Applications of Reduced Order Modeling Techniques in Computational Neuroscience

A Dissertation Presented for the

Doctor of Philosophy

Degree

The University of Tennessee, Knoxville

Kaitlyn DeLacey Toth

May 2025

Dedication

Dedicated to my parents, Carol and Sandor, my brothers, Alex and Sam, and my sister, Kristen.

Acknowledgments

This research would not have been possible without my advisor, Dr. Dan Wilson, who guided and instructed me for five years, encouraged me through all my frustrations, and allowed me to absorb just a fraction of his knowledge in dynamical systems.

I would also like to thank my PhD Committee members, Dr. Seddik Djouadi, Dr. Hector Pulgar, and Dr. Suzanne Lenhart for their time and input on my research, and for mentoring me in life beyond graduate school. I am grateful for the ongoing support from the lab mates and classmates who became my friends, contributing thoughts and ideas to my research and providing a listening ear when needed. I am immensely thankful for Dr. Paul Crilly, Mr. Aaron Dahlen, and Dr. Richard Harnett at the United States Coast Guard Academy for mentoring me and inspiring me to pursue my PhD.

Last, I would like to thank my family for their constant support. I'm especially thankful for my mom and best friend, Carol, who has been my inspiration and cheerleader for almost 30 years, and for my dog Annie whose unconditional love and companionship has taught me so much about myself.

To all those friends, colleagues, mentors, and family members not specifically named here, thank you for being a part of my life throughout the completion of my PhD.

Abstract

Human brains are highly nonlinear dynamical systems comprised of neurons that communicate through electrical and chemical synapses. These neurons produce brain rhythms which play a functional role in cognitive processes. The disruption of these cognitive processes through abnormal brain rhythms can result in a variety of neurological disorders, such as Parkinson's disease, epilepsy, and treatment-resistant depression. This work is motivated by the importance of understanding neural brain rhythms in both experimental and computational settings. In this work, we implement model reduction strategies, specifically phase and phase-amplitude reduction, to explore and analyze neural behavior from a reduced order framework. Using these model reduction techniques, we develop a control strategy that drives a population of synchronized neural oscillators towards a desynchronized state, mirroring the effect of deep brain stimulation on pathologically synchronized neural oscillators. We then examine the impact of synaptic plasticity on critical coupling strength estimates for a population of inhibitory neurons with all-to-all coupling. Finally, we derive terms for a data-driven phase-amplitude model of a complicated network of neuronal subnetworks with a complex coupling structure and additive noise.

Disclosure Statement

The content and figures presented in Chapters 2 and 3 were originally published in *Chaos: An Interdisciplinary Journal of Nonlinear Science* [116] and *The Journal of Mathematical Biology* [117]. These published articles were authored by myself and my supervisor, Dr. Dan Wilson. The content and figures contained within [116] and [117] have been reproduced in this dissertation with permission from AIP Publishing and Springer Nature.

Table of Contents

List of Tables

List of Figures

Chapter 1

Introduction

The human brain is a highly nonlinear dynamical system whose functional connections have been studied in computational and experimental environments for decades [48], [5], [73]. Although much of the functional behavior of the brain is still unknown, collective research does indicate that brain rhythms play a vital part in cognitive function [73] and the emergence of abnormal brain rhythms is linked to certain neurological disorders [73] such as Parkinson's disease [8], dystonia [119], and epilepsy [60]. For some of these neurological disorders, deep brain stimulation (DBS) and its variations are successful treatments for the associated symptoms [8], [70], [104], [119], [60]. In Parkinson's disease, for instance, the excessive synchronization of neurons is related to the onset of Parkinsonian tremors, and the desynchronization of these neurons through high-frequency DBS can temporarily alleviate the tremors [73], [41], [54], [58], [115], [9], [84], [12], [59], [49], [33]. This dissertation is motivated by the important role that brain rhythms and neural synchrony play in both cognitive function and the development and treatment of certain neurological disorders. Our research provides valuable insight into neural behavior through the analysis of neural rhythms in a computational setting.

This work specifically focuses on utilizing reduced order modeling techniques to explore, analyze, and understand different aspects of neural behavior. The reduced order modeling techniques implemented throughout this dissertation, such as phase and phase-amplitude reduction, allow high-dimensional nonlinear dynamical systems to be reduced to a lower dimension in phase space. In this work, we will apply phase and phase-amplitude reduction

techniques to high-dimensional conductance-based neural models in projects that aim to further our understanding of the role brain rhythms play in cognitive function. Each project will address a biologically relevant phenomenon, with simulation and analysis completed in the phase space.

Chapter 2 is motivated by the promising results of phase-specific adaptive DBS (aDBS) observed in patients treated for Parkinson's disease. Phase-specific aDBS is a variation of DBS where the electrical stimuli associated with DBS are locked to a particular phase of the Parkinsonian tremor [98], [92], [71], [101], [15], [38]. Adaptive forms of DBS are particularly desired due to their potential to both increase the efficacy of DBS treatments while also decreasing associated side effects. In Chapter 2, we will apply adaptive phase-amplitude reduction techniques to derive a control input with a slowly varying magnitude and phase offset that drives a population of pathologically synchronized neural oscillators towards a stable desynchronized state, mirroring the effect of aDBS on Parkinsonian tremors.

Chapter 3 considers a population of synaptically coupled neural oscillators with excitatory coupling and synaptic plasticity. Synaptic plasticity is a biologically realistic phenomenon where the synaptic connections between neurons change temporally in response to the relative spike times of the coupled neurons [37], [46], [47]. In Chapter 3, we implement phase reduction techniques to investigate new mechanisms for phase cohesion in populations of coupled neural oscillators with plastic synaptic connections. Phase cohesion is a type of neural synchrony where the population of coupled oscillators is contained within some arc length in the phase space. Specifically in Chapter 3, we define critical coupling strength estimates required to retain phase cohesion in populations of coupled neural oscillators with synaptic plasticity.

Chapter 4 derives a data-driven phase-amplitude reduced order model that extends the direct method to account for populations of coupled neural oscillators. Specifically in Chapter 4, we use least-squares fitting to determine a Fourier series approximation for the phase difference coupling functions associated with coupled oscillators. We apply this technique to model networks of neuronal subnetworks with complicated coupling structures through the analysis of population-level oscillations.

In Chapter 5, we provide concluding remarks and discuss the trajectory of future research.

Chapter 2

Control of Coupled Neural Oscillations Using Near-Periodic Inputs

The content and figures in this chapter are published in [116] and reproduced with permission from AIP Publishing.

High frequency deep brain stimulation (DBS) is a well-established treatment for Parkinson's disease. In most clinical settings, DBS is implemented by injecting 130–180 Hz pulse trains of electrical current into an appropriate brain region. Recent evidence suggests that phase-specific adaptive deep brain stimulation (aDBS), whereby the application of stimulation is locked to a particular phase of tremor, may improve therapeutic efficacy and reduce side effects. Motivated by these preliminary aDBS control strategies, this work focuses on understanding the dynamical behavior of a large population of coupled neurons in response to a nearly periodic input. Here, we apply phase-amplitude-based coordinate reduction strategies to identify a low-dimensional model and subsequently devise and validate a closed-loop control strategy to manipulate the aggregate behavior of the neural population. This work can be viewed as potential theoretical underpinning for the phase-specific adaptive DBS strategies that have gained interest in recent years.

2.1 Introduction

Deep brain stimulation is a well established treatment for medication resistant Parkinson's disease [9], [84]. DBS has also shown promise as a treatment for other neurological disorders such as epilepsy [60], depression [70], tinnitus [112], and Tourette syndrome [108]. While the fundamental mechanisms of DBS are not fully understood, one prevalent hypothesis postulates that DBS disrupts pathological synchronization among neurons in the basal ganglia-cortical loop associated with the motor symptoms of Parkinson's disease [12], [59], [49], [33]. This hypothesis has led to the development of a variety of electrical stimulation techniques designed to desynchronize populations of neurons. Coordinated reset [113], [67] is one such strategy, whereby high frequency stimulation is coordinated at different sites to desynchronize a population of oscillators that are distributed in space. The coordinated reset strategy has been shown to produce long lasting therapeutic effects in both animal and human trials [124], [1]. Other methods for achieving neural desynchronization have focused on driving neurons to a phaseless set so that they desynchronize during the relaxation to their nominal limit cycles [76], identifying energy optimal stimuli that achieve positive Lyapunov exponents and produce chaotic desynchronization [143], [132], controlling neurons to a prespecified phase distribution [74], and separating neurons into distinct clusters [144], [68], [23].

In a clinical setting, DBS is usually applied by injecting high frequency (130-180 Hz) pulse trains of electrical current into an appropriate brain region [120], [50]. While DBS is administered in an open-loop fashion in most cases, there has been a growing interest in developing demand-controlled and adaptive methods for applying DBS both to increase therapeutic efficacy and reduce the emergence of side effects. For instance, measured local field potentials (LFPs) have been used as a control variable with the goal of keeping the LFP power spectrum close to that of the tremor-free condition [98], [92], [71]. While most adaptive DBS (aDBS) strategies are fairly simple from a control theoretic perspective, generally turning off or on depending on the value of the chosen biomarker relative to some threshold, other experimental [101], [15], [38] and computational studies [39], [7], [20] have shown that timing the application of DBS input relative to the phase of a patient's tremor

rhythm can also be an effective closed-loop stimulation strategy. Indeed, phase-amplitude reduction strategies can be used to predict how phase-triggered stimulation will influence the amplitude of pathological oscillations [128] that are thought to contribute to the symptoms of Parkinson's disease; this information can subsequently be used to develop stimulation protocols for suppressing oscillation amplitude [127], [19]. Additionally, slow modulation of the magnitude of the DBS input has been been shown to be an effective aDBS strategy. For instance, increasing or decreasing the strength of the DBS pulses according to the beta band LFP power [98] or the severity of tremor [64] has been successfully demonstrated in human trials. Computational studies have also suggested that the magnitude of the DBS input could be controlled using a variety of delayed feedback approaches [89], [90], [91]; related delayed feedback approaches consider non-pulsatile inputs [99], [87].

Motivated by these preliminary aDBS control strategies, this work focuses on understanding the dynamical behavior of a large population of coupled neurons in response to a nearly-periodic input. By nearly-periodic, we mean an input that is nominally periodic (for example, as is the case for conventional DBS) with the addition of a slowly varying amplitude and phase offset that can be used to coordinate the timing of an applied input with a specified phase of the population oscillation. As illustrated in the results to follow, these additional degrees of freedom allow for the development of a closed-loop control strategy that can be used to manipulate the phase cohesion (i.e., synchronization) of a large population of neural oscillators as measured by the Kuramoto order parameter. Additionally, we identify and validate a strategy for estimating the necessary terms of the proposed closed-loop control framework in real-time so that it can be implemented without knowledge of an underlying dynamical model.

The organization of this paper is as follows: Section 3.2 provides necessary background on the phase-amplitude reduction frameworks used for the theoretical analysis in this work. Section 2.3 derives a reduced order model to characterize the behavior of a large population of noisy, coupled, conductance-based neural oscillators. Here, we employ the recently developed adaptive phase-amplitude reduction framework [138], [137] in conjunction with formal averaging techniques [105], [31] to arrive at a low order, nonlinear model describing population-level behaviors of the neural oscillators. Section 2.4 describes a

closed-loop control strategy that can be used to manipulate the phase cohesion and disrupt synchronization in population-level oscillations. Additionally, we propose a data-based strategy to estimate the terms of the associated reduced order model in real-time. Theoretical results are validated by numerical simulations with results presented in Section 3.4 for a Fokker-Planck representation of the dynamics of a coupled oscillator population and for a full model of conductance-based neurons. Section 3.5 provides concluding remarks.

2.2 Computational Model, Control Objective, and Background on Model Order Reduction Techniques

Our primary focus in this work is on the analysis of coupled, noisy, conductance-based neural oscillators in response to near-periodic forcing. The general model is described below:

$$\begin{aligned} C\dot{V}_i &= -I_{\text{ion}}(V_i, a_i) - \frac{g_0}{N}\sum_{j=1}^{N}\left[s_j(t-\tau)(V_i - E_{\text{syn}})\right] + I_{\text{stim}}(t) + \sqrt{2D}\eta_i(t), \\ \dot{s}_i &= \frac{c_1(1-s_i)}{1+\exp(-(V_i - V_T)/\sigma_T)} - c_2 s_i, \\ \dot{a}_i &= f_a(V_i, a_i), \\ i &= 1, \ldots, N. \end{aligned} \tag{2.1}$$

Above, N sets the number of neurons in the population, C is a constant membrane capacitance, V_i is the transmembrane voltage of neuron i (in mV), $a_i \in \mathbb{R}^{N_a}$ is a collection of auxiliary variables (gating variables, ionic concentrations, etc.) with dynamics governed by f_a, I_{ion} is a collection of ionic currents, s_i is a synaptic variable where c_1, V_T, σ_T, and c_2 determine the dynamics of the synaptic variable, $E_{\text{syn}} = -100$ mV is the reversal potential of the neurotransmitter so that the coupling is inhibitory, τ is a constant time delay, $g_0 > 0$ is a constant conductance that sets the synaptic coupling strength, $I_{\text{stim}}(t)$ is an externally applied current that is applied identically to each neuron, and $\eta_i(t)$ is a zero-mean white noise process associated with neuron i for which $D = 1\ \mu\text{A}^2/\text{cm}^4$ sets the intensity. Here,

the collection $\eta_1(t), \ldots, \eta_N(t)$ are independent and identically distributed. The specific forms of I_{ion} and f_a are model dependent. All neurons in Equation (2.1) are assumed to be identical. Because DBS is often applied to the subthalamic nucleus [33], for concreteness we will use a model of thalamic neurons from [103] to specify the ionic dynamics. These model equations are given in Appendix A. Terms governing the synaptic variables are taken to be $c_1 = 3, V_T = -20$ mV$, \sigma_T = 0.8$ mV$, c_2 = 1$. Inhibitory synaptic coupling is chosen because it synchronizes the population in the absence of input. We emphasize that due to the lack of heterogeneity between neurons, the simple all-to-all coupling structure, and the lack of coupling between upstream and downstream neural populations, Equation (2.1) is not meant to represent a specific target brain region for DBS. Rather, our goal is to address challenges associated with desynchronizing a population of pathologically synchronized neurons from both a dynamical systems and control theoretic perspective.

2.2.1 Description of the Primary Control Objective

In this work, we will adopt the hypothesis that pathological synchronization among neurons in the basal ganglia-cortical loop of the brain contributes to the motor symptoms of Parkinson's disease [12], [59], [49], and that therapeutic DBS disrupts this synchronization. Consequently, we will consider the identification of control strategies using $I_{\text{stim}}(t)$ to desynchronize a nominally synchronized population of neurons from Equation (2.1). Our focus in this work is on the study of the overall population response of (2.1) to nearly-periodic inputs $I_{\text{stim}}(t)$; the equations governing I_{stim} will take the general form

$$\begin{aligned} I_{\text{stim}}(t) &= \mu f_{\text{s}}(t + \zeta T_{\text{s}}/2\pi), \\ \dot{\zeta} &= \epsilon f_\zeta(t), \\ \dot{\mu} &= \epsilon f_\mu(t), \end{aligned} \tag{2.2}$$

where $f_s(t)$ is a T_s-periodic input with amplitude μ and phase offset ζ. Both ζ and μ are allowed to change slowly according to the relations f_ζ and f_μ, respectively. The input $I_{\text{stim}}(t)$ is nearly T_s-periodic, where the magnitude and phase shift are allowed to slowly vary in time. Further structure for the terms f_ζ and f_μ will be considered in the analysis to follow.

Figure 2.1 shows the behavior of a population of $N = 1000$ synaptically coupled neurons from Equation (2.1) taking the synaptic coupling time delay to be $\tau = 4$ ms. Initially, the coupling strength g_0 is set to zero allowing noise to fully desynchronize the population. At $t = 100$ ms, the coupling strength is set to $g_0 = 0.35\text{mS/cm}^2$ yielding synchronized oscillations with a period of approximately 10.9 ms. During this simulation, panel A shows the transmembrane voltage of a representative sample of neurons (colored traces) along with the average voltage (black line). Panel B shows the average value of time-delayed synaptic variable,

$$\bar{s}(t) = \frac{1}{N}\sum_{j=1}^{N} s_i(t-\tau). \tag{2.3}$$

The average synaptic variable will be used as a model observable in the development of the control strategies in the following sections. In Figure 2.1, the emergence of synchronization can clearly be seen from the individual neural traces in Panel A. In order to quantify the

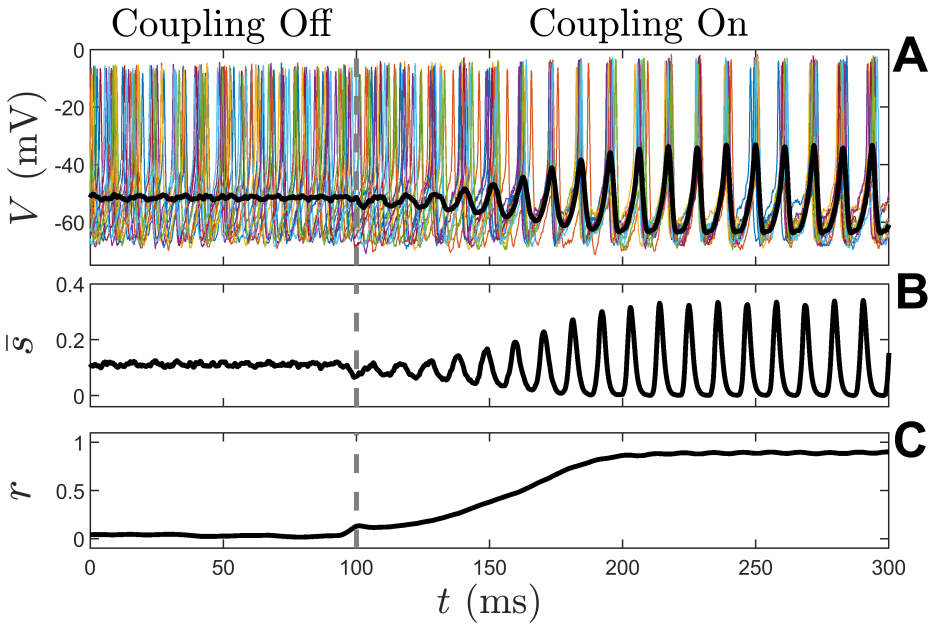

Figure 2.1: For a collection of N neurons from Equation (2.1), g_0 is set to 0mS/cm^2 for $t < 100$. Starting at $t = 100$, coupling is turned on taking $g_0 = 0.35\text{mS/cm}^2$. Colored traces in Panel A show the transmembrane voltages of a representative sample of neurons and the black line shows the average voltage. A transition from incoherence to synchronization is clearly observed after the coupling is turned on. Panels B and C show the associated values of the time-delayed average value of the synaptic variable and the order parameter computed according to Equations (2.3) and (2.4), respectively

level of synchronization, we will consider the Kuramoto order parameter

$$r(t) = \left| \frac{1}{N} \sum_{j=1}^{N} e^{i\theta_j(t)} \right|, \tag{2.4}$$

where θ_j is the asymptotic phase of neuron j (as defined by the isochrons according to Equation (2.8)). Intuitively, r takes values between 0 and 1 and gives a sense of the overall level of phase coherence. $r \approx 1$ corresponds states that are more synchronized, i.e., with a probability distribution that is well approximated by a delta function. A fully desynchronized splay state, having a uniform distribution, returns $r = 0$. While the Kuramoto order parameter is not a perfect measure of synchrony (for example, rotating block solutions can also have an order parameter of 0) this metric is sufficient for the purposes of this work to quantify the level of synchronization of a distribution of oscillators. The order parameter associated with the simulations shown in Figure 2.1 is shown in Panel C. Indeed, before coupling is applied $r(t)$ starts near zero and grows to $r(t) \approx 0.9$ after the coupling is turned on indicating a high degree of phase cohesiveness.

2.2.2 Phase-Amplitude Reduction Methods

Due to the complexity and high-dimensionality of Equation (2.1) phase-amplitude-based model order reduction techniques will be used for further analysis. To this end, consider a general dynamical system of the form

$$\dot{x} = F(x, p_0, u(t)), \tag{2.5}$$

where $x \in \mathbb{R}^N$ is the system's state, F sets the dynamics, $p_0 \in \mathbb{R}^M$ is a collection of nominal parameters, and $u(t) \in \mathbb{R}$ is an external input. Suppose that Equation (2.5) admits a stable, T-periodic limit cycle x^γ when $u(t) = 0$.

The timing of oscillations occurring in Equation (2.5) can be analyzed in a reduced order setting using the well-established method of phase reduction [147], [22], [85]. When using this strategy, the phase $\theta \in [0, 2\pi)$ is defined on the limit cycle and scaled so that $d\theta/dt = 2\pi/T = \omega$ when $u(t) = 0$. The phase can be extended to include the basin of

attraction of the limit cycle using the notion of isochrons [30], [147] which are defined as follows: for a given p_0 and taking $u(t) = 0$, for any initial condition $a(0) \in x^\gamma$, the isochron corresponding to $a(0)$ is defined to be the set of all $b(0)$ such that

$$\lim_{t\to\infty} ||a(t) - b(t)|| = 0, \tag{2.6}$$

where $b(t)$ gives the solution of (2.5) with initial condition $b(0)$ and $||\cdot||$ is some vector norm. Intuitively, initial conditions on the same isochron have the same asymptotic behavior. Defining the phase $\theta(x)$ using isochrons, one can arrive at a reduced order model by restricting attention to a close neighborhood of the periodic orbit

$$\dot{\theta} = \omega + z(\theta)u(t), \tag{2.7}$$

where $z(\theta) \equiv \langle \frac{\partial\theta}{\partial x}, \frac{\partial F}{\partial u} \rangle$ is known as the phase response curve, where each partial derivative is evaluated at $x^\gamma(\theta)$ and $u = 0$. Note that in the transformation to (2.7), Taylor expansion is used to obtain $\dot{x} = F(x, p_0, 0) + \frac{\partial F}{\partial u}u(t) + O(u^2)$ as an intermediate step. Phase reduction is a tremendously powerful tool that can be used to analyze oscillations of the N-dimensional system (2.5) using a 1-dimensional reduction. However, it is only valid in the weak perturbation limit, i.e., requiring the underlying assumption that $u(t) = O(\epsilon)$ where $0 < \epsilon \ll 1$.

Phase-only models of the form (2.7) typically fail when large magnitude inputs are required. Such inputs drive the state of the system far from the vicinity of the periodic orbit to states for which the local linearizations of the gradient of the phase are no longer accurate. To combat this issue, phase-amplitude based coordinate systems can be employed to capture the dynamics in directions transverse to the periodic orbit. A variety of such coordinate systems have been proposed and investigated in recent years [25], [135], [100], [16], [111], [126], [55]. In this work, the notion of isostable coordinates will be used, which represent level sets of the slowest decaying eigenfunctions of the Koopman operator [69]. As described in [140] (cf., [145]) one can define the slowest decaying isostable coordinates in the basin of attraction of the limit cycle by exploiting Floquet theory. By first defining $\Delta x = x - x^\gamma(\theta)$, one can write $\Delta\dot{x} = J(\theta)\Delta x + O(||\Delta x||^2)$, where $J(\theta)$ denotes the Jacobian

of the vector field evaluated at $x^\gamma(\theta)$. Letting Υ be the fundamental matrix associated with this linear equation (i.e., that solves $\Delta x(T) = \Upsilon \Delta x(0)$), define the left eigenvectors, right eigenvectors, and eigenvalues of Υ as w_j, v_j, and λ_j, respectively. Also define $\kappa_j = \log(\lambda_j)/T$ as the Floquet exponent associated with λ_j. These Floquet exponents will be sorted so that $\kappa_N = 0$ (corresponding to the $\lambda_N = 1$ eigenvalue of the fundamental matrix) and that $|\text{Re}(\kappa_j)| \leq |\text{Re}(\kappa_{j+1})|$ for all others. Provided λ_1 is not a defective eigenvalue [136], the ψ_1 isostable coordinate can be defined in the basin of attraction of the periodic orbit as follows:

$$\psi_1(x) = \lim_{k=\infty} [w_1^T (\chi(t_\Gamma^k, x) - x_0^\Gamma) \exp(-\kappa_1 t_\Gamma^k)], \tag{2.8}$$

where $\chi(t, x)$ represents the flow of (2.5) when $u(t) = 0$, x_0^Γ is the intersection of the periodic orbit and the $\theta = 0$ isochron, and t_Γ gives the time of the k^{th} transversal of the $\theta = 0$ isochron. Intuitively, isostable coordinates give a sense of the temporal distance from the periodic orbit, with larger isostable coordinates encoding for states that will take longer to relax to the periodic orbit. Isostable coordinates associated with more rapidly decaying Floquet exponents can be defined implicitly as level sets of Koopman eigenmodes. The interested reader is directed to [145], [141], and [75] for a more detailed discussion of the isostable coordinate paradigm and related reduced order modeling strategies.

2.2.3 Adaptive Phase-Amplitude Reduction

This work will employ the adaptive phase-amplitude reduction approach to consider the aggregate dynamical behavior of coupled neural oscillators using an analytically tractable reduced order coordinate basis. Following the adaptive reduction strategy illustrated in [138] and [137], Equation (2.5) can be considered in terms of the behavior of a shadow system

$$\dot{x} = F(x, p, 0) + U_e(x, p, p_0, u), \tag{2.9}$$

where

$$U_e(x, p, p_0, u) = F(x, p_0, u) - F(x, p, 0). \tag{2.10}$$

One can verify that Equation (2.9) is mathematically equivalent to Equation (2.5). Here $F(x, p, 0)$ is taken to be the nominal dynamical behavior and U_e is an effective additive input. It will be assumed that for some nominal range of system parameters p, that a periodic solution x_p^γ exists and is continuously differentiable with respect to both θ and p. In reference to each periodic orbit, a generalized phase, $\theta(x, p)$ and a set of slowly decaying generalized isostable coordinates $\psi_1(x, p), \ldots, \psi_\beta(x, p)$ can be considered. Assuming that $\theta(x, p)$ and each $\psi_j(x, p)$ are continuously differentiable in a neighborhood of the limit cycle for all x and p, one can transform to phase and isostable coordinates via the chain rule

$$\begin{aligned} \frac{d\theta}{dt} &= \frac{\partial\theta}{\partial x} \cdot \frac{dx}{dt} + \frac{\partial\theta}{\partial p} \cdot \frac{dp}{dt}, \\ \frac{d\psi_j}{dt} &= \frac{\partial\psi_j}{\partial x} \cdot \frac{dx}{dt} + \frac{\partial\psi_j}{\partial p} \cdot \frac{dp}{dt}, \end{aligned} \tag{2.11}$$

for $j = 1, \ldots, \beta$. In the above transformation, the nominal parameter set is allowed to change as a function of time. A detailed description of strategies for the computation of the partial derivatives from (2.11) are presented in [138]. Evaluation of these terms yields the adaptive reduction

$$\begin{aligned} \dot{\theta} &= \omega(p) + Z(\theta, p) \cdot U_e(x, p, p_0, u) + D(\theta, p) \cdot \dot{p}, \\ \dot{\psi}_j &= \kappa_j(p)\psi_j + I_j(\theta, p) \cdot U_e(x, p, p_0, u) + Q_j(\theta, p) \cdot \dot{p}, \\ j &= 1, \ldots, \beta, \\ \dot{p} &= G_p(p, \theta, \psi_1, \ldots, \psi_\beta). \end{aligned} \tag{2.12}$$

Above, $\omega(p)$ is the natural frequency of the unperturbed periodic orbit x_p^γ, $Z(\theta, p)$ is the gradient of the phase coordinate evaluated on x_p^γ, $D(\theta, p) = \frac{\partial\theta}{\partial p}$ and captures how changes to the adaptive parameter set influence the generalized phase, $\kappa_j(p)$ is the Floquet exponent associated with the j^{th} isostable coordinate, $I_j(\theta, p)$ is the gradient of the isostable coordinate ψ_j with respect to the state evaluated on x_p^γ, $Q_j(\theta, p) = \frac{\partial\psi_j}{\partial p}$ and captures how changes to the adaptive parameter set influence the isostable coordinates, and G_p is a parameter update rule that will be discussed in further detail momentarily. In the transformation from (2.9) to (2.12), the most rapidly decaying isostable coordinates (i.e., with large magnitude, negative

Floquet exponents) can be assumed to be zero and neglected from the model dynamics, thereby providing a reduction in dimensionality.

As mentioned earlier, standard phase-based reduction strategies implicitly require that the state remains close to the underlying periodic orbit. The critical advantage of the adaptive reduction is its ability to continuously update the adaptive parameter set p in order keep the isostable (amplitude) coordinates small, thereby keeping the state close to the periodic orbit x_p^γ. To accomplish this, G_p must be chosen appropriately. Some general design heuristics for G_p are proposed in [138]. For instance, when only a single non-truncated isostable coordinate is considered and $p \in \mathbb{R}^1$, it often works well in practice to choose

$$G_p(p, \theta, \psi_1) = -\nu \psi_1 Q_1(\theta, p), \tag{2.13}$$

taking $\nu > 0$. For higher dimensional reductions, G_p must be designed on an *ad hoc* basis. Provided an appropriate G_p can be found so that each ψ_j remains an $O(\epsilon)$ term at all times, one can write the state as

$$x = x_p^\gamma(\theta) + \mathcal{O}(\epsilon). \tag{2.14}$$

Substituting Equation (2.14) into (2.12) yields a closed reduced order equation that no longer requires direct knowledge of the state x.

2.3 Analysis of Near-Periodic Forcing in an Oscillatory Population of Synaptically Coupled Neurons

Here, using the adaptive phase-amplitude reduction framework in conjunction with formal averaging techniques, we illustrate that the general model of the form (2.1) with an externally applied current of the form (2.2) can be accurately represented according to a low-dimensional set of autonomous ordinary differential equations. Ultimately, this reduced order model will be used to analyze the influence of f_ζ and f_μ from (2.2) on the efficacy of the control law.

2.3.1 Representation of the Noisy Population of Oscillators Using the Fokker-Planck Equation

In the absence of coupling, input, and noise, we assume that each neuron from (2.1) has a strongly attracting periodic orbit with unperturbed period T_n so that the each neuron can be represented as a limit cycle oscillator. Using the phase reduction from (2.7), the Equations describing (2.1) become:

$$\dot{\theta}_i^n = \omega_n + z(\theta_i^n)\left[I_{\text{stim}}(t) + \sqrt{2D}\eta_i(t) - \frac{g_0}{N}\sum_{j=1}^{N}\left[s(\theta_j^n - 2\pi\tau/T_n)(V(\theta_i^n) - E_{\text{syn}})\right]\right], \quad (2.15)$$

for $i = 1, \ldots, N$. Here θ_j^n is the phase of the j^{th} neuron. Because the periodic orbit is strongly attracting, functions $V(\theta_i^n)$ and $s(\theta_i^n)$ are used to represent the transmembrane voltage and synaptic variable associated with the i^{th} neuron as a function of the phase [51]. Additionally, $\omega_n = 2\pi/T_n$. As part of the transformation to phase coordinates, it is assumed that D is small enough so that terms proportional to the square of the noise intensity can be truncated [62], (cf., [4]). In the formulation above g_0 and I_{stim} are assumed to be small enough so that $s_i(t-\tau)$ is well approximated by $s(\theta_i - 2\pi\tau/T_n)$ for all i. Note that in this work, we use the deterministic definition of phase from (2.8) which is defined for each neural oscillator with respect to the stable limit cycle in the absence of noise and other inputs. We emphasize that alternative formulations of phase are possible (see for instance [109], [114]) that directly incorporate the effects of noise.

Provided that the population of neurons is large enough, Equation (2.15) can be represented according to a probability density $\rho(\theta^n, t)$ that evolves according to the Fokker-Planck equation using an Ito formulation [24]:

$$\begin{aligned}\frac{\partial \rho}{\partial t} &= -\frac{\partial}{\partial \theta^n}\left[\left(\omega + z(\theta^n)\left[I_{\text{stim}}(t) - g_0\bar{s}(V(\theta^n) - E_{\text{syn}})\right]\right)\rho(\theta^n, t)\right] + \frac{\partial^2}{\partial {\theta^n}^2}\left[Dz^2(\theta^n)\rho(\theta^n, t)\right], \\ &= \underbrace{-\omega\rho_\theta + \frac{\partial^2}{\partial {\theta^n}^2}\left[Dz^2(\theta^n)\rho\right] - \frac{\partial}{\partial \theta^n}\left[z(\theta^n)g_0\bar{s}(V(\theta^n) - E_{\text{syn}})\rho\right]}_{\text{Internal Dynamics}} - \underbrace{\left[z(\theta^n)\rho_\theta + z_\theta\rho\right]I_{\text{stim}}(t)}_{\text{External Input}}, \quad (2.16)\end{aligned}$$

where

$$\bar{s} = \int_0^{2\pi} s(\theta^n - 2\pi\tau/T_n)d\theta^n, \quad (2.17)$$

and ρ_θ and z_θ denote the partial derivatives taken with respect to θ^n. Because $\theta^n \in \mathbb{S}^1$, the boundary conditions of this partial differential equation (PDE) are periodic. Equation (2.17) is analogous to Equation (2.3) and is valid when considering probability distributions instead of a finite population of neurons. For all simulations of (2.16), we will take $\tau = 1.68$. This value is chosen so that the coupling yields phase cohesive solutions in the absence of input. Towards a formulation using the adaptive reduction strategy described in Section 2.2.3, we distinguish between the internal dynamics, and the external input, separating terms that depend on $I_{\text{stim}}(t)$. The PDE model (2.16) will be further analyzed using a finite difference approximation with 100 total gridpoints for the θ axis. Letting $x^{\theta^n} \in \mathbb{R}^{100}$ represent the discretized solution of the phase distribution, after discretization the dynamics of Equation (2.16) can be approximated according to

$$\dot{x}^{\theta^n} = F^{\theta^n}(x^{\theta^n}, g_0) - I_{\text{stim}}(t)\big[\text{diag}(z_d)A + \text{diag}(Az_d)\big]x^{\theta^n}, \tag{2.18}$$

where $z_d \in \mathbb{R}^{100}$ is a discretized version of $z(\theta^n)$, F^{θ^n} represents the resulting dynamics that are solely a function of the state and coupling strength, A is a matrix which implements the finite difference approximation of the derivative of $\rho(\theta^n, t)$ with respect to θ^n, and $\text{diag}(\cdot)$ takes a vector as its argument and returns a diagonal matrix of compatible size.

2.3.2 Representation of the Temporal Evolution of the Probability Distribution Using the Adaptive Reduction Paradigm

Equation (2.18) is in the same general form as Equation (2.5) (with $I_{\text{stim}}(t)$ taking the place of $u(t)$) allowing for the implementation of the adaptive phase-amplitude reduction strategy described in Section 2.2.3. Here we will take the synaptic coupling strength to be the adaptive parameter allowing Equation (2.18) to be analyzed in terms of the shadow system

$$\begin{aligned} \dot{x}^{\theta^n} &= F^{\theta^n}(x^{\theta^n}, g) + U_e(t, g, g_0, x^{\theta^n}), \\ U_e(x^{\theta^n}, g, g_0, I_{\text{stim}}(t)) &= F^{\theta^n}(x^{\theta^n}, g_0) - I_{\text{stim}}(t)\big[\text{diag}(z_d)A + \text{diag}(Az_d)\big]x^{\theta^n} - F^{\theta^n}(x^{\theta^n}, g), \end{aligned} \tag{2.19}$$

where the coupling strength $g \in [0.225, 0.455]$ is taken to be the adaptive parameter. For each value of g considered, the model has a stable periodic orbit x_g^γ with period ranging from 9.47 to 13.57 ms. Here, the variable θ will be used to denote the population phase that describes the timing of the population-level oscillations. Note that θ, the phase of the population oscillation, is distinct from

θ^n, the phase of an individual oscillator with respect to its unperturbed limit cycle. Each periodic orbit, $x_g^\gamma(\theta)$, will be aligned so that $\theta = 0$ corresponds to the moment that $\bar{s}$ reaches is maximum value on the limit cycle. Implementing the adaptive reduction strategy discussed in Section 2.2.3 and considering the equations governing the applied stimulus from (2.2), the dynamics of Equation (2.19) can be represented according to

$$\begin{aligned}
\dot{\theta} &= \omega(g) + Z(\theta, g)U_e + D(\theta, g)\dot{g}, \\
\dot{\psi}_1 &= \kappa(g)\psi_1 + I_1(\theta, g)U_e + Q_1(\theta, g)\dot{g}, \\
\dot{g} &= -\nu Q_1(\theta, p)\psi_1, \\
\dot{\zeta} &= \epsilon f_\zeta(\theta, g, \mu), \\
\dot{\mu} &= \epsilon f_\mu(\theta, g, \mu),
\end{aligned} \tag{2.20}$$

with $I_{\text{stim}} = \mu f_s(t + \zeta T_s/2\pi)$, and $\nu = 0.1$. Above, the structure of f_ζ and f_μ has been rewritten to depend on the reduced order model parameters θ, g, and μ rather than on time itself. Additionally, it is assumed that all but one of the isostable coordinates decay rapidly and can be ignored. Per Equation (2.14), the associated probability distribution can be approximated in terms of the reduced order model parameters according to

$$\rho(\theta^n, g) = x_g^\gamma(\theta). \tag{2.21}$$

Note that the parameter update rule for $\dot{g}$ from Equation (2.20) matches the general strategy from (2.13) that serves to drive ψ_1 to smaller magnitude values. Figure 2.2 shows various characteristics of the reduced order model from (2.20). Panel A shows $\rho(\theta^n, g)$ plotted at $\theta = 0$ for various values of g on the appropriate limit cycles. As g decreases, the coherence between the oscillators decreases, resulting in a less synchronous population oscillation. Panel B shows the magnitudes of the principal Floquet multiplier (blue line) as well as secondary and tertiary complex-conjugate Floquet multipliers. The relatively fast decay of the complex-conjugate eigenvalues allows the model (2.19) to be represented using a single isostable coordinate. Taking $g_0 = -0.35$ mS/cm^2, in response to a the periodic input $I_{\text{stim}}(t) = 1.2\sin(2\pi t/5)$, panel C shows the evolution of the adaptive parameter over time. Panel D compares two sample probability distributions associated with the reduced order equations (2.20) and full order equations (2.18) with solid and dashed lines, respectively, at two separate times. Times associated with larger (resp. smaller) values of g are

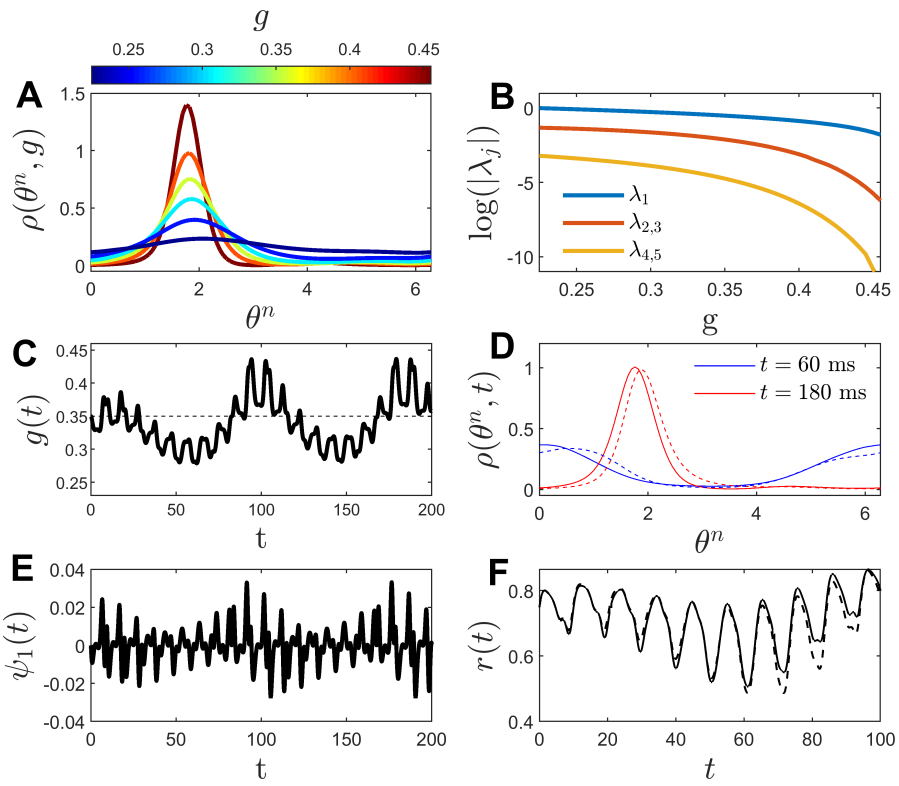

Figure 2.2: Illustration of relevant terms from the reduced order model (2.20) and a comparison with full order simulations of (2.18). Panel A shows $\rho(\theta^n, g)$ associated with x_g^γ evaluated at $\theta = 0$ for various values of g. Plots of the magnitudes of the Floquet multipliers associated with the slowest decaying Floquet eigenmodes are shown in panel B. Panels C-F show simulation results when a periodic input of $I_{\text{stim}}(t) = 1.2\sin(2\pi t/5)$ is applied to both the full and reduced order models. Panel C shows the evolution of the adaptive parameter over time with the dashed line highlighting the nominal value of g_0. For these simulations, panel D shows two snapshots of the phase distribution for the output from the reduced order model (solid lines) and the full order models (dashed lines). Panel F shows the time course of the Kuramoto order parameter for the full and reduced order models. As shown in panel E, the value of the isostable coordinate remains small during the course of the simulation, as required by the adaptive reduction strategy.

associated with more (resp. less) phase cohesive oscillations. Panel E shows that the isostable coordinate ψ_1 does indeed remain small over time as require by the adaptive reduction framework, and panel F shows the magnitude of the Kuramoto order parameter,

$$r(t) = \left| \int_0^\pi e^{i\theta^n} \rho(\theta^n, t) d\theta^n \right|, \tag{2.22}$$

computed both from the output of the reduced order model (black line) and the full model simulations (dashed line). Compared to Equation (2.4), Equation (2.22) is valid in the limit that N tends toward infinity. Overall, we observe good agreement between the full order and reduced order simulations.

2.3.3 Analysis of Reduced Order Model Dynamics Using Formal Averaging Techniques

In the previous section, we illustrated that the evolution of the probability distribution of phases within a large population of coupled neural oscillators can be represented in terms of a low order set of equations of the form (2.20) by using the adaptive phase-amplitude reduction paradigm. By recognizing that U_e from Equation (2.20) is periodic in t, we illustrate that further reduction in dimensionality can be realized using formal averaging techniques [105], [31].

To begin, recalling from Equation (2.2) that T_s is the nominal period of the input f_s, we will work in a rotating reference frame defining

$$\phi \equiv \theta - \Omega t - \zeta, \tag{2.23}$$

where $\Omega \equiv 2\pi/T_s$. Note that we have incorporated ζ in the definition of our rotating reference frame, which explicitly accounts for the slowly varying phase offset of the applied input.

Working in this rotating reference frame, Equation (2.20) becomes

$$\begin{aligned}
\dot{\phi} &= \omega(g) - \Omega + Z(\phi + \Omega t + \zeta, g) \cdot U_e + D(\phi + \Omega t + \zeta, g)\dot{g} - \epsilon f_\zeta(\phi + \Omega t + \zeta, g, \mu), \\
\dot{\psi}_1 &= \kappa(g)\psi_1 + I_1(\phi + \Omega t + \zeta, g) \cdot U_e + Q_1(\phi + \Omega t + \zeta, g)\dot{g}, \\
\dot{g} &= -\nu Q_1(\phi + \Omega t + \zeta, g)\psi_1, \\
\dot{\zeta} &= \epsilon f_\zeta(\phi + \Omega t + \zeta, g, \mu), \\
\dot{\mu} &= \epsilon f_\mu(\phi + \Omega t + \zeta, g, \mu).
\end{aligned} \tag{2.24}$$

Recall from Equation (2.19) that $U_e(x^{\theta^n}, g, g_0, I_{\text{stim}}(t))$ is periodic in time with period T_s. We will assume that U_e, ψ_1, and $\omega(g) - \Omega$ are $O(\epsilon)$ terms so that Equation (2.24) can be written in the general form $\dot{x} = \epsilon F_R(x, t)$ where $x = \begin{bmatrix} \phi & \psi_1 & g & \zeta & \mu \end{bmatrix}^T$, and F_R gives the dynamics and is periodic in t. For such a system the method of averaging [105], [31] can be used to approximate

the behavior of (2.24) according to

$$\begin{aligned}
\dot{\phi} &= \omega(g) - \Omega + \epsilon A_1(\phi, g, \mu) - \nu\psi_1 A_2(\phi, g) - \epsilon A_3(\phi, g, \mu), \\
\dot{\psi}_1 &= \big(\kappa(g) - \nu A_5(\phi, g)\big)\psi_1 + \epsilon A_4(\phi, g, \mu), \\
\dot{g} &= -\nu\psi_1 A_6(\phi, g), \\
\dot{\zeta} &= \epsilon A_3(\phi, g, \mu), \\
\dot{\mu} &= \epsilon A_7(\phi, g, \mu),
\end{aligned} \tag{2.25}$$

where

$$\begin{aligned}
A_1(\phi, g, \mu) &= \frac{1}{\epsilon T_s}\int_0^{T_s}\Big[Z(\phi + \Omega t + \zeta, g) \cdot U_e(x_g^\gamma(\phi + \Omega t + \zeta), g, g_0, \mu f_s(t + \zeta/\Omega))\Big]dt, \\
A_2(\phi, g) &= \frac{1}{T_s}\int_0^{T_s}\Big[D(\phi + \Omega t + \zeta, g)Q_1(\phi + \Omega t + \zeta, g)\Big]dt, \\
A_3(\phi, g, \mu) &= \frac{1}{T_s}\int_0^{T_s}\Big[f_\zeta(\phi + \Omega t + \zeta, g, \mu)\Big]dt, \\
A_4(\phi, g, \mu) &= \frac{1}{\epsilon T_s}\int_0^{T_s}\Big[I_1(\phi + \Omega t + \zeta, g) \cdot U_e(x_g^\gamma(\phi + \Omega t + \zeta), g, g_0, \mu f_s(t + \zeta/\Omega))\Big]dt, \\
A_5(\phi, g) &= \frac{1}{T_s}\int_0^{T_s}\Big[Q_1^2(\phi + \Omega t + \zeta, g)\Big]dt, \\
A_6(\phi, g) &= \frac{1}{T_s}\int_0^{T_s}\Big[Q_1(\phi + \Omega t + \zeta, g)\Big]dt, \\
A_7(\phi, g, \mu) &= \frac{1}{T_s}\int_0^{T_s}\Big[f_\mu(\phi + \Omega t + \zeta, g, \mu)\Big]dt.
\end{aligned} \tag{2.26}$$

Using the averaging framework, Equation (2.25) provides a close approximation to the unaveraged system of equations from (2.24). Note that the terms A_1 through A_7 do not explicitly depend on ζ, which shifts the periodic terms of each integrand but does not influence the result when integrating over the entire period. Also, A_1 through A_7 are assumed to be $O(1)$ terms; even though A_1 and A_4 are multiplied by $1/\epsilon$, the term U_e in the integrand is an $O(\epsilon)$ term.

Further simplification of Equation (2.25) is possible provided ν is chosen large enough so that ψ_1 rapidly converges to its steady state value. To this end, define

$$\psi_{ss}(\phi, g, \mu) \equiv \frac{-\epsilon A_4(\phi, g, \mu)}{\kappa(g) - \nu A_5(\phi, g)}, \tag{2.27}$$

as the steady state value of ψ_1 that results when ϕ, g, ζ, and μ are held fixed. Recognizing that the right hand sides of Equation (2.25) are comprised of $O(\epsilon)$ terms, $\dot{\phi}, \dot{g}, \dot{\mu}$, and $\dot{\zeta}$ are also $O(\epsilon)$ terms. Taking the time derivative of ψ_{ss} one can show that

$$\frac{d\psi_{ss}}{dt} = O(\epsilon^2). \tag{2.28}$$

Next, defining $\Delta\psi_1 \equiv \psi_1 - \psi_{ss}$ and taking the time derivative, one finds

$$\begin{aligned}
\Delta\dot{\psi}_1 &= \big(\kappa(g) - \nu A_5(\phi, g)\big)\psi_1 + \epsilon A_4(\phi, g, \mu) - O(\epsilon^2) \\
&= \big(\kappa(g) - \nu A_5(\phi, g)\big)(\psi_1 - \psi_{ss} + \psi_{ss}) + \epsilon A_4(\phi, g, \mu) - O(\epsilon^2) \\
&= \big(\kappa(g) - \nu A_5(\phi, g)\big)(\Delta\psi_1) + O(\epsilon^2).
\end{aligned} \tag{2.29}$$

Because all periodic orbits used in the adaptive reduction are stable, $\kappa(g) < 0$. Likewise, $A_5(\phi, g) > 0$ since the integrand from (2.26) is nonnegative and $\nu > 0$ by definition. Considering that $\kappa(g) - \nu A_5(\phi, g) = O(1)$ provided that $\Delta\psi_1 = O(\epsilon^2)$ at $t = 0$, $\Delta\psi_1 = O(\epsilon^2)$ uniformly bounded in time and consequently $\psi_1 = \psi_{ss}$ can be used as an approximation that is valid up to $O(\epsilon^2)$. This allows for the elimination of the ψ_1 dynamics from Equation (2.25) to yield

$$\begin{aligned}
\dot{\phi} &= \omega(g) - \Omega + \epsilon A_1(\phi, g, \mu) - \nu\psi_{ss} A_2(\phi, g) - \epsilon A_3(\phi, g, \mu) + O(\epsilon^2), \\
\dot{g} &= -\nu\psi_{ss} A_6(\phi, g) + O(\epsilon^2), \\
\dot{\zeta} &= \epsilon A_3(\phi, g, \mu), \\
\dot{\mu} &= \epsilon A_7(\phi, g, \mu),
\end{aligned} \tag{2.30}$$

Finally, provided $|\nu A_5(\phi, g)| \gg |\kappa(g)|$, one can write

$$\psi_{ss} = \epsilon \left(\frac{A_4(\phi, g, \mu)}{\nu A_5(\phi, g)} + O\left(\frac{\kappa(g)}{\nu^2}\right) \right). \tag{2.31}$$

Substituting (2.31) into Equation (2.30) finally yields

$$
\begin{aligned}
\dot{\phi} &= H_1(\phi, g, \mu) - \epsilon A_3(\phi, g, \mu) + O(\epsilon^2) + O\left(\frac{\epsilon\kappa(g)}{\nu}\right), \\
\dot{g} &= H_2(\phi, g, \mu) + O(\epsilon^2) + O\left(\frac{\epsilon\kappa(g)}{\nu}\right), \\
\dot{\zeta} &= \epsilon A_3(\phi, g, \mu), \\
\dot{\mu} &= \epsilon A_7(\phi, g, \mu),
\end{aligned} \tag{2.32}
$$

where

$$
\begin{aligned}
H_1(\phi, g, \mu) &= \omega(g) - \Omega + \epsilon A_1(\phi, g, \mu) - \frac{\epsilon A_4(\phi, g, \mu) A_2(\phi, g)}{A_5(\phi, g)}, \\
H_2(\phi, g, \mu) &= -\frac{\epsilon A_4(\phi, g, \mu) A_6(\phi, g)}{A_5(\phi, g)}.
\end{aligned} \tag{2.33}
$$

Equation (2.32) will be used to investigate the response of the neural oscillator population to the near-periodic input described by Equation (2.2). In the averaged setting, the phase offset and the magnitude of the input can be modulated slowly through the functions A_3 and A_7, respectively. Strategies for designing these inputs will be considered momentarily. Note that in situations where $\dot{\zeta} = \dot{\mu} = 0$, i.e., when purely periodic inputs are applied, only two state variables are required to represent the perturbed dynamics. We emphasize that in the reduction from Equation (2.25) to Equation (2.32), the term ν disappears provided that $|\nu A_5(\phi, g)|$ is sufficiently larger than $|\kappa(g)|$ for all choices of ϕ and g.

In Figure 2.3 the temporal evolution of ϕ is compared for simulations of the averaged model equations from (2.32) and the unaveraged model equations from (2.20) when using two different periodic sinusoidal inputs. In this example, we take $\zeta = \dot{\zeta} = \dot{\mu} = 0$ so that the input is fully periodic. Note here that for the input $I_{\text{stim}}(t) = 1.2\sin(2\pi t/5)$, when computing the averaged equations Ω is taken to be $2\pi/10$ in order to keep the magnitude of $\omega(g) - \Omega$ small. After computing the averaged functions A_1-A_7 using (2.26), $\dot{\phi}$ (resp., $\dot{g}$) computed according to Equation (2.32) is shown in panels A and D (resp., B and E) for the two different stimuli. Overall, the averaged equations from (2.32) accurately represent the unaveraged dynamics from Equation (2.20) with results of individual simulations shown in Panels C and F. Nullclines are plotted with red and green dashed lines to highlight the salient dynamical behavior.

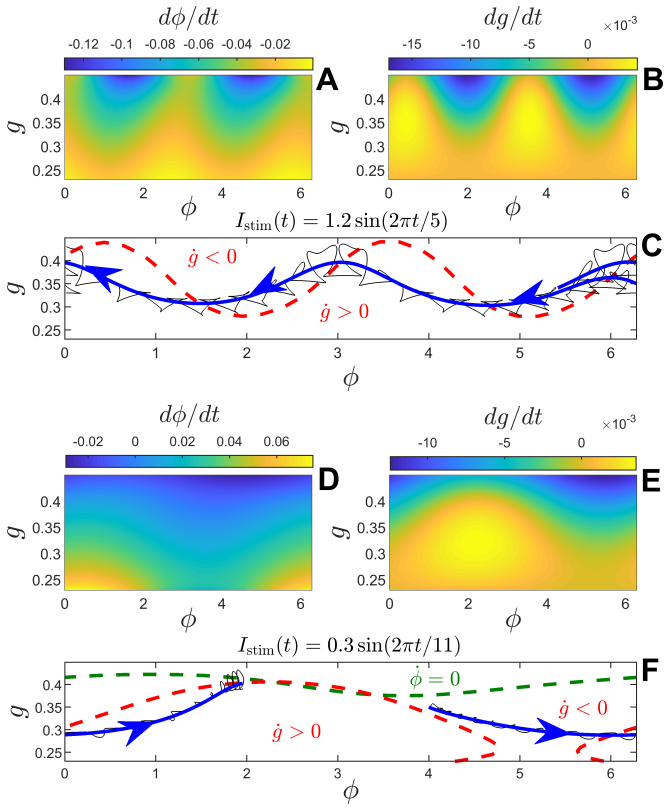

Figure 2.3: For the input $I_{\text{stim}}(t) = 1.2\sin(2\pi t/5)$, panels A and B show $\dot{\phi}$ and $\dot{g}$, respectively, computed according to the averaged equations from (2.32). Panel C shows traces of the averaged equation (blue line) and the unaveraged equations (black line). A nullcline of $\dot{g}$ associated with the averaged equations is plotted in red. The magnitude of g, and hence the level of coherence between oscillators, grows and shrinks depending on whether the state is above or below the $\dot{g} = 0$ nullcline. There are no nullclines associated with $\dot{\phi}$ for the example shown in panel C. Panels D-F show similar information when using $I_{\text{stim}}(t) = 0.3\sin(2\pi t/11)$. For this input, the system stably entrains to $I_{\text{stim}}(t)$; this entrained solution corresponds to a stable fixed point of the averaged equations from (2.32).

Results in Figures 2.2 and 2.3 illustrate that both the reduced order equations obtained using the adaptive reduction strategy (2.20) as well as the averaged equations from (2.32) provide a good approximation to the dynamics of (2.16). In the following section, we will use these reduced order equations to develop control strategies for manipulating the population level oscillations with the goal of disrupting synchronization.

2.4 A Control Strategy to Manipulate the Phase Cohesion of the Oscillator Population

The results from Figure 2.3 correspond to a situation where f_ζ and f_μ from Equation (2.2) are zero, that is, where the applied input is purely periodic. As we will illustrate here, by slowly changing the magnitude of the input and the relative offset of the rotating reference frame, μ and ζ, respectively, the cohesion between oscillators from (2.1) can be effectively manipulated.

2.4.1 A Controller for the Input Magnitude and Phase Offset

Our goal is to identify functions f_ζ and f_μ from Equation (2.20) that can shift the state of the adaptive parameter in the reduced order equations from (2.20) from $g = g_0$ to some $g = g_{\text{targ}} < g_0$. By shifting g to smaller values, the resulting phase distribution will be less synchronized. We emphasize that in the implementation of the control algorithm, the actual strength of the synaptic coupling does not change. Rather, the goal is to apply input using $I_{\text{stim}}(t)$ that drives the system to less synchronized states that are near the periodic orbit associated with the parameter g_{targ}.

Intuitively, towards the identification of an appropriate control strategy, first consider the $\dot{g} = 0$ nullcline from panel C of Figure 2.3 obtained for the averaged equations (2.32). Referring to this nullcline by $g = f_n(\phi)$, for any g_{targ} in the range of $f_n(\phi)$, the control objective could be satisfied provided that ϕ could be set to some value ϕ_{targ} for which $g_{\text{targ}} = f_n(\phi_{\text{targ}})$. For instance, considering the $\dot{g} = 0$ nullcline from Panel C of Figure 2.3, if a control strategy can be found that sets ϕ to a constant value of 5 radians, g would tend towards 0.28. Likewise, considering the nullclines from Panel F of Figure 2.3, by actively controlling ϕ to values between 4.7 and 5.6 radians, g can be driven to any desired value less then g_0. In this case, however, the magnitude of the input, μ would need to be decreased as g is driven near its lower limit. With this in mind, we will consider a control strategy that seeks to drive g and ϕ to g_{targ} and ϕ_{targ}, respectively. This control strategy will be implemented by mandating the following update rules for ζ and μ from Equation (2.20):

$$\begin{aligned} \epsilon f_\zeta(\theta) &= K_1(\theta - \Omega t - \zeta - \phi_{\text{targ}}), \\ \epsilon f_\mu(g, \mu) &= K_2(g - g_{\text{targ}}) + K_3 \int_0^t (g - g_{\text{targ}}) d\tau - K_4 \mu, \end{aligned} \tag{2.34}$$

where K_1-K_4 are appropriately chosen, positive constants. Here, In the averaged reference frame, i.e., using (2.32), this choice of f_ζ and f_μ yields the relationships

$$\begin{aligned}
\dot{\phi} &= H_1(\phi, g, \mu) - K_1(\phi - \phi_{\text{targ}}), \\
\dot{g} &= H_2(\phi, g, \mu), \\
\dot{\zeta} &= K_1(\phi - \phi_{\text{targ}}), \\
\dot{\mu} &= K_2(g - g_{\text{targ}}) + a_I - K_4\mu, \\
\dot{a}_I &= K_3(g - g_{\text{targ}}),
\end{aligned} \tag{2.35}$$

where a_i is an extra variable used to represent the necessary terms from the integral control. Intuitively in the above equations, the term $K_1(\phi - \phi_{\text{targ}})$ acts as a proportional controller that serves to update the offset of the rotating reference frame, ζ, to manipulate ϕ. The term $K_2(g - g_{\text{targ}}) + a_I$ serves as a proportional-integral controller that increases or decreases the magnitude of the applied input depending on whether g is above or below its target value. The additional term, $-K_4\mu$, is added to influence stability of the controller. Of course, the efficacy of the controller (2.34) depends on an adequate choice for ϕ_{targ} and g_{targ}. These considerations will be discussed in the results to follow.

2.4.2 Real-Time Estimation of Reduced Order Terms for Model Independent Control

Implementation of the control strategy proposed in Equation (2.35) requires knowledge of the functions $H_1(\phi, g, \mu)$ and $H_2(\phi, g, \mu)$. If an underlying model of the form (2.20) is known, these equations can be identified by first directly evaluating the integrals from Equation (2.26) and then computing the necessary terms from Equation (2.33). In the absence of an underlying dynamical model, the required functions $H_1(\phi, g, \mu)$ and $H_2(\phi, g, \mu)$ can still be estimated in real-time from observable data using a strategy described below.

Consider a general system of the form (2.5) with a set of reduced order, averaged equations that take the form (2.32). As was the case for the reduction of the noisy oscillator population from (2.15), assume that $\theta = 0$ can be clearly identified from measured data (for instance, $\theta = 0$ for a given periodic orbit from Equation (2.16) corresponds to the moment that $\bar{s}$ reaches a local maximum). Consider two successive traversals of the $\theta = 0$ level set, occurring at t_1 and t_2. The

associated coordinates in the rotating reference frame defined by Equation (2.23) are

$$\begin{aligned}\phi(t_1) &= \text{mod}(-\Omega t_1 - \zeta(t_1), 2\pi),\\ \phi(t_2) &= \text{mod}(-\Omega t_2 - \zeta(t_2), 2\pi).\end{aligned} \tag{2.36}$$

Towards identifying a strategy to estimate the unknown functions H_1 and H_2 from observable data, one can rewrite Equation (2.32) as

$$\begin{aligned}\dot{\phi} &= H_1(\phi(t_2), g(t_2), \mu(t_2)) - \epsilon A_3(\phi, g, \mu) + O(\epsilon^2) + O\left(\frac{\epsilon\kappa(g)}{\nu}\right),\\ \dot{g} &= H_2(\phi(t_2), g(t_2), \mu(t_2)) + O(\epsilon^2) + O\left(\frac{\epsilon\kappa(g)}{\nu}\right),\\ \dot{\zeta} &= \epsilon A_3(\phi, g, \mu),\\ \dot{\mu} &= \epsilon A_7(\phi, g, \mu).\end{aligned} \tag{2.37}$$

Above, the arguments of H_1 and H_2 are evaluated at the fixed time t_2. Because $\dot{\phi}$, $\dot{g}$, $\dot{\mu}$, H_1, and H_2 are $O(\epsilon)$ terms, fixing time in the evaluation of H_1 and H_2 only contributes an additional $O(\epsilon^2)$ term when $t \in [t_1, t_2]$. Neglecting the $O(\epsilon^2)$ and $O(\epsilon\kappa(g)/\nu)$ terms, through direct integration of Equation (2.37) one can write

$$\begin{aligned}H_1(\phi(t_2), g(t_2), \mu(t_2)) &\approx \frac{\phi(t_2) - \phi(t_1) + \zeta(t_2) - \zeta(t_1)}{t_2 - t_1},\\ H_2(\phi(t_2), g(t_2), \mu(t_2)) &\approx \frac{g(t_2) - g(t_1)}{t_2 - t_1}.\end{aligned} \tag{2.38}$$

Equation (2.38) can be used to obtain successive, real-time estimates of H_1 and H_2, for instance, when implementing the control strategy suggested by equation (2.35), $\zeta(t)$ is known exactly at all times because it is part of the controller, $\phi(t_1)$ and $\phi(t_2)$ can be computed according to (2.23) at successive crossings of the $\theta = 0$ level set, and $g(t_2)$ and $g(t_1)$ can be inferred from output data. Using this strategy, a reduced order model does not need to be computed before implementing the control strategy described by Equation (2.35). Rather, the necessary terms of the reduced order equations can be computed in real-time as they are needed.

As a matter of practical implementation, H_1 and H_2 can be updated once per cycle and are assumed to be constant between updates. In order to mitigate small errors that would otherwise accumulate over time, the reduced order variables ϕ and g can also be updated once per cycle

to reflect the measurements from data. The approximations from Equations (2.38) require the right hand side of Equation (2.32) to be small. As such, the accuracy of these approximations will degrade as larger magnitude inputs are used.

2.4.3 List of Steps to Implement the Model Independent Control Strategy

The model independent control strategy suggested in Section 2.4.2 relies on the estimation of the terms from Equation (2.38) from observables and subsequent implementation of the controller (2.35). A step-by-step procedure for accomplishing this task is provided below.

Step 1) Identify an observable $y(t) \in \mathbb{R}^1$ to be used for the implementation of the control strategy. This observable should have clearly identifiable oscillations. Define $\theta = 0$ to correspond to a distinct feature of the oscillations that occurs once per cycle, for instance, the crossing of a Poincaré section or the attainment of a local maximum.

Step 2) Defining t_1 and t_2 to be the times of subsequent crossings of the $\theta = 0$ isochron, define a map from the observation of $y(t)$ on the interval $[t_1, t_2]$ to the variable $g(t_2)$ that encodes for the oscillation amplitude. For instance, one could take $g(t_2) = \max(y(t)) - \min(y(t))$ on the interval $t = [t_1, t_2]$.

Step 3) Choose a periodic stimulation $I_{\text{stim}}(t)$ to be applied to the system. The Period of $I_{\text{stim}}(t)$ must be close to the period of oscillation of the observable chosen in Step 1.

Step 4) Choose a set of constants K_1, K_2, K_3, K_4, and ϕ_{targ} for the controller from Equation (2.35). In a model independent setting, this will generally be a trial and error process. One can start with ϕ_{targ} and K_1 to identify choices of ϕ_{targ} that effectively decrease the magnitude of oscillations. The terms K_2, K_3, and K_4 can subsequently be tuned to appropriately modulate the stimulus magnitude.

Step 5) Choose a profile for $g_{\text{targ}}(t)$ which sets the target for the oscillation amplitude.

Step 6) Implement the controller from Equation (2.35). On a cycle-by-cycle basis, estimates of H_1 and H_2 can be updated according to Equation (2.38), estimates of $\phi(t_1)$ and $\phi(t_2)$ can be computed according to (2.23) at successive crossings of the $\theta = 0$ level set, and $g(t_2)$ and $g(t_1)$ can be inferred from the mapping defined in Step 2.

Step 7) Adjust constants K_1, K_2, K_3, K_4, and ϕ_{targ} as necessary. Performance is generally less sensitive to the choice of these constants when g_{targ} is close to the nominal value of g that results in the absence of I_{stim}. As g_{targ} is decreased, (i.e., as the oscillation amplitude decreases) parameter adjustments may be necessary to yield a viable controller.

2.5 Results

Here we present results for the implementation of the control strategy from Section 2.4 applied to both the Fokker-Planck model for the temporal evolution of the probability distribution of a large population of neurons from Equation (2.16) and for a full model of $N = 1000$ coupled neurons from Equation (2.1). As described in Section 2.3.2, The Fokker-Planck model can be represented in a reduced order form using the adaptive reduction from Equation (2.20). Consequently, the terms $H_1(\phi, g, \mu)$ and $H_2(\phi, g, \mu)$ can be computed directly from the terms of the reduced order equations using the averaging framework. For the full model of $N = 1000$ coupled neurons, direct computation of H_1 and H_2 are not possible and the real-time estimation strategy from Section 2.4.2 will be used.

2.5.1 Control of Probability Distributions of the Fokker Planck Equation

Here we consider results of the control strategy from Equation (2.35) applied to modify the phase cohesion of the Fokker-Planck model from Equation (2.16). Starting with Equation (2.16), the terms of the adaptive reduction from (2.20) are first computed taking $g_0 = 0.35$ mS/cm^2. Recall that for the allowable range of coupling strengths $g \in [0.225, 0.455]$, the associated periodic orbits have periods $T \in [9.47, 13.57]$ ms. For this application we consider the nominal input to be a periodic series of pulses:

$$I_{\text{stim}}(t + \zeta T_s/2\pi) = \begin{cases} \mu, & \text{if } \text{mod}(t + \zeta T_s/2\pi, T_s) < 6 \\ & \text{and } \text{mod}(t + \zeta T_s/2\pi, 1) < 0.5, \\ 0, & \text{otherwise.} \end{cases} \tag{2.39}$$

Here $T_s = 10$ ms and the input is a series of 6 pulses shown taking $\mu = 1$ in panel B of Figure 2.4. Using this input, the terms of the averaged, reduced order equation of the form (2.32) are determined by directly evaluating the integrals from Equation (2.26) and using them to compute the relationships from Equation (2.33). Panel A of Figure 2.4 shows level sets of $H_2(\phi, g, \mu) = 0$ shown at different values of μ. Relative to the baseline at $g_0 = -0.35$ mS/cm^2, $\dot{g}$ tends to decrease when $\phi \in [4.2, 6.2]$ and tends to increase for $\phi \in [0.4, 4]$. With this in mind, recalling that our goal is to decrease the phase cohesion by driving the adaptive parameter, g, to lower values, to implement the control strategy from Equation (2.35), we choose $\phi_{\text{targ}} = 5$ radians. Three different parameter sets C_1, C_2, and C_3 are chosen to implement the control strategy taking $\{K_1, K_2, K_3, K_4\} = \{4, 35, 0, 0\}$, $\{4, 35, 1, 0\}$, and $\{4, 35, 1, 0.2\}$, respectively. Parameter set C_1 uses only two proportional controllers to determine the update rules for ζ and μ. Parameter set C_2 adds an integral controller to the update rule for μ, and parameter set C_3 adds an additional term that is proportional to μ. The

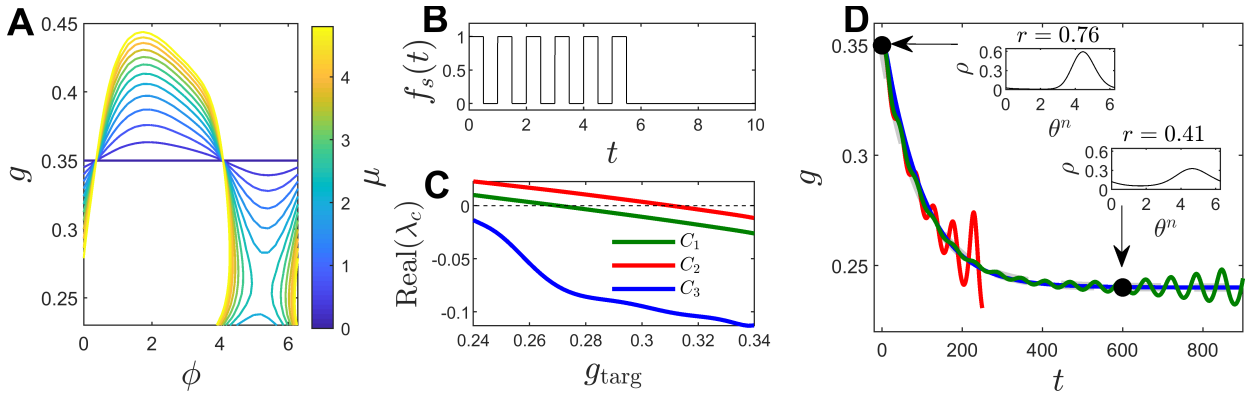

Figure 2.4: Illustration of the control strategy applied to the reduced order, averaged representation of Fokker-Planck equation from (2.35) for the periodic series of pulses shown in Panel B. Panel A shows level sets of $H_2(\phi, g, \mu) = 0$ for various values of μ. For $\phi \approx 2$ (resp., $\phi \approx 5$) the value of g tends to increase (resp. decrease), resulting in an increase (resp. decrease) in phase cohesiveness. Taking $\phi_{\text{targ}} = 5$ radians, fixed points of Equation (2.40) are obtained for different choices of g_{targ} and three different parameter sets; The largest real eigenvalue, λ_c, associated with the linearization about these fixed points is plotted against g_{targ} and shown in panel C. Fixed points for which Real$(\lambda_c) > 0$ are unstable indicating that the controller is not viable. Panel D shows the performance of each controller taking $g_{\text{targ}}(t) = 0.24 + 0.11\exp(-0.01t)$. The parameter set C_3, which uses nonzero values for all control parameters is able to decrease the phase cohesiveness of the population, with associated probability distributions shown at $t = 0$ and $t = 600$ computed according to Equation (2.21) at $\theta = \pi$. The associated order parameter computed according to Equation (2.22) is also indicated.

results to follow are qualitatively similar when modifying the non-zero values in these parameter sets.

We investigate the efficacy of these three parameter sets by investigating fixed points of

$$\begin{aligned}
\dot{\phi} &= H_1(\phi, g, \mu) - K_1(\phi - \phi_{\text{targ}}), \\
\dot{g} &= H_2(\phi, g, \mu), \\
\dot{\mu} &= K_2(g - g_{\text{targ}}) + a_I - K_4\mu, \\
\dot{a}_I &= K_3(g - g_{\text{targ}}),
\end{aligned} \tag{2.40}$$

i.e., with the same dynamics as Equation (2.35) but neglecting the ζ variable. Here, ζ is ignored to account for the fact that ϕ might not fully reach its target value. Fixed points of Equation (2.40) are obtained with a Newton iteration for various choices of g_{targ} and plotted against eigenvalues with the largest real component, λ_c, of the linearization about the fixed point. For parameter sets C_1 and C_2, stability is lost for lower values of g_{targ} as $\text{Real}(\lambda_c)$ crosses from negative to positive values. Panel D illustrates the control strategy using parameter sets C_1, C_2, and C_3 for simulations of the reduced order equations from (2.35) taking $g_{\text{targ}}(t) = 0.24 + 0.11\exp(-0.01t)$. The parameter set C_3 is able to follow this target accurately while C_1 and C_2 display unstable behavior for small values of g_{targ}. The emergence of this instability is predicted by the eigenvalue plots from panel C.

Figure 2.4 considers results for the proposed control strategy applied directly to the reduced order equations from (2.35). Next, we consider the behavior of the proposed control strategy applied to the Fokker-Planck equation from (2.16). Once again, we use the pulsatile input specified by Equation (2.39) with $T_s = 10$ ms and take $\phi_{\text{targ}} = 5$ radians. Like in the previous example, H_1 and H_2 from Equation (2.35) are obtained by directly evaluating the terms of (2.33) associated with the averaged, reduced order model dynamics from Equation (2.25). Recall that these reduced order model dynamics are approximations to the full order behavior of the Fokker-Planck equation. In order to mitigate the accumulation of small errors over time, at every crossing of $\theta = 0$ (corresponding to the moment that $\bar{s}$ from Equation (2.17) achieves a local maximum) both ϕ and μ are inferred and updated based on the measurements of $\bar{s}(t)$. For each of these updates, ϕ is inferred from Equation (2.23) and μ is inferred by comparing the value of $\bar{s}$ to the maximum values of $\bar{s}$ attained for each periodic orbit x_g^γ. Results are shown in Figure 2.5. Parameter sets C_1, C_2, and C_3 are identical to those from Figure 2.4 with the exception of taking $K_2 = 20$ instead of 35. Parameters ϕ, ζ, and μ are shown over the course of each simulation in panels A-C and

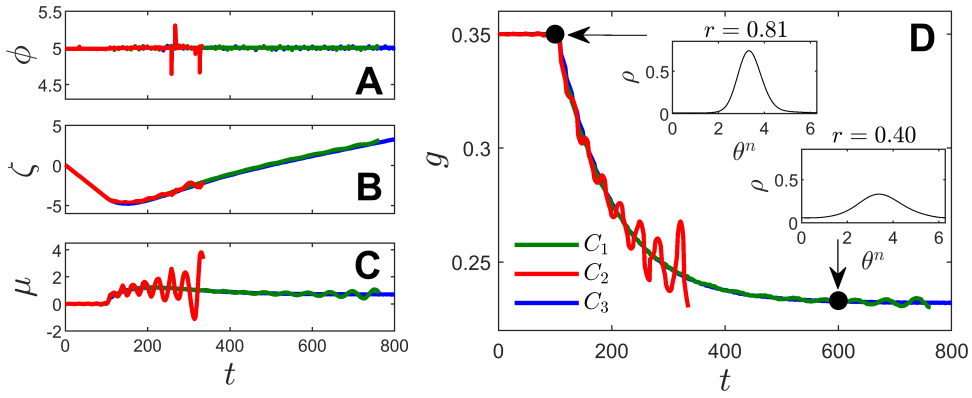

Figure 2.5: Illustration of the control strategy from Equation (2.35) applied to the Fokker-Planck equation from (2.16). Panels A, B, and C show the time course of ϕ, ζ, and μ using three different parameter sets for the constants associated with the controller. For each simulation, $\bar{s}$ as defined by Equation (2.17) is used to identify the moment that $\theta = 0$, which occurs once per cycle when $\bar{s}$ achieves a local maximum. This information is used to infer and update both ϕ and μ once per cycle. On balance, these updates are small in magnitude indicating that the averaged, reduced order equations provide a good approximation for the full order model. Panel D shows the performance of the controller with $g_{\text{targ}}(t)$ decaying slowly towards 0.232 over the course of the simulation. For the results that use parameter set C_3, the solutions of the Fokker-Planck equation are shown at $t = 100$ and $t = 600$. The associated order parameter computed according to Equation (2.22) is also indicated. Results are qualitatively similar to those from Figure 2.4, with C_1 and C_2 yielding controllers with unstable behavior.

the adaptive parameter g is shown in panel D. In this example, $g_{\text{targ}}(t) = 0.35$ for $t < 100$ and $g_{\text{targ}}(t) = 0.232 + 0.118\exp(-0.01(t - 100))$ for $t \geq 100$. Results are qualitatively similar to those from Figure 2.4 with parameter sets C_1 and C_2 yielding controllers with unstable behavior.

The implementation of the proposed control strategy from the examples in Figures 2.4 and 2.5 is predicated on the existence of a collection of periodic orbits that change continuously with respect to the adaptive parameter. In these examples, when the coupling strength g is taken to be the adaptive parameter, periodic orbits do not exist when taking $g < 0.225$. This represents a challenge when the overall goal is desynchronization, since the Kuramoto order parameter associated with the periodic orbit that emerges for $g \approx 0.225$ is still relatively large. In order to address this limitation, in the example to follow, we will assume that a less phase cohesive set of periodic orbits, x_p^γ, exists for some adaptive parameter, $p \in \mathbb{R}$. Once again, these orbits will be aligned so that $\theta = 0$ corresponds to the moment that $\bar{s}$ from Equation (2.17) reaches a local maximum. We will assume the existence of some model observable $y(t)$ such that $y(t) = p(t)$. Ultimately, we will

employ the real-time estimation strategy described in Section 2.4.2 to identify the reduced order terms used in the control strategy from Equation (2.35). Note that in this example, the adaptive parameter set will be defined implicitly. Because we will be using the model observable to infer the value of the adaptive parameter, we do not need an explicit definition for the adaptive parameter.

To proceed, we will consider simulations of the Fokker-Planck equation with the observable:

$$s_D = \max_{\theta}(\bar{s}(x_p^{\gamma}(\theta)) - \min_{\theta}(\bar{s}(x_p^{\gamma}(\theta)). \tag{2.41}$$

Here, this observable is defined to be the difference between the maximum and minimum value of $\bar{s}$ on the periodic orbit $x_p^{\gamma}(\theta)$. This definition allows for the inference from measurements of $s_D(t)$ once per cycle. Note that $\bar{s}$ still needs to be measured continuously in order to evaluate Equation (2.41). Using this strategy, the Fokker-Planck equation from (2.16) is simulated and the controller from Equation (2.35) is implemented by estimating H_1 and H_2 on a cycle-by-cycle basis. In this example, s_D takes the place of the adaptive parameter g from (2.35). For the control parameters, we use $\phi_{\text{targ}} = 5$ and take $s_{D,\text{targ}}(t) = 0.31$ for $t < 100$ and $s_{D,\text{targ}}(t) = 0.01 + 0.30\exp(-0.005(t-100))$ for $t \geq 100$. These values of $s_{D,\text{targ}}$ are chosen to be close to the nominal value that results in the absence of control for $t < 100$ and to gradually decrease towards lower values (which correspond to less synchronous solutions) over time. Controller parameters K_1, K_2, K_3, and K_4 are taken to to be 4, 30, 1, and 1, respectively. Qualitatively similar results can be obtained using other values for K_1 through K_4. Results are shown in Figure 2.6. Panels A-C show ϕ, ζ, and μ over the course of the simulation. These traces are qualitatively similar to those obtained using the C_3 parameter set from Figure 2.5. The average value of the synaptic variable and the order parameter from Equations (2.17) and (2.22), respectively, are shown in Panels D and E. Both $\bar{s}$ and r oscillate rapidly relative to the timescale shown giving the appearance of a thick line. Over the course of the simulation, the order parameter is driven below the minimum values observed in the results from Figure 2.5. Panel F shows the inferred value of $s_D(t)$ during the simulation, which gradually decays towards smaller values, as mandated by the chosen value of $s_{D,\text{targ}}(t)$. We emphasize that we are able to drive the probability distribution to less synchronous values without performing any *a priori* computations to obtain a reduced order model.

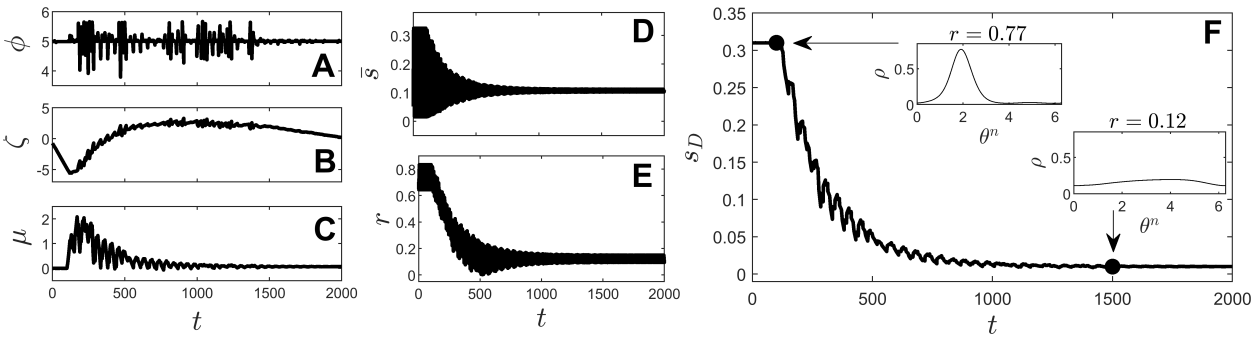

Figure 2.6: Illustration of the control strategy from Equation (2.35) applied to the Fokker-Planck equation from (2.16). The results from Figure 2.6 use an implicitly defined adaptive parameter that can be inferred from the observable defined in Equation (2.41). By simply tracking $\bar{s}$, i.e., the average value of the synaptic variable as defined in (2.17), the controller from Equation (2.35) is implemented where the terms H_1 and H_2 are approximated in real-time. Panels A, B, and C, show ϕ, ζ, and μ over the course of the simulation. Panels D and E show the corresponding values of $\bar{s}$ and the order parameter. Starting from about $r = 0.8$ at $t = 0$, the order parameter drops to approximately 0.1 after 1000 ms indicating substantial desynchronization. As the distribution approaches a less phase coherent state the input magnitude drops substantially, taking values of around $\mu = 0.06$ at $t = 2000$. The inferred value of s_D is shown in panel F during the simulation. Probability distributions are shown at $t = 100$ and $t = 1500$ giving a visual representation of the resulting desynchronization. The controller implemented here is able to drive the distribution to less synchronized solutions than the controller implemented for the results shown in Figure 2.5.

2.5.2 Control of a Large Population of Conductance-Based Neurons

Next, we consider the results of the proposed control strategy applied directly to the population of $N = 1000$ noisy, conductance-based neurons characterized by Equation (2.1) using the same values of coupling and synaptic time delay used in the results from Figure 2.1. In this example, the value of the input, I_{stim} is chosen to be identical to Equation (2.39) with the exception of taking $T_s = 10.6$ ms which is closer to the nominal period of 10.9 ms for the coupled oscillations.

Like in the example presented in Figure 2.6, we assume that a set of periodic orbits x_p^γ exists for some adaptive parameter $p \in \mathbb{R}$. We will use the observable s_D as defined in Equation (2.41) as a proxy for the adaptive parameter and employ the real-time estimation strategy described in Section 2.4.2 to identify the reduced order terms H_1 and H_2 used in the control strategy from Equation (2.35). We define $\theta = 0$ for each of these orbits to correspond to the moment that s_D crosses 0.10 with a positive slope. Once per cycle, when this $\theta = 0$ crossing is detected ϕ can

be updated using to Equation (2.23). Likewise, s_D can be updated by computing the difference between the maximum and minimum value of $\bar{s}(t)$ on the previous cycle. In-between cycles, the reduced order state variables can be updated according to the reduced order equations from (2.35) (with s_D taking the place of g).

As a first step in the implementation, the controller from Equation (2.35) is applied taking $\{K_1, K_2, K_3, K_4\} = \{4, 0, 0, 0\}$. This choice of parameters allows for direct control of ϕ (through manipulation of ζ) but does not allow for the control input μ to change. As such, by setting ϕ_{targ} to be a particular value, s_D will approach an associated region in phase space for which $\dot{s}_D = 0$. Consequently, an approximation for the nullclines of $\dot{s}_D = 0$ can be obtained by fixing a particular value of μ and slowly sweeping through different values of $\phi \in [0, 2\pi)$. These results are shown in Figure 2.7. Taking $\mu = 2$, panels A and B show the value of the order parameter computed according to Equation (2.4) and the inferred value of s_D, respectively; qualitatively similar shapes are seen in both traces. Panel C shows the nullclines that emerge for various choices of μ. For μ large enough, setting $\phi \approx 5$ completely disrupts the synchronous oscillations and no nullclines can be identified. Note that simply setting $\phi = 5$ and taking μ large enough is not a viable long-term desynchronization strategy – when oscillations are lost no information can be obtained for the reduced order model allowing oscillations to reemerge in the system due to the nominal synaptic coupling between neurons.

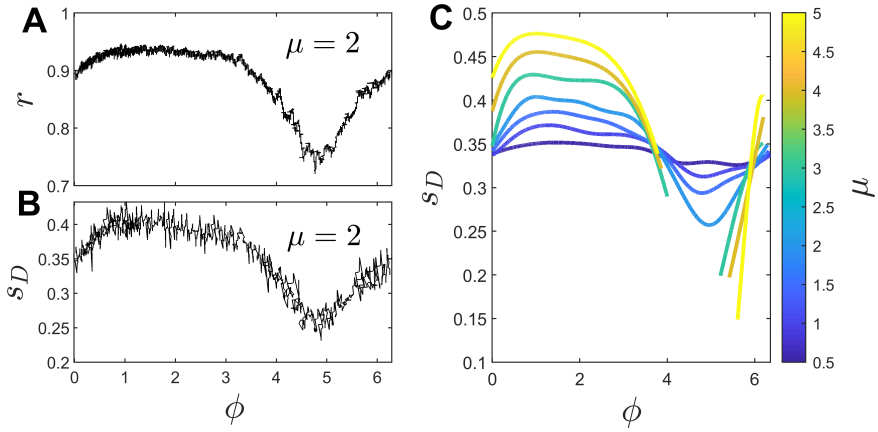

Figure 2.7: When simulating a large population of conductance-based neurons from Equation (2.1), the value of ϕ is controlled with μ held constant. By slowly sweeping from $\phi = 0$ to 2π, level sets of $\dot{s}_D = 0$ can be obtained. One such level set is shown in panel B using $\mu = 2$. The corresponding order parameter is shown in panel A. Panel C shows level sets obtained for various values of μ. Setting $\phi \approx 5$ when μ is large enough temporarily disrupts synchronization so that no level sets can be obtained.

Notice from Panel A of Figure 2.7 that the most prominent desynchronization (judging by the order parameter) occurs near values of $\phi = 5$. As such, in a full implementation of the desynchronizing controller from Equation (2.35) we choose $\phi_{\text{targ}} = 5$ radians with constants $\{K_1, K_2, K_3, K_4\} = \{4, 6, 0.18, 0.30\}$. Results are shown in Figure 2.8 for a simulation taking $s_{D,\text{targ}}(t) = 0.34$ for $t < 100$ and $s_{D,\text{targ}}(t) = 0.08 + 0.26\exp(-0.01(t - 100))$ for $t \geq 100$. These values of $s_{D,\text{targ}}$ are chosen to be close to the nominal value that results in the absence of control when $t < 100$ and to gradually decrease towards lower values (which correspond to less synchronous solutions) over time. For $t < 100$, μ is set to zero and the controller is turned off. The controller is turned on for $t \geq 100$. The black line in Panel A of Figure 2.8 shows the value of $\phi(t)$ inferred from simulations with the red line corresponding to the target value. Instantaneous updates to ϕ are made once per cycle when the threshold corresponding to $\theta = 0$ is crossed which explain

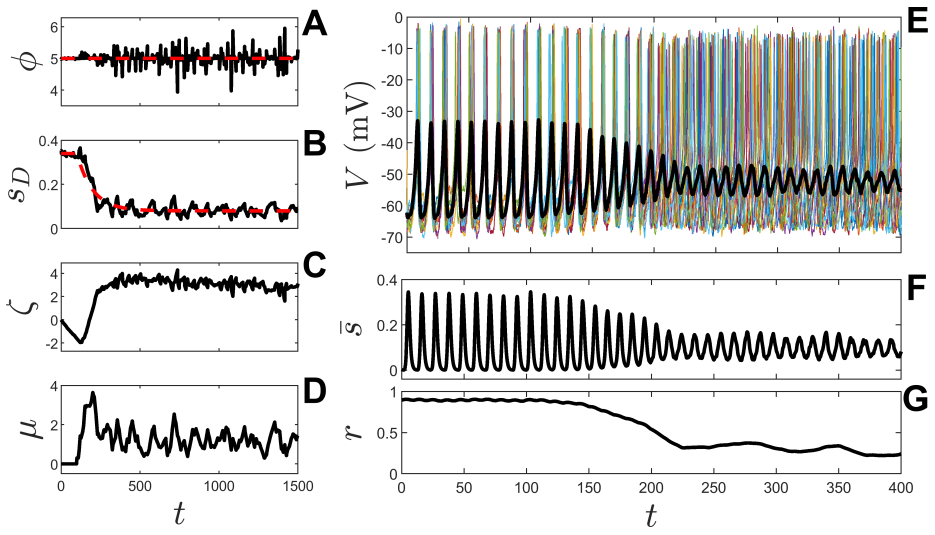

Figure 2.8: The controller given in Equation (2.35) with input given by (2.39) is implemented to desynchronize the population of $N = 1000$ synaptically coupled neurons described by Equation (2.1). Terms H_1 and H_2 of the controller are estimated using the strategy described in Section 2.4.2. Black lines in Panels A and B show values of $\phi(t)$ and $s_D(t)$ over the course of the simulation, respectively. Red lines show the corresponding values of $\phi_{\text{targ}}(t)$ and $s_{D,\text{targ}}(t)$, respectively. The phase offset and the magnitude of the input are shown in panels C and D, respectively. Disruption of synchrony can be observed in panel E, where colored lines show representative voltage traces of individual neurons and the black line shows the average transmembrane voltage of the population. Panel F shows the average value of the synaptic variable, taken to be the observable for this system when implementing the proposed strategy. Panel G shows the order parameter defined according to Equation (2.4), which falls from around 0.9 to 0.2 after the controller is turned on.

the appearance of short vertical lines in the black trace. Panel B shows the actual value of $s_D(t)$ superimposed over $s_{D,\text{targ}}(t)$. Panels C and D show the value of the phase offset and the control amplitude, respectively. When the controller is initially turned on, a relatively large value of the input magnitude, μ, is required to initiate the desynchronization; as s_D is driven to smaller values, comparatively less control input is required. Panel E shows a representative sample of the of voltage traces from the neurons in the oscillator population (colored lines) with the average value of transmembrane voltage shown in black. Disruption of the nominal synchronization is clearly observed. The average value of the synaptic current and the order parameter are shown in Panels F and G, respectively. In the absence of input, $r = 0.9$ indicating a highly synchronized population. Soon after the input is turned on and transient behavior dies out, the order parameter drops to near 0.2 where it remains indefinitely. Qualitatively similar results to those shown in Figure 2.8 can be obtained by choosing different values of K_1, K_2, K_3, and K_4. Robustness of the control algorithm is also considered by varying model parameters. For the same model used to obtain the results from Figure 2.8, representative simulations for different choices of the parameter K_1 are shown in Panels A-F of Figure 2.9. When changing one parameter at a time and keeping the rest

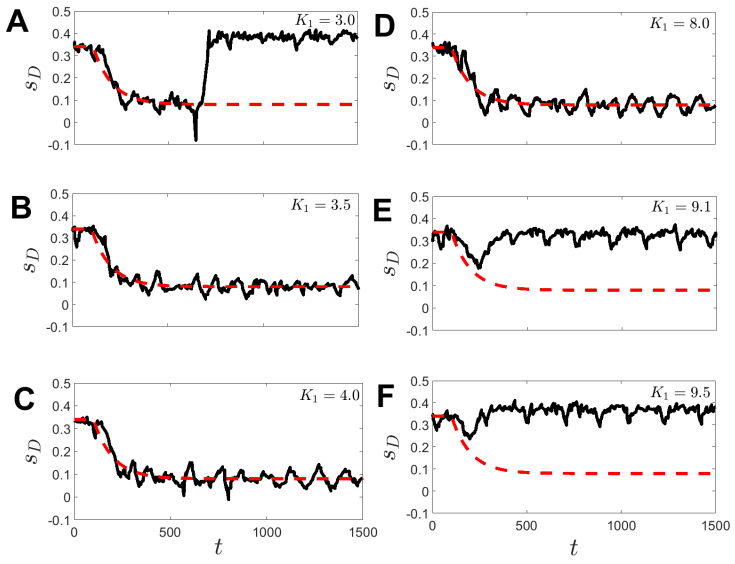

Figure 2.9: Simulations shown in Figure 2.8 are repeated for different choices of K_1. Representative results are shown here in panels A-F for the indicated values. Black and red lines show the values of $s_D(t)$ and $s_{D,\text{targ}}(t)$, respectively, for each simulation. A viable controller results for choices of $K_1 \in [3.3, 9.0]$. Robustness in response to changes in other controller parameters are reported in the text.

identical to the parameter set used in Figure 2.8, the controller is able to track the specified value of $s_{D,\text{targ}}$ for $K_1 \in [3.3, 9.0]$, $K_2 \in [3.7, 19.5]$, $K_3 \in [0.01, 0.29]$, $K_4 \in [0.19, 0.39]$, and $\phi_{\text{targ}} \in [4.6, 5.4]$. These results provide preliminary evidence that the proposed controller is robust to changes in the parameters, however, a more rigorous study of controller robustness would be warranted in future studies. Additionally, alternative implementations of the proposed control framework are also possible. Consider for instance, taking $\{K_1, K_2, K_3, K_4\} = \{4, 6, 0, 0\}$ and letting the input magnitude to saturate with limits $\mu \in [0.1, 5]$. Implementing the controller with these parameters does drive the order parameter to lower values, although, occasional short-lasting resynchronization sometimes occurs (results are not shown for this alternative parameter set).

Finally, this model independent control strategy is implemented using a modified stimulus

$$I_{\text{stim}}(t + \zeta T_s/2\pi) = \begin{cases} \mu, & \text{if } \text{mod}(t + \zeta T_s/2\pi, T_s) < 4 \\ & \text{and } \text{mod}(t + \zeta T_s/2\pi, 1) < 0.5, \\ -\mu, & \text{if } 4 \leq \text{mod}(t + \zeta T_s/2\pi, T_s) < 8 \\ & \text{and } \text{mod}(t + \zeta T_s/2\pi, 1) < 0.5, \\ 0, & \text{otherwise.} \end{cases} \tag{2.42}$$

Instead of a series of only positive pulses, Equation (2.42) mandates an alternating set of positive and negative pulses. For a constant value of μ, this stimulation protocol would yield a charge balanced stimulus which is a practical requirement in clinical settings to mitigate Faradaic reactions that damage both the surrounding brain tissue and the DBS probe [72], [50]. For a nonstatic choice of μ, the input will be nearly charge balanced. Note that Equation (2.42) does not describe a standard biphasic pulse [14], but nonetheless will have a substantially smaller accumulation of charge than the monophasic pulses from Equation (2.39). Results are shown in Figure 2.10 using the pulses mandated by Equation (2.42) and taking $\phi_{\text{targ}} = 0.5$ radians with all other parameters taken identical to those from Figure 2.8. Once again, the controller is turned on at $t = 100$ ms. Panels A-C show ϕ, s_D, and $I_{\text{stim}}(t)$ over the course of a representative simulation. Panels D-F show voltage traces, $\bar{s}$, and the order parameter, respectively, over the first 400 ms of simulation. Despite the use of a different input, the results from Figure 2.10 are qualitatively similar to those from Figure 2.8.

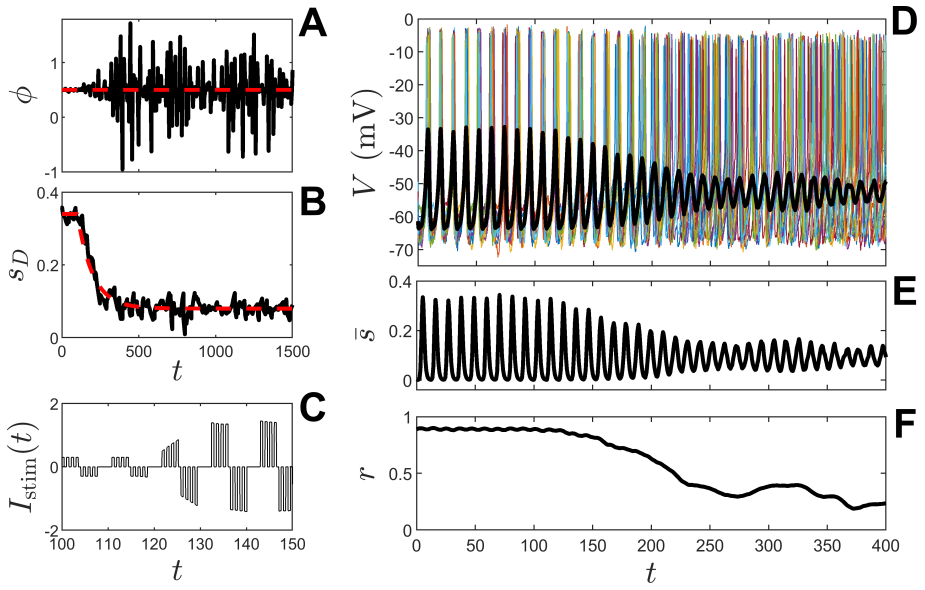

Figure 2.10: The controller from Equation (2.35) using a nearly charge-balanced stimulation mandated by Equation (2.42) is implemented to desynchronize the population of $N = 1000$ synaptically coupled neurons described by Equation (2.1). The controller is turned on at $t = 100$ ms. Black lines in Panels A and B show values of $\phi(t)$ and $s_D(t)$ over the course of the simulation, respectively. Red lines show the corresponding values of $\phi_{\text{targ}}(t)$ and $s_{D,\text{targ}}(t)$, respectively. Panel C shows the applied stimulation immediately after the controller is turned on. Disruption of synchrony can be observed in panel D, where colored lines show representative voltage traces of individual neurons and the black line shows the average transmembrane voltage of the population. Panel E shows the average value of the synaptic variable, taken to be the observable for this system when implementing the proposed strategy. Panel F shows the order parameter during the simulation defined according to Equation (2.4).

2.6 Discussion and Conclusion

In this work, we develop a closed-loop control framework that can be used to manipulate the behavior of large populations of coupled neurons using near-periodic inputs, i.e., inputs with the general form given in Equation (2.2) that are nominally periodic but with the incorporation of a slowly varying phase offset and a slowly changing amplitude. This work can be viewed as potential theoretical underpinning for the phase-specific aDBS application strategies that have gained interest in recent years [101], [15], [38]; here, the slowly varying phase offset can be used to coordinate the timing of the DBS stimulus relative to some measured observable. In this work, our primary control objective is to engender desynchronization, however, other control objectives could conceivably be considered using this strategy. Additionally, this general framework could potentially be used in

other applications, for instance, in conjunction with non-invasive stimulation therapies [96] by using accelerometer data from tremor patients as an observable used to define the phase and amplitude of the oscillation.

We employ a series of model transformations and reductions in the analysis performed in this work. Starting with a large population of conductance-based neurons from Equation (2.1), we represent the behavior in the large N limit using the Fokker-Planck equation (2.16). The adaptive phase-amplitude reduction paradigm [138], [137] is used to analyze the temporal evolution of the Fokker-Planck equation in terms of a low-order reduction and formal averaging techniques [105], [31] are used to ultimately arrive at an analytically tractable reduced-order model of the form (2.32). A relatively simple controller of the form (2.35) is subsequently proposed to manipulate the state variables of the reduced order model. As illustrated in the results, by simply manipulating the phase offset and the magnitude of the periodic input, the variables of the reduced order model can be controlled successfully.

In comparison to other proposed closed-loop DBS strategies, the proposed method is most similar to phase-triggered methods [128], [127], [19], [39], [7]. Such methods seek to apply a control input at an appropriate phase of oscillation in order to reduce the degree of synchronization in the overall population. In contrast to these other phase-triggered methods, here we use a rotating reference frame (i.e., defined in Equation (2.23)) that considers the offset, ϕ, between the population phase θ and the phase of the periodic input. By appropriately manipulating ϕ, the population oscillation can be driven to less synchronous states. Also, we note the differences between the proposed method and delayed feedback approaches detailed in [99], [88], [107] which can generally be implemented by applying a feedback signal $I_{\text{stim}}(t) = K(y(t-\tau) - y(t))$ where τ and K are a time delay and a proportional gain, respectively, and $y(t)$ is some observable. With an appropriate observable that provides a good representation of the population level behavior, it is often possible to find some combination of τ and K that can yield desynchronization. Extensions that use nonlinear delayed feedback [87] or charge-balanced pulses [89] are also possible. In contrast to the method presented in this work, delayed-feedback approaches do not require an *a priori* specification of the applied DBS waveform.

While the terms of the averaged, reduced order model derived in this work can be computed numerically according to the integrals from Equation (2.26), they do result after a long series of transformations and reductions. Errors associated with these transformations will compound at each step. Additionally, in general, the underlying model equations can either be unavailable or can

be too complicated to numerically compute the terms of the reduction. For this reason, the real-time strategy for estimation of the terms of the reduced order model as described in Section 2.4.2 would be essential for practical implementation of the proposed control strategy. Indeed, using this strategy, coupled oscillations in the full order model from Equation (2.1) can be disrupted without knowledge of the underlying model equations. In the examples considered in this work, we use the average value of the time-delayed synaptic variable as defined in Equation (2.3) as a system observable. In experimental applications, the proposed control strategy could potentially be implemented using accelerometer measurements from hand tremors or measurements LFP power spectrum data.

There are many limitations of the proposed control strategy that are not addressed here. For the purposes of this work, parameter sets for the proposed controller are identified by first determining an adequate choice of ϕ_{targ} for which the application of the near-periodic input has a desynchronizing influence. The remaining parameters were obtained using a trial-and-error approach. In future work, it would be of interest to provide a more careful analysis of this control strategy to investigate questions related to controllability and optimality. An additional limitation of the proposed control strategy is that it requires measurable oscillations to be present at all times. As a consequence of this assumption, synchronization cannot be completely abolished. For instance, when $s_{D,\text{targ}}$ is set to values below 0.08 in the results shown in Figure 2.8, oscillations can occasionally become difficult to identify subsequently degrading the real-time estimates of ϕ, s_D, H_1, and H_2. When this happens, the neural population can transiently resynchronize until accurate estimates for these terms can be reobtained and the controller can regain its efficacy. Future work will investigate strategies to mitigate this issue, for instance, by investigating strategies to stabilize the fully desynchronized state. In the examples presented in this work, it is assumed that all but one of the isostable (amplitude) coordinates in Equation (2.20) decay rapidly so that they can be ignored. As illustrated in panel B of Figure (2.2), this assumption is explicitly validated for the discretized version of of the Fokker-Planck equation from Equation (2.19) for the model used in this study. Numerical illustrations of the proposed control strategy are performed using a single population of identical neurons (2.1) that do not contain a realistic description of the overall brain circuit that is relevant to clinical DBS. It is likely that models with more complicated coupling structures and models with multiple interacting subpopulations may require the inclusion of additional amplitude coordinates, thereby complicating the analysis. Investigation of the proposed control strategy in a more realistic model would be warranted. Additionally, numerical illustrations in this work use the average value

of the synaptic variable as an observable used to define the phase and amplitude of oscillations. In practical applications, such information is not readily available. This would necessitate the use of other biomarkers such as beta band LFP power. Additional issues created by both measurement noise and delays between the application of stimulation and the effect on system observables would likely need to be considered in practical applications.

Chapter 3

The Influence of Synaptic Plasticity on Critical Coupling Estimates for Neural Populations

The content and figures in this chapter are published in [117] and reproduced with permission from Springer Nature.

3.1 Introduction

Neural synchrony is thought to play a key role in cognitive processing [36], [110], is a hallmark of the neural dysfunction that manifests in Parkinson's disease [131], [86], and is essential in the maintenance of circadian rhythms [97], [27]. Synchronization among large populations of coupled neurons has been widely studied from a dynamical systems perspective, yielding insight into the mechanisms by which neural synchronization emerges in conductance-based models of tonically firing neurons [10], [40], [22], [121], [21], [34], and providing insight into strategies by which pathological synchronization can be suppressed [94], [39], [116], [134]. The vast majority of the phase-based analysis of neural oscillators, however, neglects the influence of synaptic plasticity. Often summarized by the aphorism: 'neurons that fire together, wire together', synaptic plasticity refers to the widely observed characteristic of real neurons to modify the strength of synaptic connections over time in response to the relative firing time between neurons [37], [46], [47]. Recent evidence suggests synaptic plasticity is critical to the brain's ability to learn from memory [46]

motivating its implementation in artificial spiking neural networks to develop machine learning algorithms capable of pattern, image, and feature recognition [66], [42].

Incorporation of spike-timing dependent plasticity (STDP) in computational models of synaptically coupled populations of neurons can have profound effects on their collective behavior. This point is illustrated by numerical simulations summarized in Figures 3.1 and 3.2 for a population of $N = 5$ homogeneous neurons of the form

$$C\dot{V}_i = -I^i_{ion} - \frac{1}{N-1}\sum_{j\neq i} I^{j\to i}_{syn}, \tag{3.1}$$

for $i = 1, \ldots, N$, where V_i is the neural membrane potential (in mV), I^i_{ion} represents the ionic

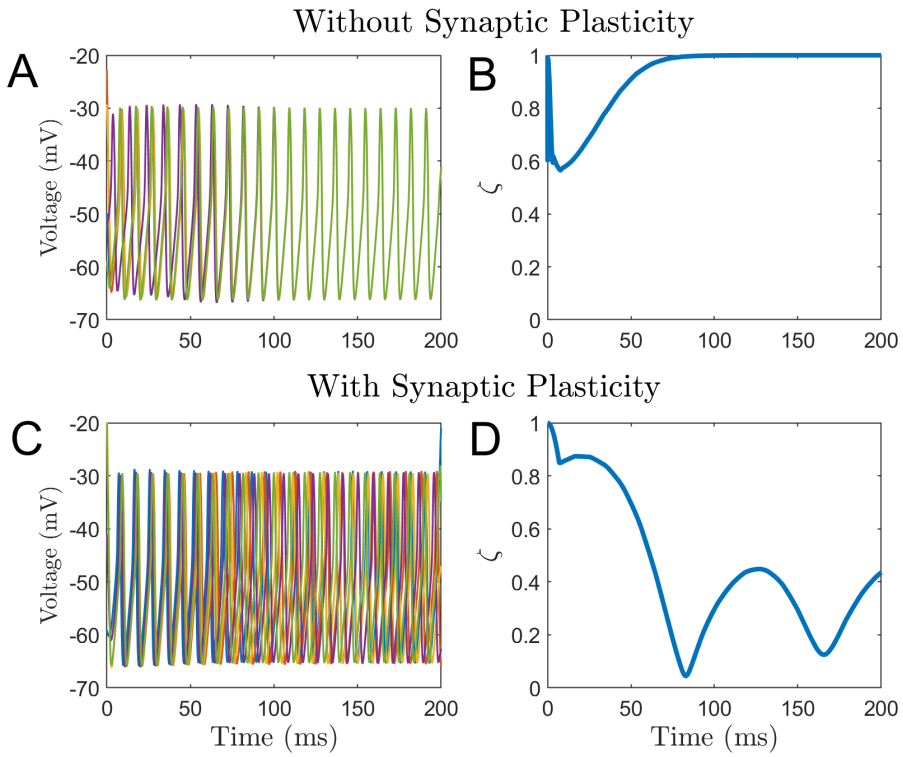

Figure 3.1: Representative simulations for an inhibitory neural population with and without synaptic plasticity. Panel A shows the voltage dynamics of a homogeneous population of five neurons with inhibitory coupling and a static synaptic coupling strength of $Kg_{j\to i} = 0.1\text{mS/cm}^2$ for all i and j. Panel B shows the corresponding Kuramoto order parameter indicating stable synchronization. Panel C shows the voltage dynamics of the same network with Hebbian STDP where $g_{j\to i} \in [0, 1]$ is allowed to change in time as described in Section 3.2.2. Panel D shows the associated Kuramoto order parameter.

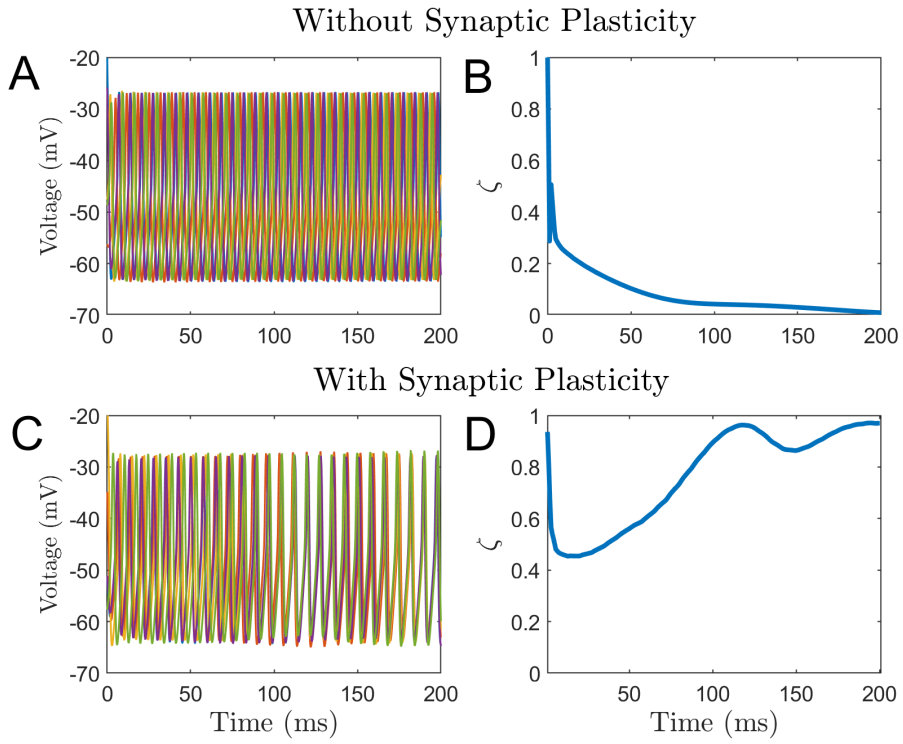

Figure 3.2: Representative simulations for an excitatory neural population with and without synaptic plasticity. Panel A shows the voltage dynamics of a homogeneous population of five neurons with excitatory coupling and a static synaptic coupling strength of $Kg_{j\to i} = 0.1\text{mS/cm}^2$ for all i and j. Panel B shows the associated Kuramoto order parameter indicating near complete desynchronization. Panel C show the voltage dynamics of the same network with Hebbian STDP where $g_{j\to i} \in [0, 1]$ is allowed to change in time as described in Section 3.2.2 and Panel D gives the corresponding Kuramoto order parameter.

current derived from the neuron's internal dynamics, $I_{syn}^{j\to i}$ represents the synaptic current from the presynaptic neuron j to the postsynaptic neuron i, and C is the constant membrane capacitance. Since self coupling is not considered here, the $I_{syn}^{j\to i}$ term is scaled by $1/(N-1)$ and not $1/N$. The synaptic current is [22]

$$I_{syn}^{j\to i} = Kg_{j\to i}(t)s_j(t)(V_i - E_{syn}), \tag{3.2}$$

where $K > 0$ is a maximum synaptic conductance, $g_{j\to i} \in [g_{min}, 1]$ is governed by a Hebbian STDP rule where the update is a function of the current weight of the synaptic connection and the time difference between spikes [118], s_j is a synaptic variable associated with neuron j, and E_{syn} is the reversal potential that governs whether coupling is inhibitory or excitatory. A complete description of the model parameters can be found in Section 3.2. Figures 3.1 and 3.2 present

the voltage dynamics and the corresponding Kuramoto order parameter using inhibitory and excitatory coupling, respectively. The Kuramoto order parameter, ζ, is used to quantify the level of synchronization with $\zeta = 1$ indicating complete synchronization and lower values indicating less synchronization in the network (the full definition of the order parameter for this network is given in Equation (3.10)). In both figures, panels A and B show the results with static coupling. Panels C and D in each figure provide the same information when using a Hebbian STDP rule instead. In both simulations, stability of the synchronous state depends on the presence or absence of synaptic plasticity in the network leading to substantial changes in the aggregate behavior. Figures 3.1 and 3.2 demonstrate that the presence or absence of synaptic plasticity can have a substantial influence on the aggregate behavior of a coupled population of neurons. Figure 3.1 demonstrates that a population of inhibitory neurons with static synaptic coupling and dynamics governed by (3.1) and (3.2) will tend toward a stable synchronized state. However, the inclusion of STDP prohibits this same population from synchronizing. Figure 3.2 illustrates that a homogenous population of excitatory neurons with static synaptic coupling and dynamics governed by (3.1) and (3.2) will tend toward a stable antiphase state. However, the inclusion of STDP allows this same population to reach a phase cohesive state.

While the dynamics that govern synaptic plasticity are well documented [18] and often included in computational studies, its influence on network synchronization is of particular interest in this work. Reference [79] concludes that STDP enhances neural synchronization when compared to populations of neurons without plastic synaptic coupling in results obtained on a hybrid network comprised of a spike generator, a clamp to simulate an excitatory synapse, and a neuron from an *Aplysia* abdominal ganglion. Reference [45] analyzes the parameters and factors that contribute to the development of a stable synchronized state in a population of heterogeneous excitatory oscillators coupled with STDP. Reference [57] studies the emergence of distributed synchrony throughout a population of coupled neurons with STDP. Reference [63] discusses bifurcations in stability that occur among populations of Kuramoto oscillators coupled with STDP as the synaptic potentiation and depression windows change, with a stable synchronous state existing above some threshold coupling strength for equal window lengths and the emergence of multistability with asymmetric windows. Reference [81] analyzes how various parameters affect both the induction and retention of phase and period locking in a two-neuron network with plastic synaptic connections, and reference [47] focuses on the effect of the axonal delay in a network of conductance-based neural oscillators with plastic synaptic connections in the context of the critical brain hypothesis

[56], [17]. In this work, we are primarily focused on understanding the synchronization (or lack thereof) that emerges in large populations of neurons with synaptic connections that are subject to Hebbian STDP rules as illustrated, for instance, in Figures 3.1 and 3.2. While much research has been conducted on the implications of STDP on synchronization, none has addressed the existence of a threshold critical coupling strength for phase cohesion and the conditions which would affect this critical coupling strength. This work extends prior work from [142] to investigate the impact of Hebbian STDP on the critical coupling strength required to maintain phase cohesion.

Extending prior results from [142] that did not consider STDP, we derive upper bounds for the critical coupling strength required to maintain phase cohesion in a network of neurons with excitatory coupling and STDP. Note here that the critical coupling strength is the minimum coupling strength required to retain phase cohesion. Here, a population of oscillators is considered phase cohesive if the phase difference between any two oscillators remains bounded within a prespecified arclength. Critically, we find that the presence or absence of STDP can lead to qualitatively different collective behavior of the aggregate population. Our analysis highlights the importance of the relative ordering between phase cohesive neurons and that order switching can degrade the synchronizing influence of coupling when STDP is considered. The organization of this paper is as follows: in Section 3.2 we provide necessary background on the neural models used in this study in addition to the phase reduction techniques used to represent the oscillatory dynamics with a low order basis. In Section 3.3 we derive upper bounds on the critical coupling strength to maintain phase cohesion. Section 3.4 shows the result of numerical simulations validating our analytical results, and Section 3.5 provides concluding remarks.

3.2 Background

3.2.1 Neural Model Equations

The theoretical analysis presented in this work can be applied to any tonically firing conductance-based neural model. For concreteness, and for the purposes of illustration, we will consider a

synaptically coupled model of a population of thalamic neurons from [103]

$$
\begin{aligned}
C\dot{V}_i &= -I_L(V_i) - I_{Na}(V_i, h_i) - I_K(V_i, h_i) - I_T(V_i, r_i) + I_{stim,i} - \frac{1}{N-1}\sum_{j\neq i} I_{syn}^{j\to i}(s_j, V_i), \\
\dot{h}_i &= (h_\infty - h_i)/\tau_h, \\
\dot{r}_i &= (r_\infty - r_i)/\tau_r, \\
\dot{s}_i &= \frac{c_1(1-s_i)}{1+\exp(-(V_i - V_T)/\sigma_T)} - c_2 s_i,
\end{aligned} \tag{3.3}
$$

for $i = 1, \ldots, N$. Above, V_i denotes the transmembrane voltage of neuron i, h_i and r_i are associated gating variables, s_i is a state variable used to determine the synaptic current, and $C = 1\mu\text{F/cm}^2$ is the constant membrane capacitance. The synaptic current $I_{syn}^{j\to i}$, was defined in Equation (3.2). Parameters that govern the dynamics of the synaptic variable are $c_1 = 3$ ms^{-1}, $c_2 = 0.3$ ms^{-1}, $V_T = -20$ mV, and $\sigma_T = 0.8$ mV. The form of Hebbian plasticity implemented in this model is discussed in the next subsection. I_L, I_{Na}, I_K, and I_T are the leak, sodium, potassium, and low-threshold calcium ionic currents, respectively, with dynamics

$$
\begin{aligned}
I_L(V) &= g_L(V - E_L), \\
I_{Na}(V, h) &= g_{Na}(m_\infty^3)h(V - E_{Na}), \\
I_K(V, h) &= g_K((0.75(1-h))^4)(V - E_K), \\
I_T(V, r) &= g_T(p_\infty^2)r(V - E_T),
\end{aligned} \tag{3.4}
$$

where $g_L = 0.05$ mS/cm^2, $g_{Na} = 3$ mS/cm^2, $g_K = 5$ mS/cm^2, $g_T = 5$ mS/cm^2, $E_L = -70$ mV, $E_{Na} = 50$ mV, $E_K = -90$ mV, and $E_T = 0$ mV. $I_{stim,i} \in [4.84, 5.16]$ is a baseline current applied to neuron i chosen so that the individual neurons are in a tonically firing regime. For homogeneous cases, $I_{stim,i} = 5$ for all N neurons. However, we will ultimately be looking specifically at situations where $I_{stim,i}$ is different between neurons yielding a heterogeneous population. Auxiliary functions are given below:

$$
\begin{aligned}
h_\infty &= 1/(1+\exp((V+41)/4)),\\
r_\infty &= 1/(1+\exp((V+84)/4)),\\
\alpha_h &= 0.128\exp(-(V+46)/18),\\
\beta_h &= 4/(1+\exp(-(V+23)/5)),\\
\tau_h &= 1/(\alpha_h+\beta_h),\\
\tau_r &= 28+\exp(-(V+25)/10.5),\\
m_\infty &= 1/(1+\exp(-(V+37)/7)),\\
p_\infty &= 1/(1+\exp(-(V+60)/6.2)).
\end{aligned}
\tag{3.5}
$$

3.2.2 Modeling Synaptic Plasticity

To incorporate synaptic plasticity, we consider a soft bound spike-timing dependent plasticity (STDP) rule [47]. In the context of Equation (3.2), the STDP is incorporated by updating $g_{j\to i}(t) \in [g_{min}, 1]$ each time either neuron i or j spike. We specifically register an action potential or spike time whenever $V_i = -30$ mV and $\dot{V}_i > 0$. For two arbitrary neurons i and j, letting t_i be the time that neuron i spikes and t_j be the time that neuron j most recently spiked, immediately after neuron i spikes, both $g_{j\to i}(t)$ and $g_{i\to j}(t)$ are updated according to

$$
g_{\alpha\to\beta}(t_i^+) = \begin{cases}
g_{\alpha\to\beta}(t_i^-) + A_+(1-g_{\alpha\to\beta}(t_i^-))e^{\frac{-\Delta t_{\alpha\to\beta}}{\tau_+}}, & 0 < \Delta t_{\alpha\to\beta} < t_c,\\
g_{\alpha\to\beta}(t_i^-) - A_-(g_{\alpha\to\beta}(t_i^-) - g_{min})e^{\frac{\Delta t_{\alpha\to\beta}}{\tau_-}}, & -t_c < \Delta t_{\alpha\to\beta} \le 0,\\
g_{\alpha\to\beta}(t_i^-), & |\Delta t_{\alpha\to\beta}| \ge t_c,
\end{cases}
\tag{3.6}
$$

where $\alpha = \{i, j\}$, $\beta = \{j, i\}$, and $\Delta t_{\alpha\to\beta} = t_\beta - t_\alpha$. Above, g_{min} is a lower bound on the synaptic strength (typically at or near 0). The magnitude of each update is determined by the amplitudes $A_+ = A_- = 2$, and the size of the synaptic potentiation and depression learning windows are set by $\tau_+ = \tau_- = 10$ ms. Note that the assumptions $A_+ = A_-$ and $\tau_+ = \tau_-$ are simplifications made for this particular model and not representative of biologically realistic values. We assume here that the synaptic potentiation and depression windows are equal in size, although these values could be changed as desired in the model.

For the synaptic update to occur, there must be some indication of a causal or noncausal relationship between the presynaptic neuron firing and the postsynaptic neuron firing. In this case, if $\Delta t_{\alpha\to\beta}$ falls within a predefined time window $|\Delta t_{\alpha\to\beta}| < t_c$, the synaptic update specified in Equation (3.6) will occur. When $0 < \Delta t_{\alpha\to\beta} < t_c$, the presynaptic neuron fires before the postsynaptic neuron so that the relationship is causal and the synaptic strength of that relationship will correspondingly increase. Conversely, if $-t_c < \Delta t_{\alpha\to\beta} \leq 0$ (meaning that the postsynaptic neuron fires before or at the same time as the presynaptic neuron), the relationship between the neurons is noncausal and the synaptic strength will decrease [82]. Outside of the $|\Delta t_{\alpha\to\beta}| < t_c$ window, no update will occur. Note that the t_c value should be selected so that a single firing relationship is not classified as both causal and noncausal over the same firing period; that is, t_c should be less than $T/2$, where T is the average period of of the coupled oscillators. In our model, we elect to use $t_c = 3$ms since the average period of the coupled oscillators (corresponding to $I_{stim} = 5$) is approximately 8.4ms. In simulations with static synaptic connections, for instance from Figures 3.1 and 3.2, $g_{\alpha\to\beta} = 1$ for all α and β.

3.2.3 Phase Reduction

Weakly perturbed limit cycle oscillators can be written in a reduced order form using phase reduction. Consider a general dynamical system of the form

$$\dot{x} = F(x) + \epsilon u(t), \tag{3.7}$$

where $x \in \mathbb{R}^N$ is the state, F sets the dynamics, u is an external perturbation, and $0 < \epsilon \ll 1$. Suppose that when $u = 0$, Equation (3.7) has a stable T-periodic limit cycle x^γ, with $T = 2\pi/\omega$. States on the limit cycle can be mapped to a phase $\theta \in [0, 2\pi)$ which is scaled so that $\dot{\theta} = \omega$ where $\omega = 2\pi/T$. Using isochrons to extend phase to the basin of attraction of the limit cycle and changing variables to phase coordinates (see, for instance [22], [75]), the phase dynamics when $u(t) \neq 0$ can be represented according to

$$\dot{\theta} = \omega + \epsilon \frac{\partial \theta}{\partial x} \cdot u(t), \tag{3.8}$$

where the gradient is evaluated on the periodic orbit at $x^\gamma(\theta)$ and the dot denotes the dot product. In the context of the neural model (3.3), for neuron i, $F(x)$ denotes everything except for the

synaptic current and $u(t)$ is comprised of only the synaptic current received by neuron i. Writing Equation (3.3) in phase reduced form yields

$$\dot{\theta}_i = \omega_i - \frac{\epsilon}{N-1} \sum_{j \neq i} Z_i(\theta_i) \hat{K} g_{j \to i}(t) s_j(t) (V_i - E_{syn}), \tag{3.9}$$

for $i = 1, \ldots, N$ where $Z_i(\theta_i)$ is the gradient of the phase with respect to voltage perturbations evaluated on the limit cycle of the i^{th} neuron and $\hat{K} = \frac{K}{\epsilon C} > 0$. We explicitly assume that $\hat{K} = O(1)$ so that the overall input is an order ϵ term. The phase response curve can be calculated numerically using the adjoint equation or from data; we refer the interested reader to [75] or [146] for more information on phase reduction techniques pertaining to neuroscience applications.

With a phase reduced model that can accurately reflect the dynamics of the full order model, we can consider the Kuramoto order parameter to assess the level of synchronization of the overall population:

$$\zeta = \left| \frac{1}{N} \sum_{i=1}^{N} e^{i\theta_i} \right|. \tag{3.10}$$

When $\zeta = 1$ the system (3.9) is fully synchronized. Values of ζ closer to zero generally indicate less synchronization in the overall network but can also correspond to rotating block states (see for instance, [6]). We consider the Kuramoto order parameter in Figures 3.1 and 3.2 to be a general gauge of synchronization. Note that the phase is not directly measurable for simulations of (3.3); in this case, we take $\theta_i = 0$ to correspond to the moment that neuron i spikes and linearly interpolate all phases in between to compute (3.10).

3.3 Upper Bounds for the Critical Coupling Strength for a Population of Coupled Neurons with Synaptic Plasticity

Consider a population of N tonically firing neurons of the form (3.3) with a Hebbian STDP update rule of the form (3.6). After phase reduction, the dynamics can be represented according to Equation (3.9) as described in Section 3.2.3 with natural frequency $\omega \in [\omega_{min}, \omega_{max}]$. Define $\omega_0 = (\omega_{min} + \omega_{max})/2$. In this work, we use the notion of phase cohesion to characterize synchronization of the population. A population is phase cohesive at time t if there exists some

arclength $\nu(t) \in [0, \pi)$ that contains θ_i for all $i = 1, \ldots, N$. Figure 3.3 provides an illustration of phase cohesion with a population $N = 5$ neural oscillators.

The goal here is to identify an upper bound on the critical coupling strength for phase cohesion. This critical coupling strength, $K_{crit}(\nu)$, is defined such that if $\hat{K} \geq K_{crit}(\nu)$, then a phase cohesive population of N neurons contained within an arclength ν will remain phase cohesive within that arclength for all forward time. To begin, let $\phi_i \equiv \theta_i - \omega_0 t$, where ϕ is a residual phase when working in a rotating reference frame [45]. Working in this rotating reference frame, the dynamics of (3.9) become

$$\dot{\phi}_i = \Delta\omega_i - \epsilon \frac{\hat{K}}{N-1} \sum_{j \neq i} Z_i(\theta_i) g_{j \to i}(t) s_j(\theta_j)(V_i(\theta_i) - E_{syn}), \tag{3.11}$$

where $\Delta\omega_i = \omega_i - \omega_0$. Again, defining a new variable, $\psi_{i,j} = \phi_i - \phi_j$, we can write Equation (3.11) in terms of the phase difference between neurons i and j.

$$\begin{aligned} \dot{\psi}_{i,j} =& \omega_i - \omega_j - \epsilon \frac{\hat{K}}{N-1} \sum_{k \neq i} \left[Z_i(\theta_i) g_{k \to i}(t) s_k(\theta_k)(V_i(\theta_i) - E_{syn}) \right] \\ &+ \epsilon \frac{\hat{K}}{N-1} \sum_{k \neq j} \left[Z_j(\theta_j) g_{k \to j}(t) s_k(\theta_k)(V_j(\theta_j) - E_{syn}) \right]. \end{aligned} \tag{3.12}$$

In Equation (3.12), we have designated the i^{th} and j^{th} neurons to be arbitrary neurons that are presently at the leading and lagging edges of a population (neurons 1 and 5 in Figure 3.3). The

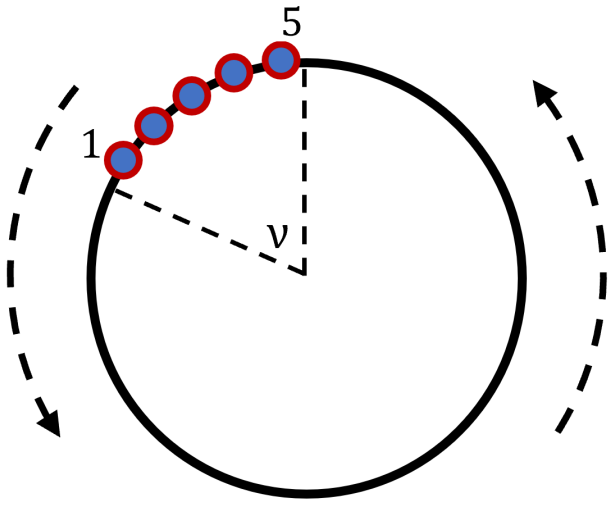

Figure 3.3: Phase cohesion in a population of five neural oscillators. The phase of each oscillator is contained within the arclength ν.

phase difference dynamics of any other pair of neurons contained within this population will be bounded above by the phase difference dynamics of these edge neurons.

3.3.1 A Limiting Value of Synaptic Conductance When Spike Order is Preserved

To simplify (3.12), we next focus on the impact of synaptic plasticity. If two tonically-firing coupled neurons have nonidentical spike times, we define the leading neuron to be the neuron which spikes first in a given limit cycle with spike time t_{lead}, and the lagging neuron to be the neuron which spikes some time later with spike time t_{lag}, so that $0 < t_{lag} - t_{lead} < T/2$. Recall that each pair of neurons has a synaptic relationship which updates reciprocally; in our two neuron example, this means that when the relationship from the leading neuron to lagging neuron is strengthened, the relationship from the lagging neuron to the leading neuron is weakened. With this in mind, consider two neurons with phases θ_m and θ_n where neuron m, the leading neuron, always spikes before neuron n, the lagging neuron. Considering the update rule from (3.6), and provided ν is small enough at some initial time $t = 0$ so that the time between neuron m spiking and neuron n spiking is smaller than t_c, that is $0 < t_n - t_m < t_c$, then $g_{m\to n}$ and $g_{n\to m}$ will update reciprocally when the current lagging neuron (neuron n) fires, and $\lim_{t\to\infty}(g_{m\to n}) = 1$ while $\lim_{t\to\infty}(g_{n\to m}) = g_{min}$ regardless of initial conditions. With this in mind, for any initial condition $g_{m\to n}(0)$, where m is the leading neuron and n is the lagging neuron for all $t \geq 0$, let $t_s^{m\to n}$ be the maximum possible time required so that $|g_{m\to n}(t) - 1| \leq M$ where $M > 0$ is an order ϵ term. Correspondingly, for any initial condition $g_{n\to m}(0)$ let $t_s^{n\to m}$ be the maximum possible time required so that $|g_{n\to m}(t) - g_{min}| \leq M$. Finally, we define

$$t_s = \max(t_s^{n\to m}, t_s^{m\to n}). \tag{3.13}$$

Intuitively, t_s is defined so that if neuron m always spikes before neuron n on any time interval of length t_s, then $g_{m\to n}$ will be within order ϵ of its maximum value and $g_{n\to m}$ will be within order ϵ of g_{min} at the end of that time interval.

In simulations of the neural model with synaptic plasticity (3.3), for instance, shown in Figures 3.1 and 3.2, and shown in detail in Figure 3.4, the firing order of neurons is capable of changing over time. To accommodate this feature, we define two new variables to track potential order changes

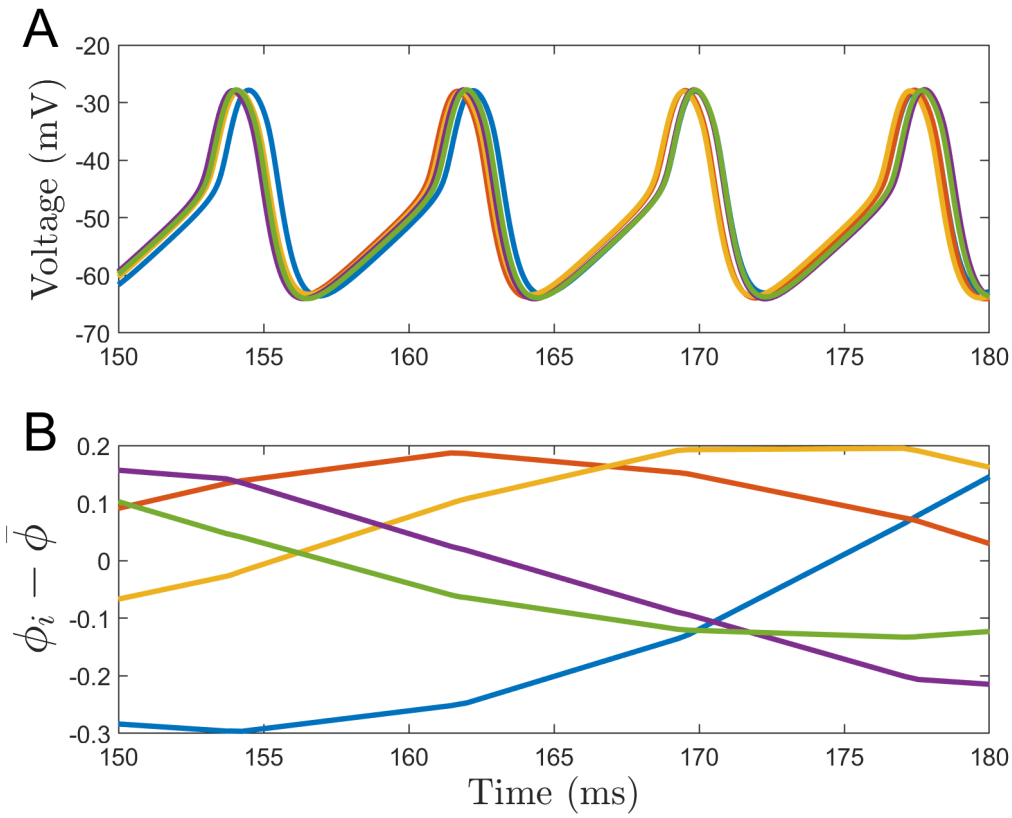

Figure 3.4: A 30 ms window from a single simulation of $N = 5$ excitatory neurons with dynamics governed by (3.3) and the synaptic update rule in (3.6). Ordinal switches can be clearly seen in the full order model in panel A and the phase reduced model in panel B. In the phase reduced model, ϕ_i was computed by interpolating the phase from each neuron's respective spike times in the corresponding full order model and $\bar{\phi}(t) = \frac{1}{N}\sum_{i=1}^{N}\phi_i(t)$.

in a given time window of duration τ:

$$\rho_{i,j}(t,\tau) = \begin{cases} 1, & \text{if } \theta_j(t) = \theta_i(t) \text{ for any } t \in [t-\tau, t], \\ 0, & \text{otherwise,} \end{cases} \tag{3.14}$$

$$\eta_i(t,\tau) = \sum_{j \neq i} \rho_{i,j}(t,\tau). \tag{3.15}$$

Above, Equation (3.14) tracks whether the order of θ_j and θ_i could have switched on the given time interval while (3.15) gives the sum of all possible ordinal switches for neuron i within that same time interval. We emphasize that the maximum value of $\rho_{i,j}(t,\tau)$ is 1, even if multiple switches occur on the given time interval.

An illustrative example of this strategy is provided in Figure 3.5 taking $\tau = 25$ for a population of $N = 25$ neurons. The leading (resp. lagging) edge is highlighted in panel A (resp., B). In panel A (resp., B), the black line highlights the phase of a neuron that is leading (resp., lagging) at some point in the simulation; the line is solid at all moments that the neuron is leading (resp., lagging) and dashed otherwise. In panels A and B, the phases of other neurons that change order relative to the black trace (yielding nonzero $\rho_{i,j}$) are shown in color, while all others appear in grey. All

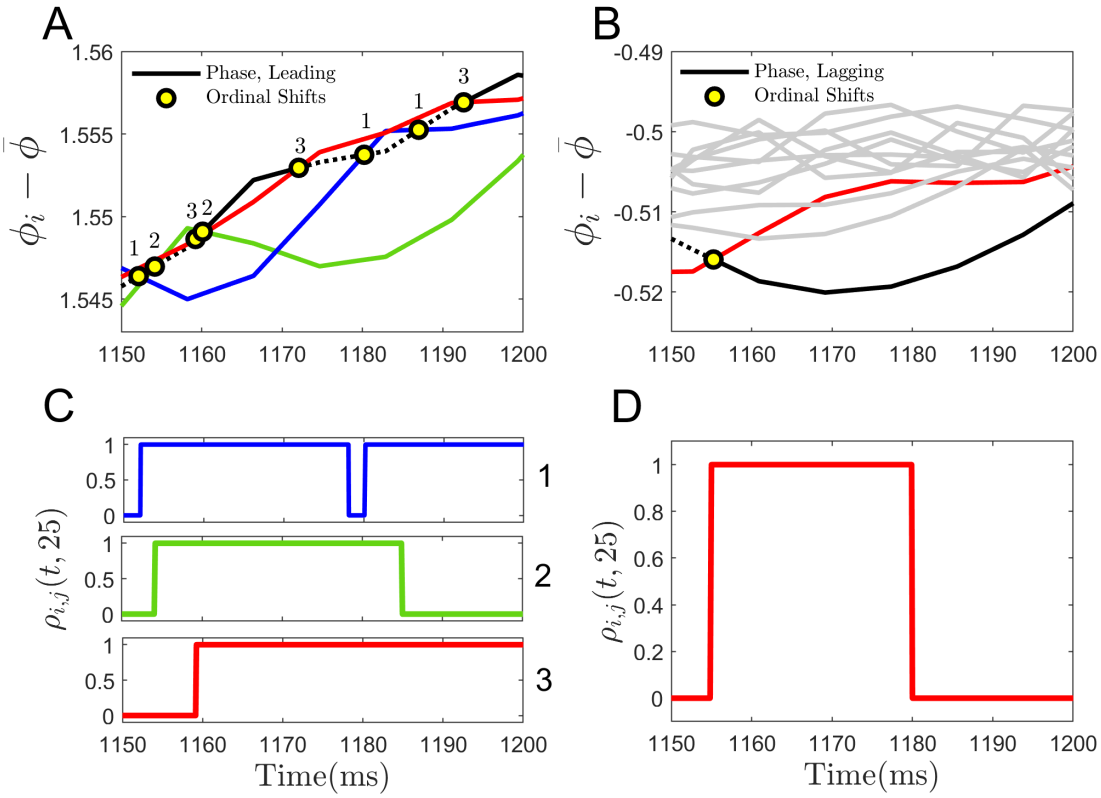

Figure 3.5: Panel A and B show the phases of an example population of $N = 25$ neurons plotted with respect to the rotating reference frame. Panels A and B show the leading and the lagging edge, respectively. The black line in panel A (resp., B) highlights a trace associated with a single neuron that is leading (resp., lagging) at some point in the simulation; this black line is solid at the moments when this neuron is the leading (resp., lagging) neuron and dashed otherwise. For this specific neuron, all ordinal shifts are highlighted with yellow circles. In panel A, the yellow circles are numbered 1, 2, or 3 with the number corresponding to the identically numbered subplot in panel C. In panels A and B, the traces associated with neurons that do not change order with the black traces are shown in gray while those that do change order are colored. Panel C (resp., D) shows the value of $\rho_{i,j}(t, 25)$ associated with the change in ordering between the black trace and the trace of corresponding color from panel A (resp., B).

switches with the black traces in panels A and B are marked with yellow circles, and in panel A these switches are numbered 1, 2, or 3, with the number corresponding to same numbered subplot in panel C. Panel C (resp., D) shows the value of $\rho_{i,j}(t, 25)$ associated with the change in ordering between the black trace and the trace of corresponding color from panel A (resp., B). In panel C, each $\rho_{i,j}$ is shown on its own subplot since more than one neuron switched with the neuron of interest. The first switch in panels A and B between the neuron with the black trace and the corresponding colored neuron marks the instant that $\rho_{i,j} = 1$ for that pair. Prior to this switch, $\rho_{i,j} = 0$. $\rho_{i,j}$ remains at 1 unless τ time passes without a switch. Note that per the definition from (3.14), $\rho_{i,j} = 1$ if neurons i and j switch one or more times on the interval $[t - \tau, t]$; multiple switches on the same interval still yield $\rho_{i,j} = 1$.

Considering the definition of t_s from Equation (3.13) one can show $\rho_{i,j}(t, t_s) = 0$ implies

$$\begin{cases} g_{i\to j}(t) > 1 - M, & \text{if } \theta_i \text{ leads } \theta_j, \text{ and } \theta_{\mathrm{i}} - \theta_{\mathrm{j}} < \mathrm{t_c/T}, \\ g_{i\to j}(t) < g_{min} + M, & \text{if } \theta_j \text{ leads } \theta_i, \text{ and } \theta_{\mathrm{j}} - \theta_{\mathrm{i}} < \mathrm{t_c/T} \end{cases} \tag{3.16}$$

Above, recall that $M > 0$ is an $O(\epsilon)$ term and the values θ_i and θ_j are continuous functions of time and do not refer to the phase at a given spike time.

3.3.2 An Upper Bound on the Critical Coupling Strength

To proceed, suppose that at some initial time, t_0, the phases of the neurons from (3.3) are contained within an arclength $\nu(t) \in [0, \pi]$ for which

$$\max_{i,j} |\theta_i(t_0) - \theta_j(t_0)| \leq \nu. \tag{3.17}$$

Phase cohesion is maintained so long as (3.17) holds for all forward time. As a reminder, for synaptic plasticity to modulate the synaptic weights in the model, the neurons need to have a causal or noncausal relationship (firing within t_c of one another). If the arclength, ν, is small enough, then there will always be a causal or anticausal relationship. Therefore, this derivation will focus on determining what coupling strength, K_{crit}, is required to ensure $\max_{i,j} |\theta_i(t) - \theta_j(t)| \leq \nu$ for all $t > t_0$.

To begin, consider any two oscillators with phases θ_m and θ_n for which $\theta_m - \theta_n = \nu$. Here, θ_m is at the leading edge of ν and θ_n is at the trailing edge. The goal here is to provide general

conditions that ensure that $\dot{\theta}_m - \dot{\theta}_n \leq 0$, thereby ensuring that the phase differences do not increase beyond ν. Towards this goal, suppose that

$$\eta_k(t, t_s) \leq \beta, \tag{3.18}$$

for $k = \{m, n\}$, that is, the current leading and lagging neuron experience at most β order shifts in the time interval $[t - t_s, t]$. Note that (3.18) is an assumption that limits the amount of order switching between neurons on a given time interval.

Combining Equations (3.18) and (3.16) with Equation (3.12), one can write

$$\begin{aligned}
\dot{\psi}_{m,n} \leq \omega_m - \omega_n &- \epsilon \frac{\hat{K}}{N-1} \sum_{k|\rho_{k,m}(t,t_s)=0} \Big[g_{min} Z_m(\theta_m) s_k(\theta_k)(V_m(\theta_m) - E_{syn}) \Big] \\
&- \epsilon \frac{\beta \hat{K}}{N-1} \min_{\theta, \upsilon} \Big[\upsilon Z_m(\theta) s_k(\theta)(V_m(\theta) - E_{syn}) \Big] \\
&+ \epsilon \frac{\hat{K}}{N-1} \sum_{k|\rho_{k,n}(t,t_s)=0} \Big[Z_n(\theta_n) s_k(\theta_k)(V_n(\theta_n) - E_{syn}) \Big] \\
&+ \epsilon \frac{\beta \hat{K}}{N-1} \max_{\theta, \upsilon} \Big[\upsilon Z_n(\theta) s_k(\theta)(V_n(\theta) - E_{syn}) \Big] + O(\epsilon^2),
\end{aligned} \tag{3.19}$$

where $\upsilon \in [g_{min}, 1]$. The above inequality is obtained by considering the maximum value and minimum value for the influence of synaptic coupling from neurons that have switched order in the time interval considered, Equation (3.19) can be rewritten as

$$\begin{aligned}
\dot{\psi}_{m,n} \leq \dot{\mu}_{m,n} = \omega_m - \omega_n &- \epsilon \frac{\hat{K}}{N-1} \sum_{k|\rho_{k,m}(t,t_s)=0} \Big[g_{min} Z_m(\theta_m) s_k(\theta_k)(V_m(\theta_m) - E_{syn}) \Big] \\
&+ \epsilon \frac{\hat{K}}{N-1} \sum_{k|\rho_{k,n}(t,t_s)=0} \Big[Z_n(\theta_n) s_k(\theta_k)(V_n(\theta_n) - E_{syn}) \Big] + \epsilon \frac{\beta \hat{K}}{N-1} (C_1 + C_2) + O(\epsilon^2),
\end{aligned} \tag{3.20}$$

where C_1 and C_2 are appropriately defined constants and $\mu_{m,n}$ provides an upper bound for $\psi_{m,n}$. Recalling that $\phi_i = \theta_i - \omega_0 t$, one can rewrite Equation (3.20) as

$$\dot{\mu}_{m,n} = \omega_m - \omega_n - \epsilon\frac{\hat{K}}{N-1}\sum_{k|\rho_{k,m}(t,t_s)=0}\Big[g_{min}Z_m(\phi_m+\omega_0 t)s_k(\phi_k+\omega_0 t)(V_m(\phi_m+\omega_0 t)-E_{syn})\Big]$$
$$+\epsilon\frac{\hat{K}}{N-1}\sum_{k|\rho_{k,n}(t,t_s)=0}\Big[Z_n(\phi_n+\omega_0 t)s_k(\phi_k+\omega_0 t)(V_n(\phi_n+\omega_0 t)-E_{syn})\Big]$$
$$+\epsilon\frac{\beta\hat{K}}{N-1}(C_1+C_2)+O(\epsilon^2). \tag{3.21}$$

Equation (3.21) is T_0-periodic, where $T_0 = 2\pi/\omega_0$ so that provided $\omega_m - \omega_n = O(\epsilon)$, its dynamics can be well-approximated using averaging theory [105]

$$\dot{\mu}_{m,n} = \frac{1}{T_0}\int_0^{T_0}\Bigg(\omega_m - \omega_n + \epsilon\frac{\beta\hat{K}}{N-1}(C_1+C_2)$$
$$-\epsilon\frac{\hat{K}}{N-1}\sum_{k|\rho_{k,m}(t,t_s)=0}\Big[g_{min}Z_m(\phi_m+\omega_0 t)s_k(\phi_k+\omega_0 t)(V_m(\phi_m+\omega_0 t)-E_{syn})\Big]$$
$$+\epsilon\frac{\hat{K}}{N-1}\sum_{k|\rho_{k,n}(t,t_s)=0}\Big[Z_n(\phi_n+\omega_0 t)s_k(\phi_k+\omega_0 t)(V_n(\phi_n+\omega_0 t)-E_{syn})\Big]+O(\epsilon^2)\Bigg)dt. \tag{3.22}$$

Noting that the integral in Equation (3.22) is evaluated over a single period, it can be rewritten in terms of the phase differences, i.e.,

$$\dot{\mu}_{m,n} = \omega_m - \omega_n + \epsilon\frac{\beta\hat{K}}{N-1}(C_1+C_2)$$
$$-\sum_{k|\rho_{k,m}(t,t_s)=0}\Big[\frac{\epsilon\hat{K}}{N-1}g_{min}\Gamma_{m,k}(\phi_m-\phi_k)\Big]+\sum_{k|\rho_{k,n}(t,t_s)=0}\Big[\frac{\epsilon\hat{K}}{N-1}\Gamma_{n,k}(\phi_n-\phi_k)\Big], \tag{3.23}$$

where

$$\Gamma_{i,j}(\phi) = \frac{1}{T_0}\int_0^{T_0} Z_i(\omega_0 t)s_j(\phi+\omega_0 t)(V_i(\omega_0 t)-E_{syn})dt. \tag{3.24}$$

Allowing for heterogeneity in the population of neurons, Equation (3.23) can be upper bounded by

$$\dot{\mu}_{m,n} \leq \omega_m - \omega_n + \epsilon\frac{\beta\hat{K}}{N-1}(C_1+C_2) - \sum_{k|\rho_{k,m}(t,t_s)=0}\frac{\epsilon\hat{K}}{N-1}g_{min}\Gamma_{min}(\phi_m-\phi_k)$$
$$+\sum_{k|\rho_{k,n}(t,t_s)=0}\frac{\epsilon\hat{K}}{N-1}\Gamma_{max}(\phi_n-\phi_k), \tag{3.25}$$

where

$$\Gamma_{max}(\phi) = \max_{\substack{i=1,\dots,N \\ j=1,\dots,N}} \Gamma_{i,j}(\phi),$$
$$\Gamma_{min}(\phi) = \min_{\substack{i=1,\dots,N \\ j=1,\dots,N}} \Gamma_{i,j}(\phi). \tag{3.26}$$

Noting that $\phi_m - \phi_k \in [0, \nu]$ and $\phi_n - \phi_k \in [-\nu, 0]$ for any k, the right hand side of Equation (3.25) can be bounded by

$$\dot{\mu}_{m,n} \leq \omega_m - \omega_n + \epsilon\frac{\beta\hat{K}}{N-1}(C_1 + C_2) - \frac{\epsilon\hat{K}g_{min}(N-\beta-1)}{N-1}\min_{\phi\in(0,\nu)}\left(\Gamma_{min}(\phi)\right)$$
$$+ \frac{\epsilon\hat{K}(N-\beta-1)}{N-1}\max_{\phi\in(-\nu,0)}\left(\Gamma_{max}(\phi)\right). \tag{3.27}$$

Above, $\phi = 0$ is not included in the maximization and minimization because otherwise $\rho_{m,k}$ and $\rho_{n,k}$ would equal 1. Considering Equation (3.27), $\dot{\mu}_{m,n} \leq 0$, and hence cannot increase, provided

$$\hat{K} \geq \frac{(N-1)(\Delta\omega_{max})}{\epsilon\left[(N-\beta-1)\left(g_{min}\min_{\phi\in(0,\nu)}(\Gamma_{min}(\phi)) - \max_{\phi\in(-\nu,0)}(\Gamma_{max}(\phi))\right) - \beta(C_1+C_2)\right]}, \tag{3.28}$$

where $\Delta\omega_{max} = \max_{i,j}(\omega_i - \omega_j)$ for any possible value of i and j. Recalling that $\psi_{m,n} \leq \mu_{m,n}$, if Equation (3.28) is satisfied, the phase difference between neurons m and n cannot increase. By definition, this provides an upper bound on the coupling strength to retain phase cohesion in the overall network of neurons. Recalling that $\hat{K} = \frac{K}{\epsilon C}$,

$$K_{crit}(\beta,\nu) \leq \frac{C(N-1)(\Delta\omega_{max})}{\left[(N-\beta-1)\left(g_{min}\min_{\phi\in(0,\nu)}(\Gamma_{min}(\phi)) - \max_{\phi\in(-\nu,0)}(\Gamma_{max}(\phi))\right) - \beta(C_1+C_2)\right]} \tag{3.29}$$

is an upper bound on the critical coupling strength, K, required to maintain phase cohesion. The actual critical coupling strength is guaranteed to be less than this estimated value. Notice that the bound (3.29) is a function of β. In the limit that the effect from order switching is negligible, $\beta = 0$ will provide an accurate estimate for the upper bound. The individual terms that comprise (3.29) give insight about when phase cohesion is possible. For instance, the right hand side of (3.29) grows with the dispersion in frequencies $\Delta\omega_{max}$ indicating that larger coupling strengths will be required when the difference in frequencies is larger. Noting that C_1 and C_2 will generally be positive and

also recalling that $\hat{K}$ must be positive, $g_{min}\min_{\phi\in(0,\nu)}(\Gamma_{min}(\phi)) - \max_{\phi\in(-\nu,0)}(\Gamma_{max}(\phi)) > 0$ must be true for any upper bound on K to exist. Assuming $g_{min} \approx 0$, this would require $\Gamma_{max}(\phi) < 0$. As β increases, i.e., as the reordering of the neurons becomes faster relative to the time scales associated with the plastic synaptic conductances, the contribution from constants C_1 and C_2 increases, thereby increasing the upper bound on $\hat{K}$.

3.3.3 Comparison With Upper Bounds Using Static Synaptic Strengths

The result (3.29) provides an upper bound for the critical coupling strength where the synaptic weights are governed by the Hebbian STDP rule from Equation (3.6). Previous work [142] considered upper bounds for coupled inhibitory neural populations when the coupling strength is static. Excitatory neurons were not considered in [142] as phase cohesion is not possible with static synaptic coupling. Using a simplified form of the synaptic conductance

$$I_{syn}^{j\to i} = Ks_j(t)(V_i - E_{syn}), \tag{3.30}$$

where $K > 0$ is a constant synaptic conductance and the remaining terms are defined identically to those from Equation (3.2) the analysis from [142] determined the following upper bound for the critical coupling strength:

$$K_{crit}(\nu) \leq \frac{C\Delta\omega_{max}}{\min\limits_{\phi\in[0,\gamma]}\left(\Gamma_{min}(\phi) - \Gamma_{max}(\phi-\nu)\right)}. \tag{3.31}$$

In Equation (3.31), the contribution from $\Gamma_{min}(\phi)$ is weighted equally to the contribution from $\Gamma_{max}(\phi-\nu)$. As a consequence, particularly when the effect of heterogeneity is negligible, the slope of $\Gamma_{min}(\phi)$ and $\Gamma_{max}(\phi)$ is important in determining the upper bound on $\hat{K}$. Equation (3.31) provided a viable solution in [142] for populations of inhibitory neurons but yields an impossible solution for populations of excitatory neurons as the right hand side is negative. This is consistent with the results shown in Figures 3.1 and 3.2 when the coupling strength is static. As a reminder, Γ_{max} and Γ_{min} are defined the same way that they were defined in Equation (3.26), and so the solution presented here is dependent on our specific model parameters.

Compared to the upper bound with plasticity (3.29), and considering that g_{min} is generally very close to zero, only $\Gamma_{max}(\phi)$ contributes to determining the upper bound on the critical coupling strength, which again would require $\Gamma_{max}(\phi) < 0$. This property does not hold for heterogeneous populations of inhibitory neurons. It does hold, however, for heterogeneous populations of excitatory neurons. Additionally, the ordering of the neurons within the network has a significant influence on the upper bound from (3.29) but has no bearing on the estimate from (3.31).

Figure 3.6 provides a visual comparison of the upper bound on K_{crit} calculated using equations (3.31) and (3.29), that is with and without the inclusion of synaptic plasticity, for a population

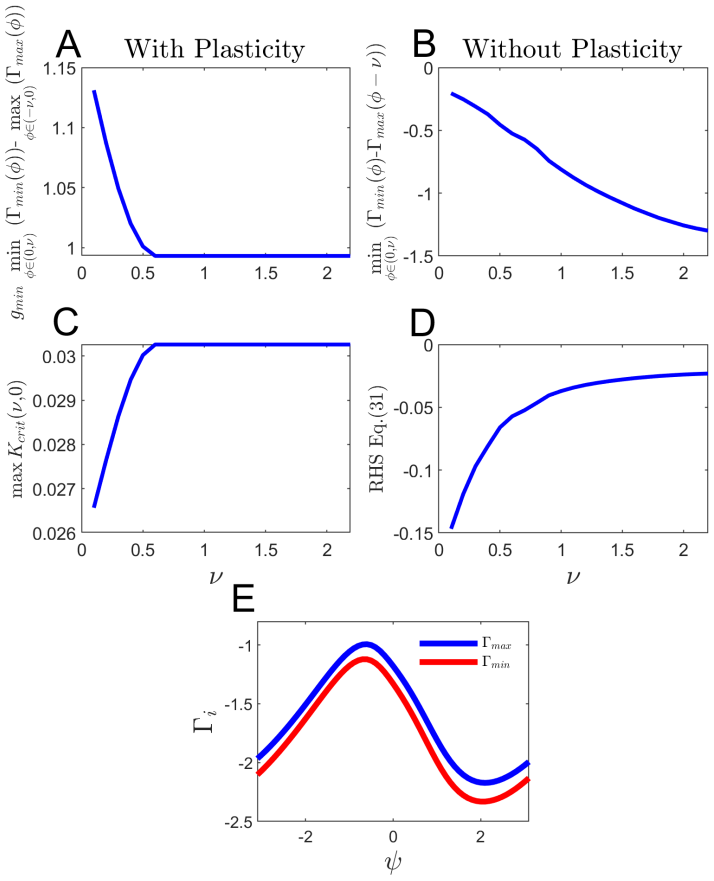

Figure 3.6: Panels A and B give a visual representation of the denominator of (3.29) taking $\beta = 0$ and (3.31), respectively. Panel C provides the corresponding max K_{crit} for populations of excitatory neurons with plastic synaptic coupling calculated in (3.29). Panel D gives the right hand side of Equation (3.31); because this value is negative, no positive value of K will result in a phase cohesive population when STDP is not considered. Panel E provides plots of Γ_{min} and Γ_{max} for reference.

of excitatory neurons. Panels A and B show the denominator terms from Equations (3.29) and (3.31), respectively, while panels C and D show the corresponding values of $\max K_{crit}$. Panel E shows the coupling functions, Γ_{max} and Γ_{min}, used in these calculations. Here $\beta = 0$ is assumed when considering the bound for the population with STDP. We emphasize that without synaptic plasticity, the right hand side of (3.31) is negative, indicating that no positive value of K can be chosen in order to yield phase cohesion. The results from Figure 3.6 are consistent with those from Figure 3.2, where the population remains phase cohesive if synaptic plasticity is considered but loses phase cohesion when there is no synaptic plasticity. Note that although we consider $\beta = 0$ here, this is to get an initial sense of how well this bound works for small values of β. Nonzero values of β will be considered in Section 4.

3.3.4 The Critical Coupling Strength for Inhibitory Neurons

This paper has focused on the implications of STDP on the retention of phase cohesion in a population of heterogeneous excitatory neurons. However, our results would be incomplete if we did not include some of our studies on populations of inhibitory neurons. Reference [142] found the critical coupling strength required for phase cohesion in populations of heterogeneous inhibitory neurons with static synaptic coupling. To demonstrate why inhibitory populations could not be included in this paper, we present Figure 3.7. Here we have considered a population of neurons with $I_{stim} \in [4.92, 5.08]$. Note that in panels B and D, the denominator shown in Panel B is positive and the critical coupling strength is therefore positive for $\nu \in [0.2, 0.6]$, indicating that within this region, phase cohesion among these heterogeneous oscillators with inhibitory synaptic coupling is possible. Adding synaptic plasticity, however, removes the possibility of phase cohesion, as can be verified in panels A and C, which are consistently negative for all values of ν. Again panel E shows the coupling functions, Γ_{max} and Γ_{min}, used in these calculations.

3.4 Numerical Results

For validation of the bound obtained in Section 3.3.2, we consider a population of N coupled excitatory neurons from Equation (3.3). For these simulations $I_{stim,i} \in [4.84, 5.16]$ with specific values taken from the distributions described below. To numerically determine the actual critical coupling strength, we choose a synaptic conductance, K, (i.e., the coupling strength) larger than

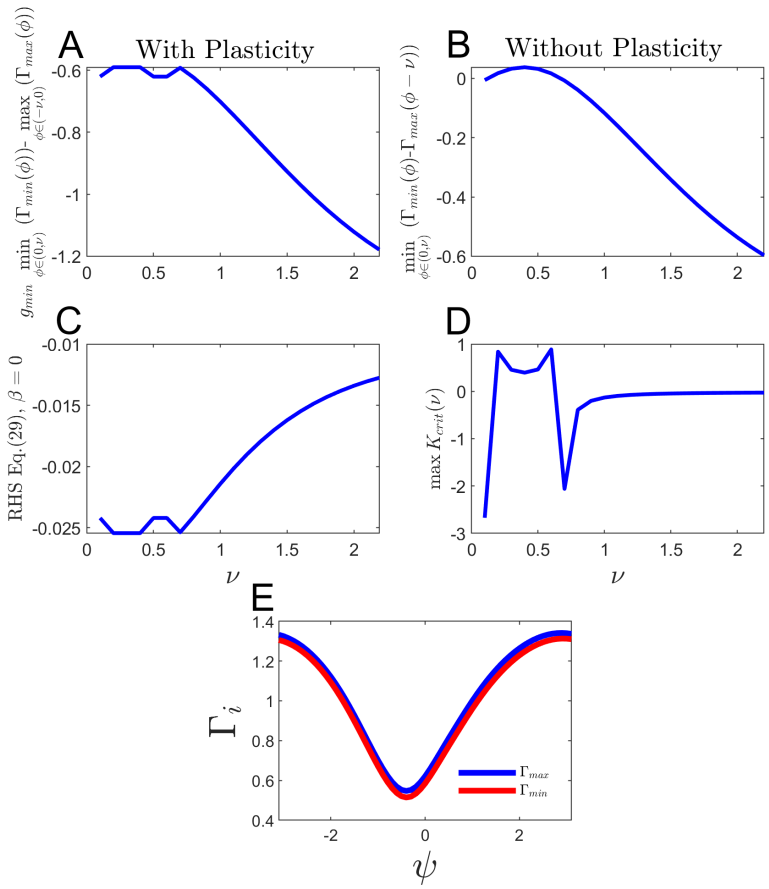

Figure 3.7: Panels A and B give a visual representation of the denominator of (3.29) taking $\beta = 0$ and (3.31), respectively, for populations of inhibitory neurons with $I_{stim} \in [4.92, 5.08]$. Panel C provides the corresponding RHS of Eq. (3.29), given $\beta = 0$ for these same populations of inhibitory neurons with plastic synaptic coupling. Since this value is negative, no positive value of K will result in a phase cohesive population when the synaptic coupling is subject to this specific form of Hebbian STDP. Panel D gives the upper bound on the critical coupling strength, $\max K_{crit}$, for populations of inhibitory neurons with static synaptic coupling, which is seen to be positive in the region $\nu \in [0.2, 0.6]$. Panel E provides plots of Γ_{min} and Γ_{max} for reference.

the critical value and slowly decrease until phase cohesion is lost. Here, we consider a population to be phase cohesive if the phases of all neurons remain within an arclength of size $\nu = 2.3$ radians.

Results are shown in Figure 3.8. In each panel of Figure 3.8, the upper bound on the critical coupling strength is computed according to Equation (3.29), taking $\beta = 0$ and using the maximum value over all values of ν. This bound is shown with a dashed line for reference. In panel A, we consider populations of N=5, 10, 15, 20, 25, and 30 excitatory neurons with baseline currents that

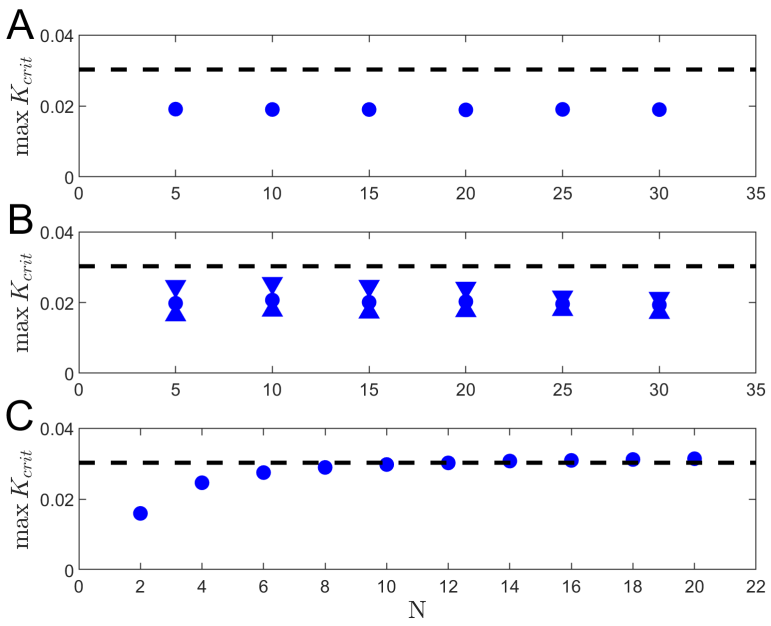

Figure 3.8: In each panel, the dashed black line represents the upper bound on the critical coupling strength computed according to Equation (3.29), taking $\beta = 0$ (i.e., assuming no switching between neurons on the boundary) and taking the maximum over all values of ν. In panel A, the true critical coupling strength for populations of different sizes with baseline currents spread evenly between the maximum and minimum values are shown with dots. Panel B is similar, except with the baseline currents drawn from a uniform distribution. Here the triangles and circles represent the minimum, average, and maximum value of the numerically computed critical coupling strength obtained from 30 total trials for each population size. In panel C, half of the neurons have the maximum value of baseline current and the other half have the minimum baseline current.

are evenly spread between the upper and lower bounds. For each trial, the actual critical coupling strength is approximately 35 percent below the predicted critical coupling strength value. In panel B, we consider populations of neurons with two neurons having the minimum and maximum values for the baseline current and we draw the remaining baseline currents from a uniform distribution. We again consider population sizes of N=5, 10, 15, 20, 25, and 30 excitatory neurons. For each population size considered, we numerically compute the critical coupling strength for 30 trials. Due to the randomness in each population, there is some spread in the critical coupling strengths obtained. Panel B shows the maximum, minimum, and mean of each group of 30 trials. We also consider even numbered populations of excitatory neurons where $N/2$ neurons have the smallest possible baseline current and the remaining $N/2$ neurons have the largest possible baseline current.

The results for these trials are shown in panel C of Figure 3.8. Particularly for these simulations, it is expected that there will be more order switching between the neurons on the boundary because the unperturbed natural frequencies are clustered at the maximum and minimum values. For this reason, these simulations ultimately require a larger coupling strength to retain phase cohesion with some trials having a critical coupling strength above the value predicted from Equation (3.29) for $\beta = 0$.

Figure 3.9 is included to more carefully investigate the influence of order switching among the neurons in a population. Here we consider simulations with baseline currents taken identically to those considered in Figure 3.8 and plot the corresponding η value over time for one of these

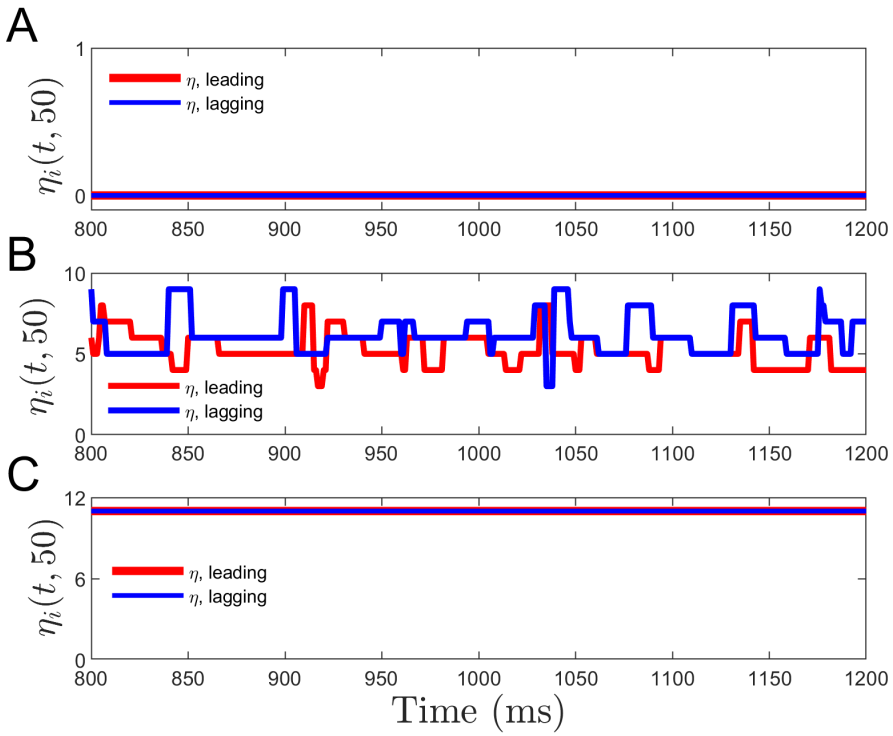

Figure 3.9: In each panel, the value $\eta_i(t, 50)$ is calculated over time for a single simulation of $N = 25$ neurons in panels A and B and $N = 24$ neurons in panel C. For these trials the coupling strength is near the actual critical coupling strength so that the neurons are just within the arclength, ν, and not forced together through strong coupling. In panel A, the natural frequencies are evenly distributed as is done in panel A of Figure 3.8. In panel B, the natural frequencies are taken from a uniform distribution as was done in the trials from panel B of Figure 3.8. In panel C, half of the neurons have natural frequencies of ω_{max} and half of the neurons have natural frequencies of ω_{min}, as was done in the trials from panel C of Figure 3.8.

simulations. Note that in each simulation, K is taken to be close to the critical value for phase cohesion. Panel A shows η calculated according to (3.15) for the leading and lagging neurons from a population of $N = 25$ neurons with evenly distributed natural frequencies, as was done in panel A of Figure 3.8. In panel B of Figure 3.9, we show the η value for a single simulation of $N = 25$ neurons where the baseline currents are drawn from a uniform distribution, as was done in panel B of Figure 3.8. In panel C of Figure 3.9, we finally present the η value for a simulation of N=24 neurons with half of the natural frequencies clustered at the lower bound and half at the upper bound as was done in panel C of Figure 3.8. For these trials, to ensure that our leading and lagging edge neurons were contained within and near the limits of the arclength ν, we set $K = 0.025$ in panels A and B and $K = 0.035$ in panel C. The fact that the true critical coupling strength in panel C of Figure 3.8 exceeds the predicted critical coupling strength is consistent with the fact that in panel C of Figure 3.9, order switching is nonnegligible. Note that η is shown in these plots for the *current* leading or lagging neuron at time, t. Large jumps in η, such as those in panel B, often occur when a new neuron takes over as the leading or lagging neuron in a population. As such, when a switch occurs at the leading or lagging edge, the value of η can increase/decrease by several natural numbers in a single time step.

3.5 Discussion and Conclusion

The presence or absence of spike timing dependent plasticity (STDP) can qualitatively alter the collective behavior of a synaptically coupled population of neurons. In this work, we derive an upper bound for the critical coupling strength required for maintaining phase cohesion in a population of conductance based, synaptically coupled neurons subject to Hebbian STDP. This work can be viewed as an extension of results from [142] (which assumed static coupling strengths between oscillators with inhibitory connections). In addition to providing a reasonably tight upper bound on the critical coupling strength required to retain phase cohesion in populations of excitatory neurons, the results also explain the qualitative differences in the aggregate behavior in Figures 3.1 and 3.2, where the populations are simulated with and without synaptic plasticity. When the influence of coupling felt by the leading neurons is diminished over time (as is the case here) the stability of the phase cohesive state can change depending on whether the coupling is excitatory or inhibitory.

In contrast to results that do not consider STDP, the critical coupling strength depends on the ordering of neurons. In particular, changes to the ordering of the neurons on the edge of the arclength will degrade the synchronizing influence of synaptic coupling, ultimately requiring a stronger coupling strength to retain phase cohesion. This effect is reflected in the results from Figure 3.8 and Figure 3.9. Individual neurons from larger populations with evenly spaced natural frequencies switch spike order less often and consequently require smaller coupling strengths to retain phase cohesion. Individual neurons from larger populations with natural frequencies clustered at the maximum and minimum values switch spike order more and hence require larger coupling strengths to retain phase cohesion. As emphasized in Figures 3.8 and 3.9, even when the overall population remains phase cohesive, there are still a small number of order shifts between neurons in the overall population.

There are a number of limitations and possible extensions of the present work. Here, we are only concerned with the stability of the phase cohesive state but are not able to make any deductions about its basin of attraction or make inferences about spontaneous synchronization that may emerge in a coupled population of oscillators. We are also unable to make any direct inferences about frequency synchronization, although this phenomenon was not observed in any of the examples considered. Additionally, we do not directly consider the influence of noise in the population which would certainly be a factor in a more realistic population of neural oscillators. Furthermore, the phase-based reduction techniques used here are only valid in the weakly perturbed limit and it may be necessary to incorporate alternative phase-based reduction strategies that can accommodate larger magnitude inputs in more realistic models. We elected to use soft bound Hebbian STDP in our model, which does not allow for unrestricted growth or decay of a given synaptic connection, bounding the synaptic strength so that $g_{i\to j} \in [g_{min}, 1]$ and $|\Delta g_{i\to j}|$ decreases as the synaptic strength approaches a boundary. However, there exist qualitative differences when hard bounds are implemented instead, where the update to the synaptic connection is linearly additive and no longer a function of the current synaptic weight. Some of these qualitative differences, such as those mentioned in [118] and [32], could affect these results. It would be of interest to conduct further analysis on how hard bounds would alter the findings presented here. Finally, the analysis considered in this work is only valid for tonically firing neurons and it would be of interest to investigate possible extensions for bursting neurons or for neurons without a well-defined firing rate.

Chapter 4

Direct Method Phase-Based Model Identification for Coupled Oscillators

4.1 Introduction

Functional connections of the brain have been studied for decades [48], [5]. Many of these studies are motivated by the potential to understand the efficacy of treatments for certain neurological or psychiatric conditions where the only true observables are the manifestation or disappearance of related symptoms [149]. For example, deep brain stimulation (DBS) has proven to be an effective treatment for a variety of neurological and psychiatric conditions, such as Parkinsonian tremors [8], dystonia [119], epilepsy [104], and treatment-resistant depression [70]. However, while the efficacy of the treatment is known, the functional reason for the efficacy is frequently not fully understood. Findings indicate that brain rhythms play an important role in cognitive function, and abnormal brain rhythms are related to the onset of certain neurological disorders [73]. Excessive synchronization of neurons, for instance, is observed in patients with Parkinson's disease and the disruption of this synchronization through DBS alleviates the associated tremors [73], [41], [54], [58], [115]. Motivated by the potential applications of data-driven reduced order modeling in computational neuroscience, we present here a data-driven method that extends the direct method to produce a phase-based reduced order model that accounts for complex coupling structures between oscillators.

Phase-based reduction strategies are frequently used to model oscillatory dynamical systems of the general form

$$\dot{x} = F(x, u), \tag{4.1}$$

where $x \in \mathbb{R}^n$ defines the state and u is an applied input restricted to be $O(\epsilon)$ in magnitude, where $0 < \epsilon \ll 1$ [11], [30], [43], [51], [77], [148], [85], [75]. Provided a T-periodic limit cycle x^γ exists, the n-dimensional system described in Equation (4.1) can be represented in a reduced order framework using isochrons to define a reduced order coordinate system within the basin of attraction of the limit cycle [22], [6], [147]. For any two initial conditions, $a(0)$ and $b(0)$, in the basin of attraction, $\lim_{t\to\infty}||a(t) - b(t)|| = 0$ if they are on the same isochron [145], [147], [30].

Simple phase reduction is often sufficient when the input $u(t)$ is small enough in magnitude that deviations from x^γ are small. Phase-amplitude reduction is an extension of phase reduction that utilizes Floquet theory to derive the dynamics of additional amplitude coordinates that account for perturbations transverse to the periodic orbit [145]. The resulting phase-amplitude reduced order model can be used to overcome some of the shortcomings of standard phase-based reduction strategies [134], [116].

The necessary terms of the phase-amplitude reduction are computed straightforwardly when the underlying dynamical equations are known. When model equations are unavailable, they can be inferred from data using the direct method [147], [26], [78]. To implement the direct method, small pulse inputs are applied to estimate the phase sensitivity. It is essential that other unmodeled inputs such as coupling and noise do not significantly alter the phase. When considering a coupled system of oscillators, it is not possible to apply the direct method to infer the phase-amplitude reduced equation for the individual oscillators.

Previous research on data-driven model identification strategies for nonlinear dynamical systems utilize a variety of other techniques. For instance, dynamic mode decomposition (DMD) yields linear modes that represent snapshots of time-series data that can be analyzed with respect to associated eigenvalues and eigenvectors [106], [52], [102], [93] [35]. Since DMD yields a linear operator, however, it is often difficult to apply to systems with stable oscillations. Common machine learning approaches to model identification include the sparse identification of nonlinear dynamics (SINDy) algorithm, which implements sparse regression to find candidate functions that best reflect a given system's temporal dynamics [13], [65]. However, since the SINDy algorithm considers best candidate functions, these functions may not always reflect the true dynamics or structure of a

system and its coupling. Additionally, with machine learning, overfitting is a concern. Deep learning and neural networks can also be applied to infer the dynamics of nonlinear dynamical systems from data [83], [125],[61], [95]. However, similar to traditional machine learning, overfitting can again be an issue, and the black box nature of deep learning models imply that any derived coupling structure within the system may not be accurate or fully understood. Data-driven approaches to phase-based model reduction have also been considered in previous works. In [133], proper orthogonal decomposition was applied to observable data to infer the parameters for a phase-amplitude reduced order model. In [139], the authors derive a phase-amplitude model using the aforementioned direct method by strategically applying external inputs to a system and measuring the system's sensitivity to perturbations at different states along its limit cycle. In [3], the authors implement deep learning and artificial neural networks to determine relevant terms for a phase-amplitude reduced order model.

In this work, we extend the direct method to explicitly consider a population of coupled limit cycle oscillators. Using observables from these systems, we propose a strategy to infer relevant parameters for their corresponding phase-based reduced order models. This work is primarily motivated by the impact of neural brain rhythms on cognitive function and potential applications of the analysis of these rhythms in both experimental and computational environments.

The remainder of this paper is organized as follows. In Section 4.2, we describe the phase-amplitude reduced order model, its limitations, and its underlying assumptions and derive an analytical model that will form the basis of the data-driven algorithm. In Section 4.3, we provide a detailed algorithm for inferring the necessary terms of the reduced order model from data. Section 4.4 provides results for a simple coupled two oscillator system. Section 4.5 gives an overview of the study of population-level oscillations for neural models. Sections 4.6 and 4.7 give results for the proposed model identification strategy applied to population-level oscillations of a two subnetwork (Section 4.6) and four subnetwork (Section 4.7) system of neural oscillators. Concluding remarks are provided in Section 4.8.

4.2 The Phase-Amplitude Reduced Order Model

4.2.1 Background

Consider a general nonlinear dynamical system of the form (4.1), where x is the state as determined by the system's internal dynamics and u is an external input. Provided a T-periodic limit cycle x^γ exists, the timing of the oscillations in (4.1) can be considered using phase reduction.

Transforming to phase coordinates, the dynamics are:

$$\begin{aligned}\dot{\theta} &= \frac{\partial \theta}{\partial x} \cdot \dot{x} \\ &= \frac{\partial \theta}{\partial x} \cdot F(x,u) \\ &= \frac{\partial \theta}{\partial x} \cdot \big(F(x,0) + \frac{\partial F}{\partial u} u + O(|u|^2)\big).\end{aligned} \tag{4.2}$$

Simplifying Equation (4.2) further and dropping higher order terms yields a standard phase reduced model:

$$\dot{\theta} = \omega + \epsilon Z(\theta) u(t), \tag{4.3}$$

where $\omega = 2\pi/T$ is the natural frequency of the limit cycle oscillator and $Z(\theta) = \frac{\partial \theta}{\partial x}^T \frac{\partial F}{\partial u}$ is the infinitesimal phase response curve evaluated along the limit cycle at phase θ.

The addition of amplitude coordinates in a reduced order model can account for perturbations from the limit cycle which decay slowly back towards the periodic orbit [145]. Amplitude coordinates can be included by considering level sets of the slowest decaying eigenmodes of the Koopman operator [53],[69]. The slowest decaying isostable coordinate is defined within the basin of attraction of a limit cycle according to

$$\psi(x) = \lim_{t \to \infty} (w^T (\nu(t_\Gamma^k, x) - x_0) \exp(-\kappa t_\Gamma^k)), \tag{4.4}$$

where $\nu(t_\Gamma^k, x)$ defines the flow of the dynamical system defined in Equation (4.1), x_0 is the location where the $\theta = 0$ isochron crosses the periodic orbit, t_Γ^k is the time of the k^{th} crossing of the $\theta = 0$ isochron, w is the left eigenvector of the monodromy matrix associated with the slowest decaying Floquet exponent, and κ is the slowest decaying Floquet exponent.

The dynamics of the isostable coordinate for a single oscillator are:

$$\begin{aligned}\dot{\psi} &= \frac{\partial \psi}{\partial x} \cdot \dot{x} \\ &= \frac{\partial \psi}{\partial x} \cdot F(x,u), \\ &= \frac{\partial \psi}{\partial x} \cdot \big(F(x,0) + \frac{\partial F}{\partial u} u + O(|u|^2)\big).\end{aligned} \tag{4.5}$$

Simplifying Equation (4.5) and dropping the higher order terms yields

$$\dot{\psi} = \kappa\psi + \epsilon I(\theta) u(t), \tag{4.6}$$

where κ is the slowest decaying Floquet exponent and $I(\theta) = \frac{\partial \psi}{\partial x}^T \frac{\partial F}{\partial u}$ is the isostable response curve evaluated along the limit cycle at each phase θ.

4.2.2 Phase and Amplitude Dynamics for a Coupled Population of Oscillators

Consider a population of N coupled limit cycle oscillators with dynamics that can be written in the form

$$\begin{aligned}\dot{\theta}_i &= \omega_i + \epsilon \sum_{k \neq i} Z_i(\theta_i) g_{k \to i}(\theta_i, \theta_k), \\ \dot{\psi}_i &= \kappa_i \psi_i + \epsilon \sum_{k \neq i} I_i(\theta_i) g_{k \to i}(\theta_i, \theta_k), \\ i &= 1, ..., N,\end{aligned} \tag{4.7}$$

where g sets the coupling. Here, $0 < \epsilon \ll 1$ so that the influence of coupling is small relative to the natural frequency of the oscillators. The oscillators are coupled in an all-to-all fashion with no self coupling. Defining $\phi_{i,j} = \theta_i - \theta_j$, Equation (4.7) can be rewritten as

$$\begin{aligned}\dot{\theta}_i &= \omega_i + \epsilon \sum_{k \neq i} Z_i(\theta_i) g_{k \to i}(\theta_i, \theta_i - \phi_{i,k}), \\ \dot{\psi}_i &= \kappa_i \psi_i + \epsilon \sum_{k \neq i} I_i(\theta_i) g_{k \to i}(\theta_i, \theta_i - \phi_{i,k}), \\ i &= 1, ..., N.\end{aligned} \tag{4.8}$$

The phase difference between any two oscillators, i and j, has associated dynamics defined to be $\dot{\phi}_{i,j} = \dot{\theta}_i - \dot{\theta}_j$ so that

$$\dot{\phi}_{i,j} = \omega_i - \omega_j + \epsilon \sum_{k \neq i} Z_i(\theta_i) g_{k \to i}(\theta_i, \theta_i - \phi_{i,k}) - \epsilon \sum_{k \neq j} Z_j(\theta_j) g_{k \to i}(\theta_j, \theta_j - \phi_{j,k}). \tag{4.9}$$

Provided $\omega_i - \omega_j = O(\epsilon)$, the right hand side of (4.9) is an order ϵ term and and we can apply formal dynamical averaging techniques [31], [105]. To begin, we will work in a rotating reference frame by defining a new phase variable,

$$\zeta_i = \theta_i - \omega_0 t, \tag{4.10}$$

where $\omega_0 = \frac{1}{N} \sum_{i=1}^{N} \omega_i$ is the average natural frequency of the population of N oscillators. Note that $\phi_{i,j} = \theta_i - \theta_j = \zeta_i - \zeta_j$. Rewriting Equation (4.8) in this rotating reference frame yields

$$\begin{aligned} \dot{\zeta}_i &= \omega_i - \omega_0 + \epsilon \sum_{k \neq i} Z_i(\zeta_i + \omega_0 t) g_{k \to i}(\zeta_i + \omega_0 t, \zeta_i - \phi_{i,k} + \omega_0 t) \\ \dot{\psi}_i &= \kappa_i \psi_i + \epsilon \sum_{k \neq i} I_i(\zeta_i + \omega_0 t) g_{k \to i}(\zeta_i + \omega_0 t, \zeta_i - \phi_{i,k} + \omega_0 t) \\ i &= 1, ..., N. \end{aligned} \tag{4.11}$$

Averaging the dynamics defined in Equation (4.11) over the period $T_0 = 2\pi/\omega_0$ and defining $\Delta\omega_i = \omega_i - \omega_0$ yields

$$\begin{aligned} \dot{\zeta}_i &= \frac{1}{T_0} \int_0^{T_0} \left[\Delta\omega_i + \epsilon \sum_{k \neq i} Z_i(\zeta_i + \omega_0 t) g_{k \to i}(\zeta_i + \omega_0 t, \zeta_i - \phi_{i,k} + \omega_0 t) \right] dt, \\ \dot{\psi}_i &= \frac{1}{T_0} \int_0^{T_0} \left[\kappa_i \psi_i + \epsilon \sum_{k \neq i} I_i(\zeta_i + \omega_0 t) g_{k \to i}(\zeta_i + \omega_0 t, \zeta_i - \phi_{i,k} + \omega_0 t) \right] dt, \\ i &= 1, ..., N, \end{aligned} \tag{4.12}$$

where solutions of (4.11) are well approximated by solutions of the averaged equation (4.12). Factoring out the constant terms from the integrands in Equation (4.12) and exchanging the

summation and integration order yields.

$$\dot{\zeta}_i = \Delta\omega_i + \epsilon \sum_{k \neq i} \frac{1}{T_0} \int_0^{T_0} \left[Z_i(\zeta_i + \omega_0 t) g_{k \to i}(\zeta_i + \omega_0 t, \zeta_i - \phi_{i,k} + \omega_0 t) \right] dt, \tag{4.13}$$

$$\dot{\psi}_i = \kappa_i \psi_i + \epsilon \sum_{k \neq i} \frac{1}{T_0} \int_0^{T_0} \left[I_i(\zeta_i + \omega_0 t) g_{k \to i}(\zeta_i + \omega_0 t, \zeta_i - \phi_{i,k} + \omega_0 t) \right] dt,$$

$$i = 1, ..., N.$$

Considering Equation (4.13), we define coupling functions between any two oscillators, i and k.

$$\Gamma_{\zeta, k \to i}(\phi_{i,k}) = \frac{\epsilon}{T_0} \int_0^{T_0} \left[Z_i(\zeta_i + \omega_0 t) g_{k \to i}(\zeta_i + \omega_0 t, \zeta_i - \phi_{i,k} + \omega_0 t) \right] dt, \tag{4.14}$$

$$\Gamma_{\psi, k \to i}(\phi_{i,k}) = \frac{\epsilon}{T_0} \int_0^{T_0} \left[I_i(\zeta_i + \omega_0 t) g_{k \to i}(\zeta_i + \omega_0 t, \zeta_i - \phi_{i,k} + \omega_0 t) \right] dt.$$

Note that because of the integration over an entire period, $\Gamma_{\zeta, k \to i}$ and $\Gamma_{\psi, k \to i}$ are functions of only $\phi_{i,k}$. Substituting (4.14) into (4.13) yields

$$\dot{\zeta}_i = \Delta\omega_i + \sum_{k \neq i} \Gamma_{\zeta, k \to i}(\phi_{i,k}), \tag{4.15}$$

$$\dot{\psi}_i = \kappa_i \psi_i + \sum_{k \neq i} \Gamma_{\psi, k \to i}(\phi_{i,k}),$$

$$i = 1, ..., N.$$

4.3 Data-Driven Model Identification for the Phase Dynamics of the Coupled Oscillator Model

4.3.1 Defining the Data-Driven Basis Function

The coupling functions, $\Gamma_{\zeta, k \to i}(\phi_{i,k})$ and $\Gamma_{\psi, k \to i}(\phi_{i,k})$, are periodic over the range $\phi = [0, 2\pi)$ and can therefore be approximated using the Fourier series expansion

$$\Gamma_{\zeta,k\to i}(\phi_{i,k}) \approx \frac{a_{0,k\to i}}{2} + \sum_{n=1}^{\infty} a_{n,k\to i}\sin(n\phi_{i,k}) + b_{n,k\to i}\cos(n\phi_{i,k}), \tag{4.16}$$
$$\Gamma_{\psi,k\to i}(\phi_{i,k}) \approx \frac{c_{0,k\to i}}{2} + \sum_{n=1}^{\infty} c_{n,k\to i}\sin(n\phi_{i,k}) + d_{n,k\to i}\cos(n\phi_{i,k}).$$

We write the dynamics in Equation (4.15) entirely using a Fourier series expansion by including two additional terms, $\Delta\omega_i$ and $\kappa_i\psi_i$. Substituting this Fourier series representation into (4.15) yields

$$\dot{\zeta}_i \approx \Delta\omega_i + \hat{a}_{0,i} + \sum_{k\neq i}\sum_{n=1}^{\infty} a_{n,k\to i}\sin(n\phi_{i,k}) + b_{n,k\to i}\cos(n\phi_{i,k}), \tag{4.17}$$
$$\dot{\psi}_i \approx \kappa_i\psi_i + \hat{c}_{0,i} + \sum_{k\neq i}\sum_{n=1}^{\infty} c_{n,k\to i}\sin(n\phi_{i,k}) + d_{n,k\to i}\cos(n\phi_{i,k}),$$
$$i = 1, ..., N,$$

where $\hat{a}_{0,i} = \frac{1}{2}\sum_{k\neq i} a_{0,k\to i}$ and $\hat{c}_{0,i} = \frac{1}{2}\sum_{k\neq i} c_{0,k\to i}$. Recall that using the weak coupling assumption, each $\phi_{i,k}$ changes slowly on the timescale of a single period and the averaged values can be used to approximate the unaveraged values of $\dot{\zeta}_i$ and $\dot{\psi}_i$ [31], [105]. Finally, we convert back to θ_i by substituting $\zeta_i = \theta_i + \omega_0 t$. We also determine some measurable value ν that varies each cycle between $\theta = 0$ isochron crossings to model the dynamics of each oscillator's isostable coordinate. This amplitude coordinate and the actual isostable coordinate have a linear relationship so that $\nu_i = p_i\psi_i$, where p_i is a constant. This value can, for instance, be the difference between the local maximum and the local minimum over a given cycle, as is represented in Figure 4.1 for a two oscillator model. Using the coordinate change $\nu_i = p_i\psi_i$, these substitutions yield the phase-based model that we we will obtain using a data-driven approach:

$$\dot{\theta}_i = \omega_i + \hat{a}_{0,i} + \sum_{k\neq i}\sum_{n=1}^{\infty} a_{n,k\to i}\sin(n\phi_{i,k}) + b_{n,k\to i}\cos(n\phi_{i,k}), \tag{4.18}$$
$$\dot{\nu}_i = \kappa_i\nu_i + \frac{\hat{c}_{0,i}}{p_i} + \sum_{k\neq i}\sum_{n=1}^{\infty} \frac{c_{n,k\to i}}{p_i}\sin(n\phi_{i,k}) + \frac{d_{n,k\to i}}{p_i}\cos(n\phi_{i,k})$$
$$i = 1, ..., N.$$

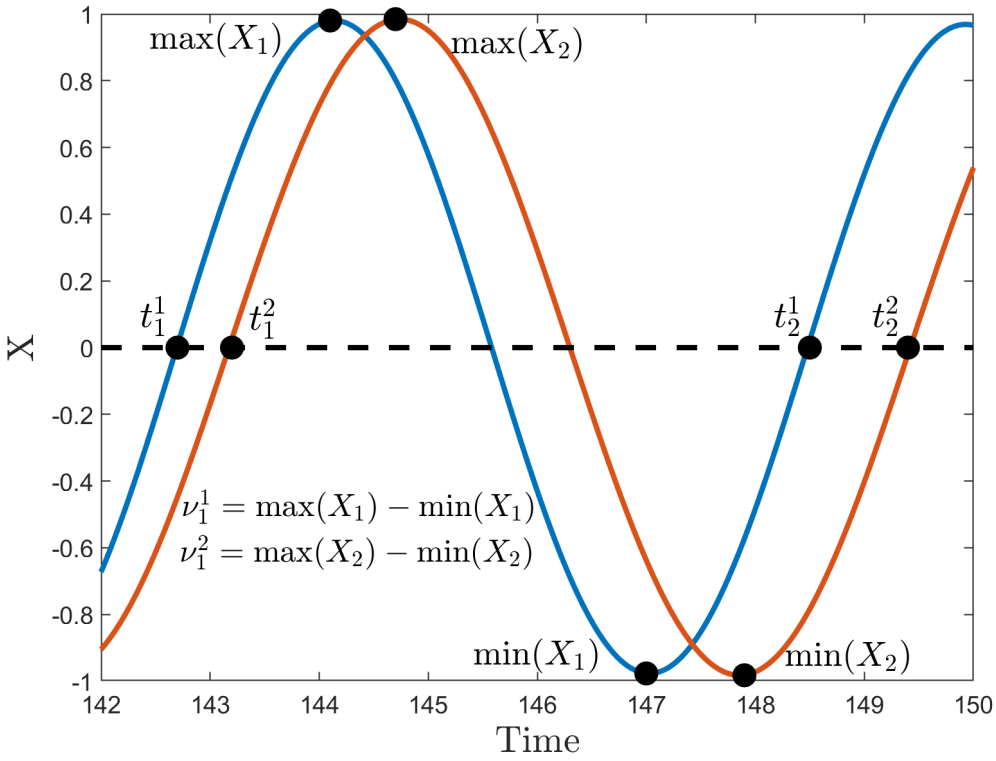

Figure 4.1: This figure demonstrates the calculation of $\nu_k = \max(X) - \min(X)$ over a single cycle for example data. Here, ν_k is an amplitude coordinate that is proportional to the system's slowest decaying isostable coordinate. In this figure, we again only plot two crossings of the $\theta = 0$ isochron for each oscillator and obtain an amplitude coordinate for the corresponding cycle between those crossings.

The original state in the full order model can be inferred from the reduced order dynamics since $x = f(\theta, \nu)$. Note that while p_i is usually unknown, it is only necessary to determine the ratios $\frac{\hat{c}_{0,i}}{p_i}$, $\frac{c_{n,k\to i}}{p_i}$, and $\frac{d_{n,k\to i}}{p_i}$ in the inference of (4.18).

4.3.2 The Data Driven Model: An Algorithm

The unknown coefficients from (4.18) can be approximated for m discrete time steps and $k = 1, ..., q$ coupled oscillators with the linear matrix equations

$$B_1 = A_1 F_1 \tag{4.19}$$

$$B_2 = A_2 F_1$$

where $B_1 \in R^{m\times 1}$, $A_1 \in R^{m\times(2q+1)}$, and $F_1 \in R^{(2q+1)\times 1}$ are defined below

$$B_1 = \begin{bmatrix} \dot{\theta}_i(t_1) & \cdots & \dot{\theta}_i(t_m) \end{bmatrix}^T, \tag{4.20}$$

$$A_1 = \begin{bmatrix} 1 & \sin\big(\phi_{i,1}(t_1)\big) & \cos\big(\phi_{i,1}(t_1)\big) & \cdots & \sin\big(\phi_{i,q}(t_1)\big) & \cos\big(\phi_{i,q}(t_1)\big) \\ \vdots & \vdots & \vdots & \vdots & \vdots & \vdots \\ 1 & \sin\big(\phi_{i,1}(t_m)\big) & \cos\big(\phi_{i,1}(t_m)\big) & \cdots & \sin\big(\phi_{i,q}(t_m)\big) & \cos\big(\phi_{i,q}(t_m)\big) \end{bmatrix},$$

$$F_1 = \begin{bmatrix} (\omega_i + \hat{a}_{0,i}) & a_{1,1\to i} & b_{1,1\to i} & \cdots & a_{1,q\to i} & b_{1,q\to i} \end{bmatrix}^T,$$

and $B_2 \in R^{m\times 1}$, $A_2 \in R^{m\times(2q+2)}$, and $F_2 \in R^{(2q+2)\times 1}$ are defined as

$$B_2 = \begin{bmatrix} \dot{\nu}_i(t_1) & \cdots & \dot{\nu}_i(t_m) \end{bmatrix}^T, \tag{4.21}$$

$$A_2 = \begin{bmatrix} \nu_i(t_1) & 1 & \sin\big(\phi_{i,1}(t_1)\big) & \cos\big(\phi_{i,1}(t_1)\big) & \cdots & \sin\big(\phi_{i,q}(t_1)\big) & \cos\big(\phi_{i,q}(t_1)\big) \\ \vdots & \vdots & \vdots & \vdots & \vdots & \vdots & \\ \nu_i(t_m) & 1 & \sin\big(\phi_{i,1}(t_m)\big) & \cos\big(\phi_{i,1}(t_m)\big) & \cdots & \sin\big(\phi_{i,q}(t_m)\big) & \cos\big(\phi_{i,q}(t_m)\big) \end{bmatrix},$$

$$F_2 = \begin{bmatrix} \kappa_i & \frac{\hat{c}_{0,i}}{p_i} & \frac{c_{1,1\to i}}{p_i} & \frac{d_{1,1\to i}}{p_i} & \cdots & \frac{c_{1,q\to i}}{p_i} & \frac{d_{1,q\to i}}{p_i} \end{bmatrix}^T.$$

In B_1 and B_2, the discrete approximations of $\dot{\theta}(t)$ and $\dot{\nu}(t)$ are determined by fluctuations in the time and state between crossings of some reference isochron. The discrete approximations of ν_i and $\phi_{i,k}$ can also be made by analyzing the time and state between crossings of some reference isochron. Therefore in a data-driven setting, F_1 and F_2 are the only unknowns while the elements of B_1, B_2, A_1, and A_2 can be determined from data. Above, only the first modes of the Fourier series expansions are computed for each coupling function. Additional modes can be obtained with appropriate modifications to A_1, A_2, F_1, and F_2.

A step-by-step explanation of how to estimate the elements of A_1, A_2, B_1, and B_2 and develop a phase-amplitude model in the form of Equation (4.18) using a least-squares approximation of the Fourier series coefficients is provided in the algorithm below.

1. Simulate the full order model (Equation (4.1)) for an extended period of time (approximately 50-100 oscillations). Determine a set of observables from which to obtain measurement data.

2. Define some value of each observable to be the $\theta = 0$ isochron for each oscillator. This can be a local maximum, local minimum, or some other cyclically repeating value (e.g., the crossing of $X = 0$ with a positive slope in Figure 4.2).

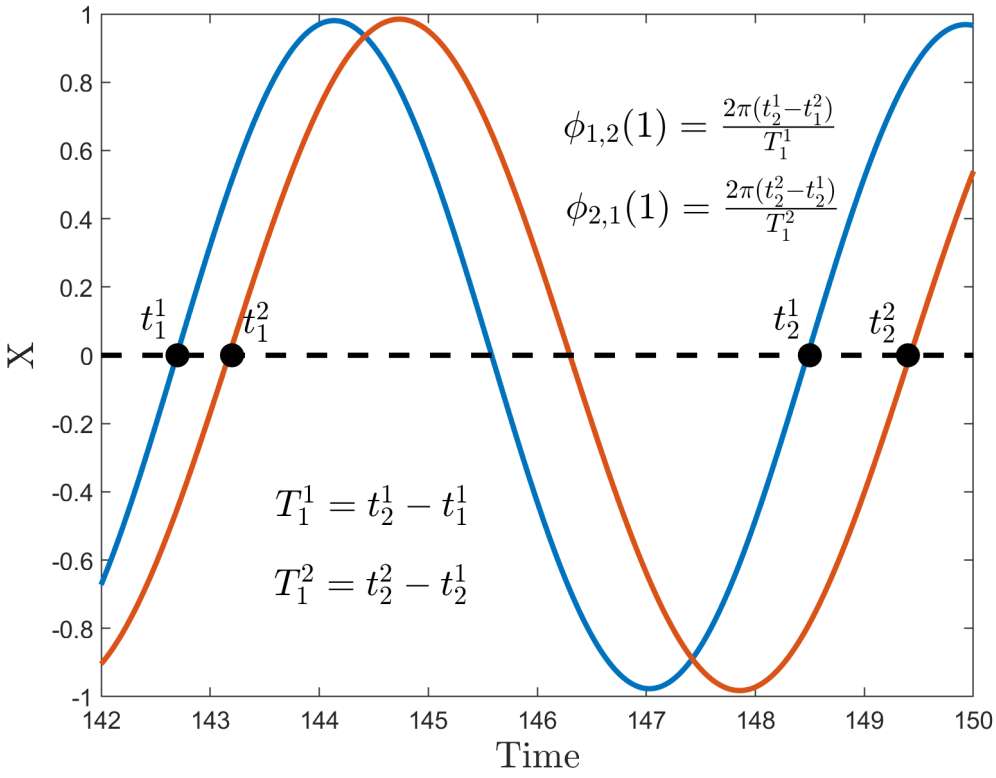

Figure 4.2: This figure demonstrates the determination of t_k, T_k, and $\phi_{i,j}(k)$ for example data. In this figure, we only plot two crossings of the $\theta = 0$ isochron for each oscillator (t_k^1 and t_k^2).

3. Extract each cycle of the chosen observables between crossings of the $\theta = 0$ isochron.

4. For each limit cycle oscillator, define the time of crossings of the $\theta = 0$ isochron by the chosen observable to be $t_1, t_2, ..., t_{N_{cross}}$ and the time between crossings to be $T_1 = (t_2 - t_1), T_2 = (t_3 - t_2), ..., T_{N_{cross}-1} = (t_{N_{cross}} - t_{N_{cross}-1})$ where N_{cross} is the total number of isochron crossings. Figure 4.2 illustrates these terms for a single example cycle.

5. For each limit cycle oscillator, define a chosen amplitude coordinate and calculate the amplitude for each cycle between crossings of the $\theta = 0$ isochron. Define the amplitudes to be $\nu_1, ..., \nu_{N_{cross}-1}$. Figure 4.1 illustrates this calculation for a single example cycle.

6. Use the time between crossings from Step 4 to approximate instantaneous measurements of $\dot{\theta}_i$ for each oscillator i. Store these measurements in the vector B_1.

$$B_1 = \left[\frac{2\pi}{T_1}, \frac{2\pi}{T_2}, ..., \frac{2\pi}{T_{N_{cross}-1}}\right]^T. \tag{4.22}$$

7. Use the time between crossings from Step 4 and the amplitudes from Step 5 to define discrete measurements of $\dot{\nu}_i$ for each oscillator i. Store these measurements in the vector B_2.

$$B_2 = \left[\frac{\nu_2 - \nu_1}{T_1}, \frac{\nu_3 - \nu_2}{T_2}, ..., \frac{\nu_{N_{cross}-1} - \nu_{N_{cross}-2}}{T_{N_{cross}-1}}\right]^T. \tag{4.23}$$

8. Define the phase difference between any two oscillators, i and j, at each isochron crossing k to be $\phi_{i,j}(t_k) = [2\pi \min(t_k^i - t^j)]/T_k^i$, where t_k^i is the k^{th} crossing by oscillator i of the $\theta = 0$ isochron, t^j are all crossings of the $\theta = 0$ isochron by oscillator j that occur before t_k^i, and $T_k^i = t_{k+1}^i - t_k^i$. Thus, we are solving for the closest crossing of the $\theta = 0$ isochron to t_k^i by oscillator j that occurs up to the time t_k^i. An example of this calculation for a single cycle of the $\theta = 0$ isochron can be found in Figure 4.2.

9. For each oscillator i: using the phase differences found in Step 8, set up matrix A_1 from Equation (4.20) using $m = N_{cross} - 1$ rows of Fourier series terms up to the desired order.

10. For each oscillator i: using the phase differences found in Step 8 and the amplitude values found in Step 5, set up matrix A_2 from Equation (4.21) using $m = N_{cross} - 1$ rows of Fourier series terms up to the desired order.

11. To determine the Fourier series coefficients for the phase dynamics, use Equation (4.19) with the B_1 vector from Step 6 and the A_1 matrix from Step 9 to solve for F_1.

$$F_1 = A_1^\dagger B_1 \tag{4.24}$$

Here † indicates a pseudoinverse.

12. To determine the Fourier series coefficients for the amplitude dynamics, use Equation (4.19) with the B_2 vector from Step 7 and the A_2 matrix from Step 10 to solve for F_2.

$$F_2 = A_2^\dagger B_2 \tag{4.25}$$

13. Run the phase-amplitude reduced order model defined in Equation (4.18) using the Fourier series coefficients stored in F_1 and F_2. Within the reduced order model, calculate the phase difference instantaneously.

14. To verify the efficacy of the reduced order model, map back to equivalent states in the full order model using the amplitude and phase coordinates to infer corresponding states in the full order model.

4.4 Example with a Simple Model: the Nonradial Isochron Clock

To illustrate the efficacy of our technique, we consider a simple model of two coupled oscillators of the form

$$\dot{X}_i = C_i\sigma X_i(\mu - (X_i^2 + Y_i^2)) - Y_i(C_i(1 + \rho(X_i^2 + Y_i^2 - \mu))) - \frac{\beta}{N-1}\sum_{j\neq i}^{N}(X_i - X_j), \tag{4.26}$$

$$\dot{Y}_i = C_i\sigma Y_i(\mu - (X_i^2 + Y_i^2)) + X_i(C_i(1 + \rho(X_i^2 + Y_i^2 - \mu))),$$

$$i = 1, .., N.$$

This equation is a modified version of Winfree's radial isochron clock [147] with added diffusive coupling. Here, $C_1 = 1.1$ and $C_2 = 1.0$ are constants that explicitly define the stable natural frequencies of the uncoupled oscillators: $\omega_1 = C_1 = 2\pi/T_1$ and $\omega_2 = C_2 = 2\pi/T_2$ where T_1 and T_2 are the associated stable periods of the uncoupled system. The parameters of the system are defined to be $\sigma = 0.08$, $\rho = 0.12$, and $\mu = 1$. The coupling strength between the oscillators is $\beta = 0.03$. Following the steps listed in Section 4.3.2, we will infer a data-driven phase-amplitude model that accurately captures the dynamics of (4.26).

4.4.1 Fitting the Model to Data

To begin, we simulated (4.26) for 600 time units. Defining the $\theta = 0$ isochron to be when both $X = 0$ and $\dot{X} > 0$ for a given oscillator, we extracted the individual cycles between isochron crossings. These cycles are plotted in Figure 4.3 for oscillator 1 in panel A and oscillator 2 in panel B.

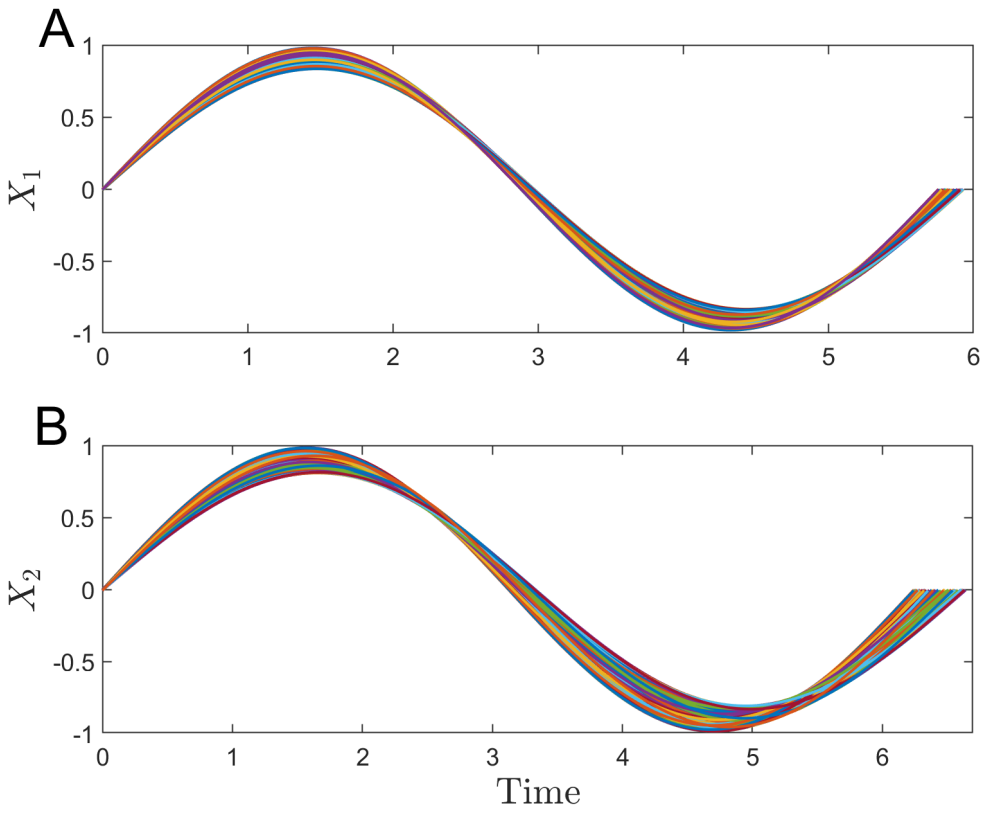

Figure 4.3: Cycles of the observables for the coupled two oscillator dynamics of the nonradial isochron clock. Panel A plots these cycles for the first oscillator and panel B plots these cycles for the second oscillator

Using this data, we found discrete approximations of $\dot{\theta}_i$, $\dot{\nu}_i$, ν_i and $\phi_{i,k}$ and defined A_1, B_1, A_2, and B_2 for each oscillator i following Steps 4-10 of Section 4.3.2. In this application, we defined the amplitude coordinate of the i^{th} oscillator to be $\nu_q^i = \max(X_q^i) - \min(X_q^i) - \nu_{0,i}$ for each q^{th} cycle between crossings of the $\theta = 0$ isochron. In this equation, $\nu_{0,i} = \frac{1}{N_{cross}-1} \sum_{q=1}^{N_{cross}-1} \big(\max(X_q^i) - \min(X_q^i) \big)$. With the B_1 vector and A_1 matrix, we evaluated Equation (4.24) and determined the Fourier series coefficients that govern the phase dynamics. With the B_2 vector and A_2 matrix, we evaluated Equation (4.25) and determined the Fourier series coefficients that govern the amplitude dynamics. The F_1 and F_2 vectors contain the Fourier series coefficients that are used in the phase-amplitude model defined in Equation (4.18). In this example, we used a first-order Fourier series approximation.

Figure 4.4 presents a direct comparison between the measured observables $\dot{\theta}_i$ as defined in Equation (4.22) and the evaluation of A_1F_1, where F_1 contains the Fourier series coefficients found using Equation (4.24).

Similarly, Figure 4.5 presents a comparison between the measured observables $\dot{\nu}_i$ from Equation (4.23) and the evaluation of A_2F_2, where F_2 contains the Fourier series coefficents found using Equation (4.25). In both figures, the observable data is shown in blue and our approximation using the Fourier series coefficients is in black. The X axis of both of these figures is the phase difference

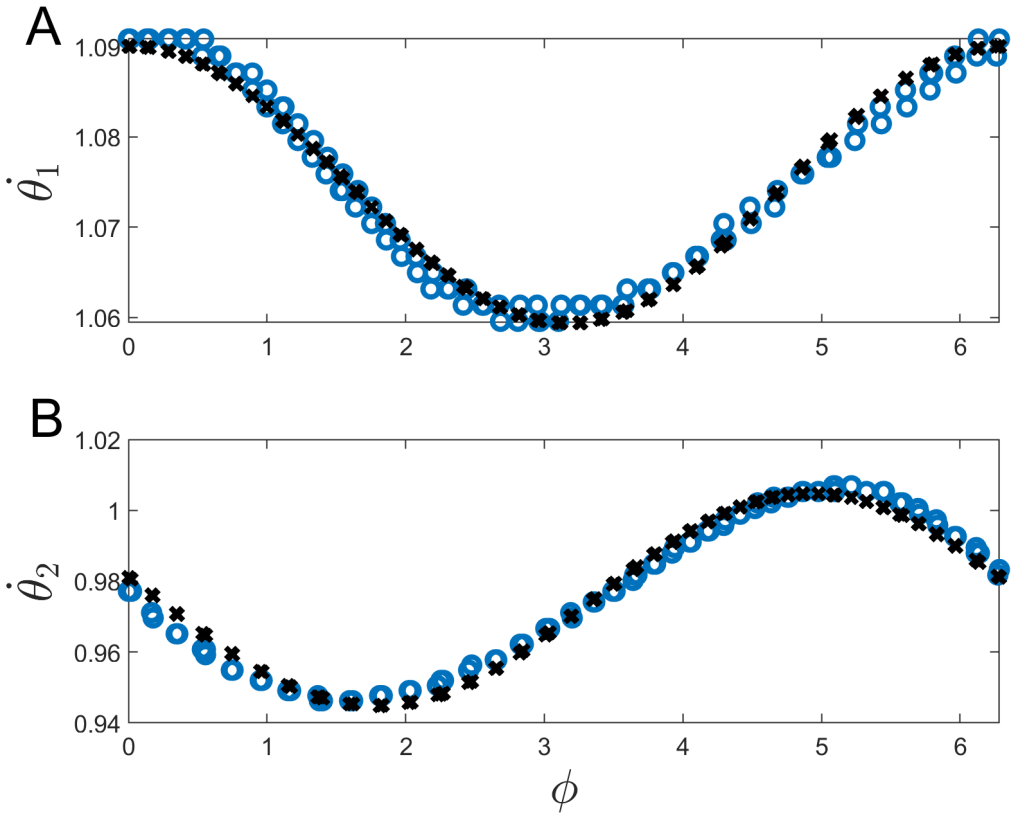

Figure 4.4: This figure validates the least-squares approximation of the Fourier series coefficients for the phase dynamics derived in Section 4.3.2. It directly compares the measured data defined in Equation (4.22) with the evaluation of A_1F_1, where A_1 and F_1 are calculated using the steps in Section 4.3.2. These are plotted as a function of the phase difference ϕ calculated in Step 8 of Section 4.3.2 and found in the terms of the A_1 matrix. The measured data from Equation (4.22) is shown in blue and the data from the evaluation of A_1F_1 is shown in black. Panel A presents these results for the first oscillator and panel B presents these results for the second oscillator.

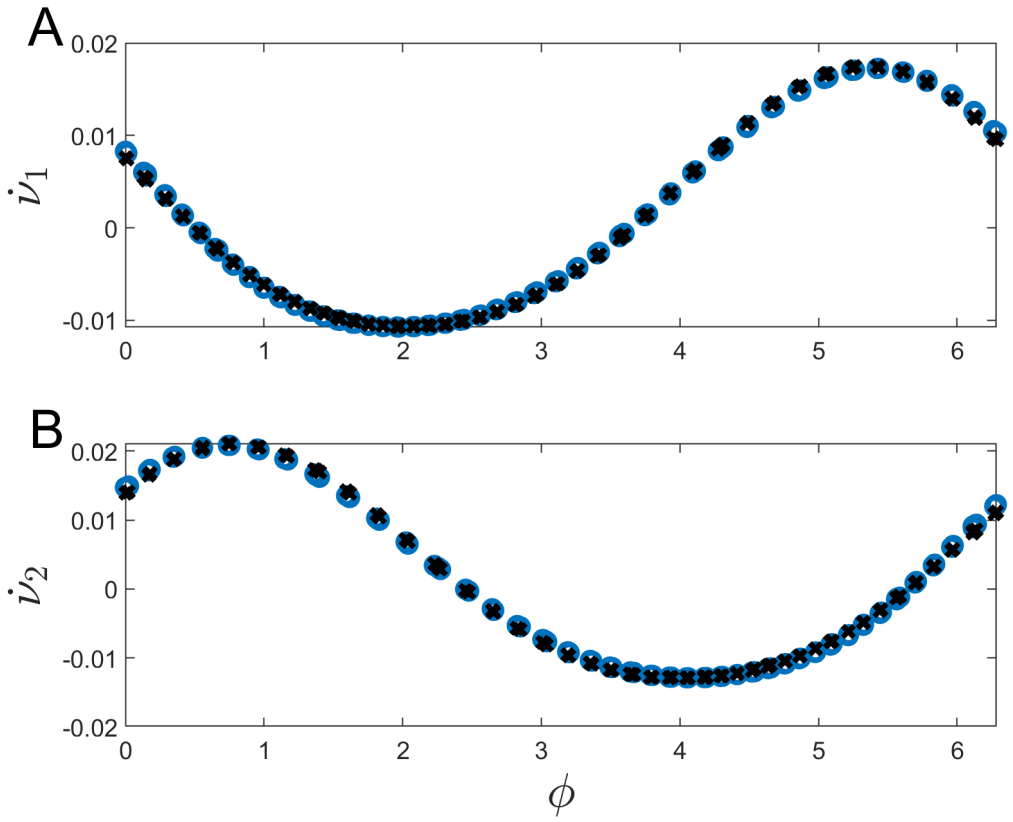

Figure 4.5: This figure validates the least-squares approximation of the Fourier series coefficients for the amplitude dynamics derived in Section 4.3.2. It directly compares the measured data defined in Equation (4.23) with the evaluation of A_2F_2, where A_2 and F_2 are calculated using the steps in Section 4.3.2. These are plotted as a function of the phase difference ϕ calculated in Step 8 of Section 4.3.2 and found in the terms of the A_2 matrix. The measured data from Equation (4.23) is shown in blue and the data from the evaluation of A_2F_2 is shown in black. Panel A presents these results for the first oscillator and panel B presents these results for the second oscillator.

between the oscillators ϕ used in the A_1 and A_2 matrices. In both figures, panel A presents the information for the first oscillator and panel B presents it for the second oscillator.

4.4.2 Comparisons Between Ground Truth and Inferred Model Simulations

To test the model, we simulated Equation (4.18) using the derived Fourier series coefficients found using Equations (4.24) and (4.25). The phase and amplitude coordinates for this simulation are shown in Figure 4.6 for a 200 time unit snapshot.

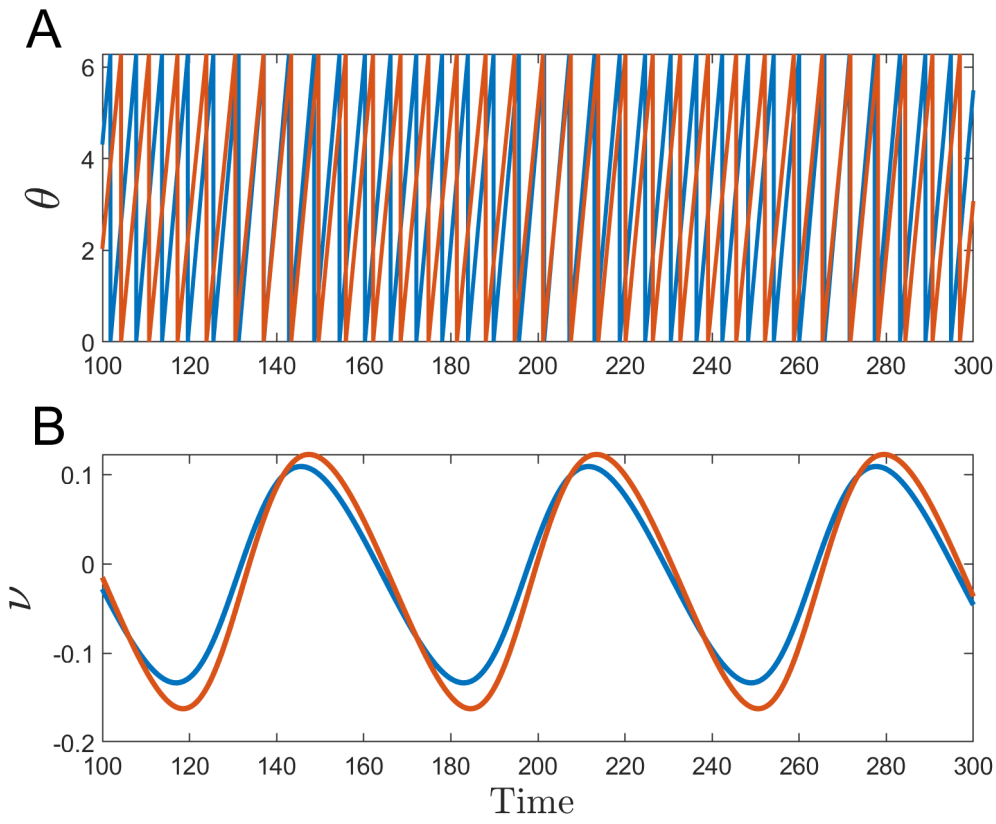

Figure 4.6: The phase and amplitude dynamics of the phase-amplitude model. Panel A presents the phase dynamics of the first oscillator in blue and the second oscillator in red. Panel B presents the amplitude dynamics of the first oscillator in blue and the second oscillator in red.

We compare the ground truth model with the phase-based model by approximating the identical initial conditions of the full order model in the phase space and evolving the phase-based model defined in Equation 4.18 forward in time. We present a comparison of the ground truth and phase-based simulations in Figure 4.7. In this comparison, we have mapped the phase-based model back to its comparable state in the full order model using the relationship $x = f(\theta, \nu)$.

For further validation of the data-driven phase-amplitude model, we also compare the data-driven phase coupling function found using Equation (4.16) to the actual phase coupling function computed analytically from the equations governing the system's dynamics. For our analytical calculation, we computed the phase response curves for each oscillator numerically using methods

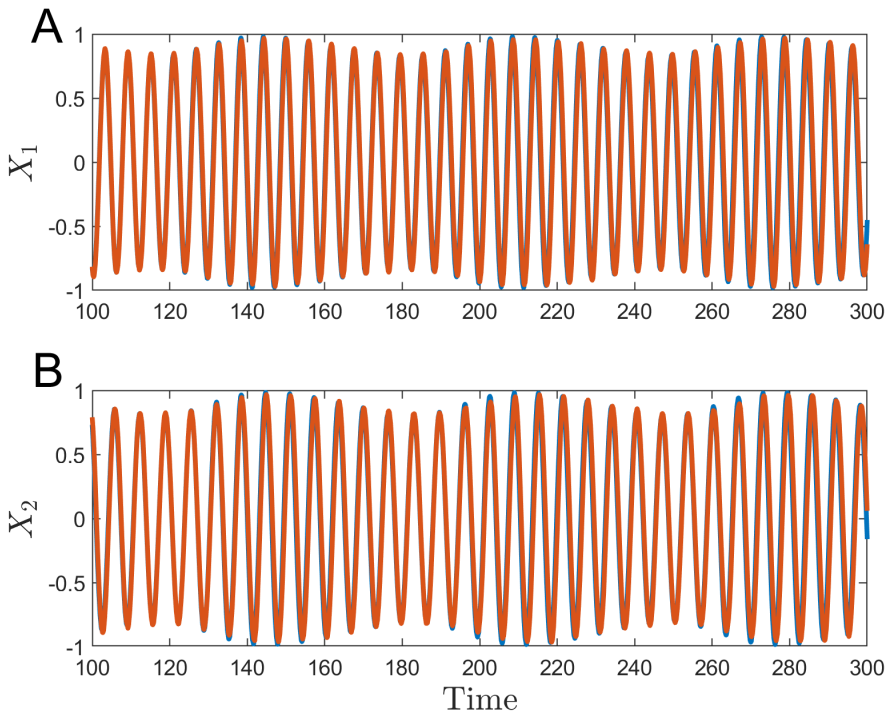

Figure 4.7: This figure compares the full order model with dynamics defined in Equation (4.26) to the inferred state from the phase-amplitude model with dynamics defined in Equation (4.18). Panel A compares the dynamics of the X_1 variable in the full order model and phase-amplitude model. Panel B compares the dynamics of the X_2 variable in the full order model and phase-amplitude model. In both panels, the state in the full order model is plotted in blue and the comparable state derived from the phase-based model is shown in red. In each panel, the curves are nearly indestinguishable.

described in [75], and then calculated the coupling function according to

$$\Gamma_{\zeta,k\to i}(\phi_{i,k}) = -\beta\frac{1}{T_0}\int_0^{T_0} Z_i(\zeta_i+\omega_0 t)\Big(X_i(\zeta_i+\omega_0 t) - X_j(\zeta_i+\omega_0 t-\phi_{i,j})\Big)dt. \tag{4.27}$$

Here, $\omega_0 = 2\pi/T_0$ and T_0 is the average period of the two oscillators. For this comparison, we reduced the heterogeneity so that the natural frequencies of the coupled oscillators were $C_1 = \omega_1 = 0.99$ and $C_2 = \omega_2 = 1.01$. We also decreased the coupling strength to $\beta = 0.008$. This ensured that the timescales of the terms in the averaged equations were close. The coupling functions are presented in Figure 4.8 and are plotted over the phase difference ϕ. The coupling functions for the first oscillator are shown in panel A, and the coupling functions for the second oscillator are shown in panel B.

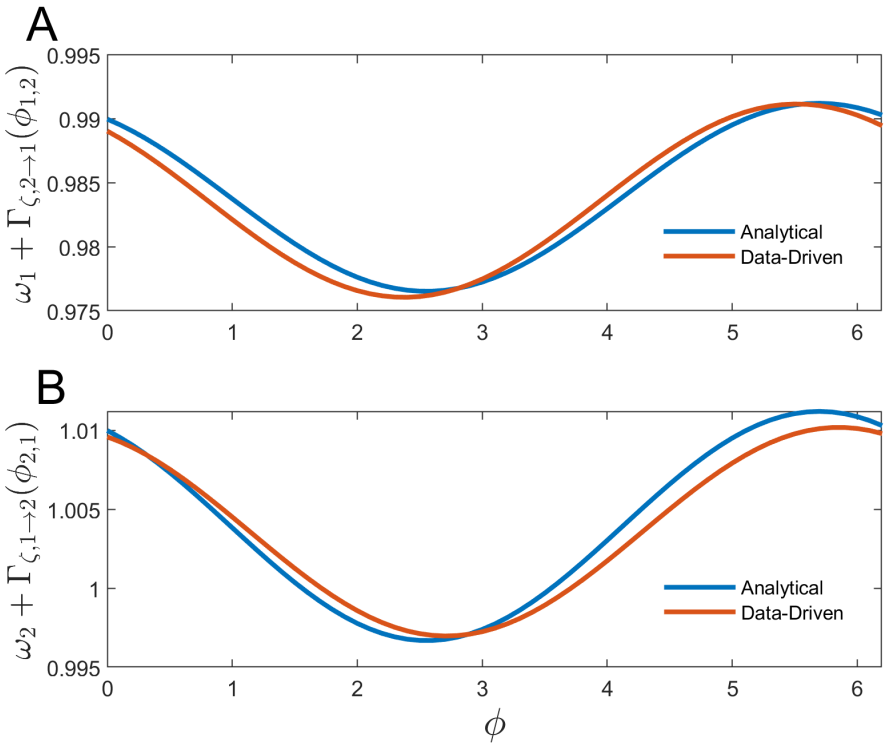

Figure 4.8: This figure compares the numerically computed coupling functions defined in Equation (4.27) to the data-driven coupling functions defined in Equation (4.16) for a pair of coupled oscillators. Panel A presents this comparison for the first oscillator and panel B presents the comparison for the second oscillator.

4.5 Neural Population-Level Oscillations

The primary motivation for this work is the application of this data-driven technique to coupled neural subnetworks. The existence of population-level neural dynamics has been studied since the electroencephalogram (EEG) first recorded electrical activity in the brain [44],[129]. Since then, numerous researchers have investigated these population-level dynamics to uncover their reasons and functions [2], [29], [80], [28], [130]. Recent research has also considered population-level oscillations in computational neural models [11], [123], [122].

The conductance-based neural model used in this work has voltage dynamics

$$\frac{\dot{V}_i}{C} = I_{b_i} - I_L(V_i) - I_{Na}(V_i, h_i) - I_K(V_i, h_i) - I_T(V_i, r_i) + I_{c_i} + \sqrt{2D}\eta_i(t), \qquad (4.28)$$
$$i = 1, ..., N,$$

where I_{b_i} is a baseline stimulus, I_L, I_{Na}, I_K and I_T are ionic currents, I_{c_i} is the current due to coupling, and $\sqrt{2D}\eta_i$ is a white noise process that is independent for each neuron. A full explanation of additional variables and parameters can be found in Appendix B. In a data-driven setting the underlying dynamics and coupling structure of the individual oscillators are unknown. Instead, we assume that the only measured observable we can obtain from the system is the average voltage of each subnetwork

$$\bar{V}_m = \frac{1}{N_m} \sum_{i=1}^{N_m} V_i, \tag{4.29}$$

where N_m is the number of neurons in the m^{th} subnetwork. Figure 4.9 presents an example network of four subnetworks, where each subnetwork contains a population of neurons whose coupling structure reflects the coupling defined in Equation (B.4). The neurons within each subnetwork are coupled with electrotonic coupling. Coupling between neurons in different subnetworks is inhibitory or excitatory synaptic coupling. The electrotonic coupling between neurons within the same subnetwork exerts a stronger force than the synaptic coupling between neurons in different subnetworks. We assume that each subnetwork has an associated population-level limit cycle. The following two sections will discuss the application of our data-driven technique on neuronal networks of two and four subnetworks.

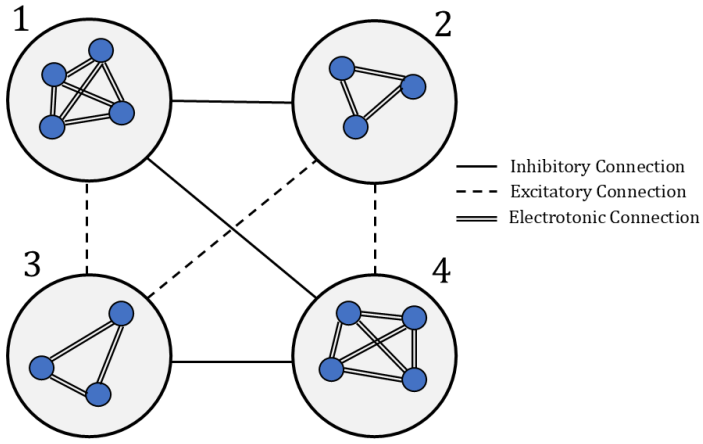

Figure 4.9: A network containing four neuronal subnetworks. Neurons within each subnetwork are interconnected with electrotonic coupling. Neurons in different subnetworks are coupled with inhibitory or excitatory synaptic coupling.

4.6 Results: A Neuronal Network of Two Subnetworks

First we considered a two subnetwork system of $N = 1000$ neurons with dynamics defined in Equation (B.1) and related equations in Appendix B. A complete description of the parameters in this model can be found in Section B.1 of Appendix B. Below, we present our methodology and results following the steps given in Section 4.3.2.

4.6.1 Fitting the Model to Data

To begin, we evaluated this system for 2000 ms and obtained voltage dynamics for all $N = 1000$ neural oscillators. We then calculated the average voltage of the oscillators in each subnetwork $\bar{V}_m$ using Equation (4.29). The voltages for the neurons in each subnetwork are presented in Figure 4.10 for a 200 ms snapshot, with panel A plotting the voltages in the first subnetwork and panel B plotting the voltages in the second. The average voltage of each subnetwork as defined in Equation (4.29) is overlayed in black on the respective panel, demonstrating the existence of population-level oscillations.

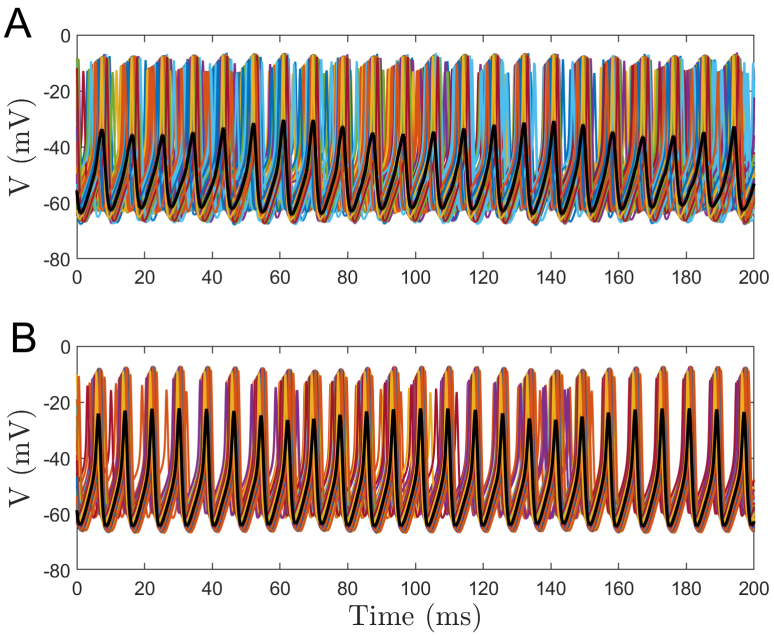

Figure 4.10: Voltage dynamics of all neurons in a two subnetwork system. Panel A presents the voltages for the first subnetwork, and panel B presents the voltages for the second subnetwork. A black trace on each panel represents the average voltage of that subnetwork which are taken as the observables for this system.

Our proposed strategy is implemented using the average voltage of each subnetwork as the observable. We define the $\theta = 0$ isochron to be when $\bar{V}_1 = -51.3$ mV with $\dot{\bar{V}}_1 > 0$ for the first subnetwork and $\bar{V}_2 = -50.7$ mV with $\dot{\bar{V}}_2 > 0$ for the second subnetwork. These values are equivalent to the mean values of $\bar{V}$ for each subnetwork. We then extracted the average voltage dynamics between subsequent crossings of the $\theta = 0$ isochron for each subnetwork. We have plotted these cycles in Figure 4.11, with panel A showing the information for the first subnetwork, and panel B showing the information for the second subnetwork. Note that these cycles are plotted over time so that we can visually see the variation in both the amplitude of the oscillations as well as the time between isochron crossings.

From the data in Figure 4.11, we found discrete approximations of $\dot{\theta}_i$, $\dot{\nu}_i$, ν_i and $\phi_{i,k}$ and defined A_1, B_1, A_2, and B_2 following Steps 4-10 of Section 4.3.2. In this application, we chose the amplitude coordinate of the i^{th} oscillator to be $\nu_q^i = \max(\bar{V}_q^i) - \min(\bar{V}_q^i) - \nu_{0,i}$, where $\nu_{0,i} = \frac{1}{N_{cross}-1}\sum_{q=1}^{N_{cross}-1}\big(\max(\bar{V}_q^i) - \min(\bar{V}_q^i)\big)$. With the B_1 vector and A_1 matrix, we evaluated Equation (4.24) and determined the Fourier series coefficients that govern the phase dynamics. With the B_2

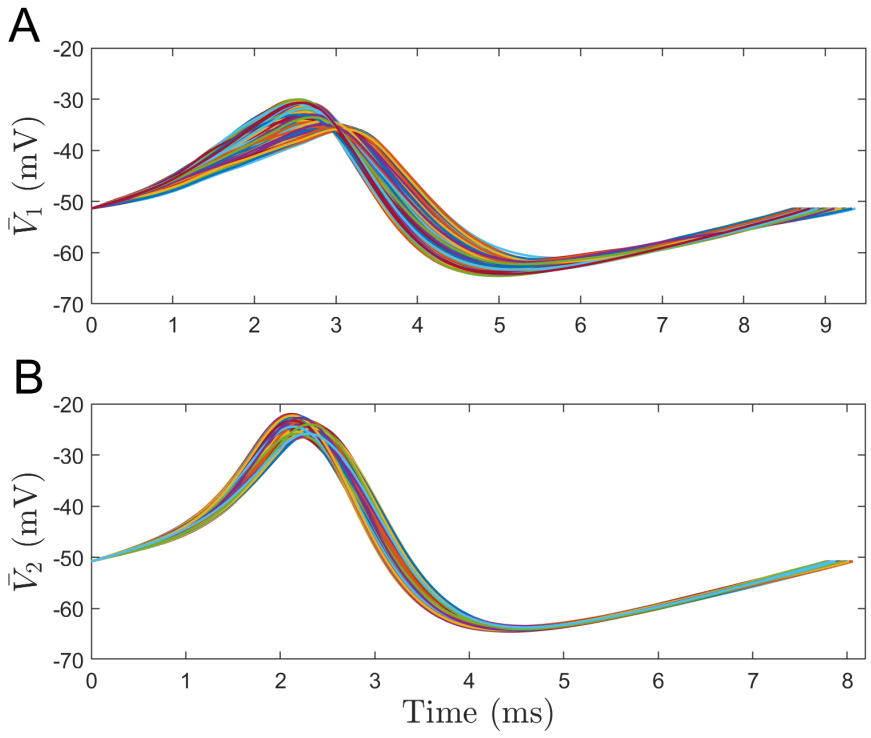

Figure 4.11: Voltage dynamics between $\theta = 0$ isochron crossings for each subnetwork. Panel A presents the dynamics for the first subnetwork, and panel B presents the dynamics for the second subnetwork.

vector and A_2 matrix, we evaluated Equation (4.25) and determined the Fourier series coefficients that govern the amplitude dynamics. The F_1 and F_2 vectors contain the Fourier series coefficients that are used in the reduced order model defined in Equation (4.18). In this example, we used a second-order Fourier series approximation.

In Figure 4.12, we present a direct comparison between measured observables $\dot{\theta}_i$ as defined in Equation (4.22) and the evaluation of A_1F_1, where F_1 contains the Fourier series coefficients calculated using Equation (4.24).

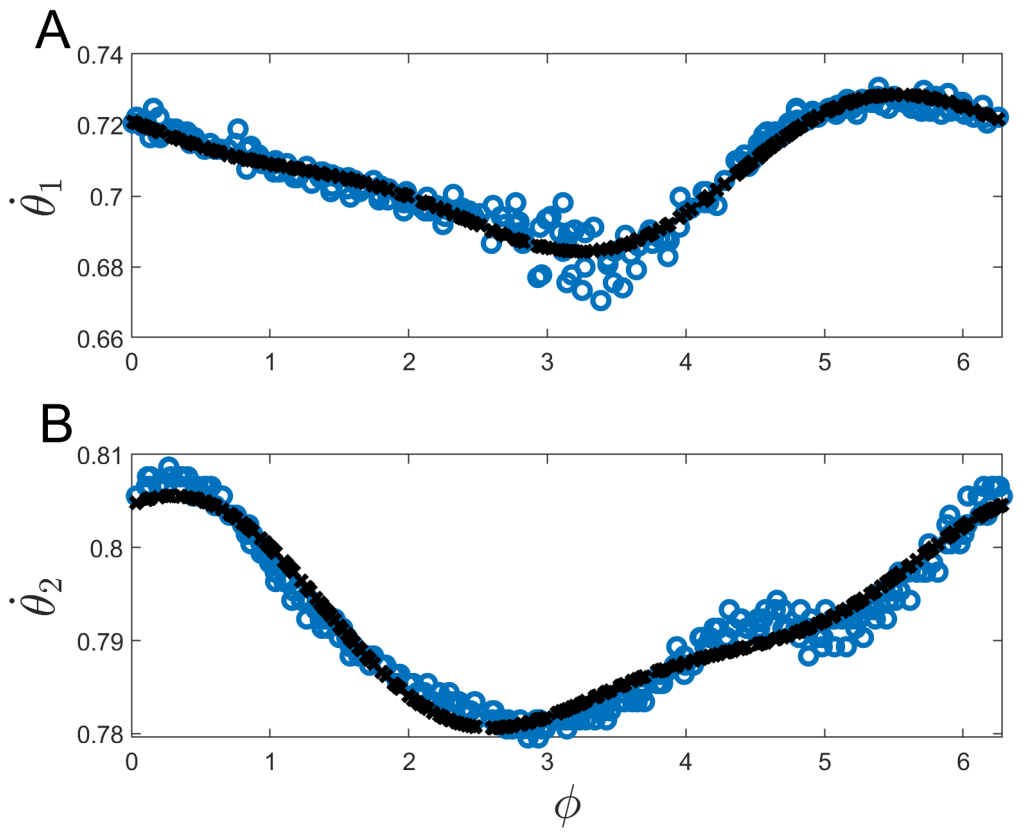

Figure 4.12: This figure validates the least-squares approximation of the Fourier series coefficients for the phase dynamics derived in Section 4.3.2. It directly compares the measured data defined in Equation (4.22) with the evaluation of A_1F_1, where A_1 and F_1 are calculated using the steps in Section 4.3.2. They are plotted as a function of the phase difference ϕ calculated in Step 8 of Section 4.3.2 and found in the terms of the A_1 matrix. The measured data from Equation (4.22) is shown in blue and the data from the evaluation of A_1F_1 is shown in black. Panel A presents the results for the first subnetwork and panel B presents the results for the second subnetwork.

Similarly, Figure 4.13 presents a comparison between the measured observables $\dot{\nu}_i$ from Equation (4.23) and the evaluation of A_2F_2, where F_2 contains the Fourier series coefficients found using Equation (4.25). In both Figure 4.12 and Figure 4.13, the observable data is shown in blue and our approximation using Fourier series coefficients is shown in black. The X axis of both figures is the phase difference between the subnetworks ϕ that is used in the A_1 and A_2 matrices. In both figures, panel A presents this information for the first subnetwork and panel B presents this information for the second subnetwork.

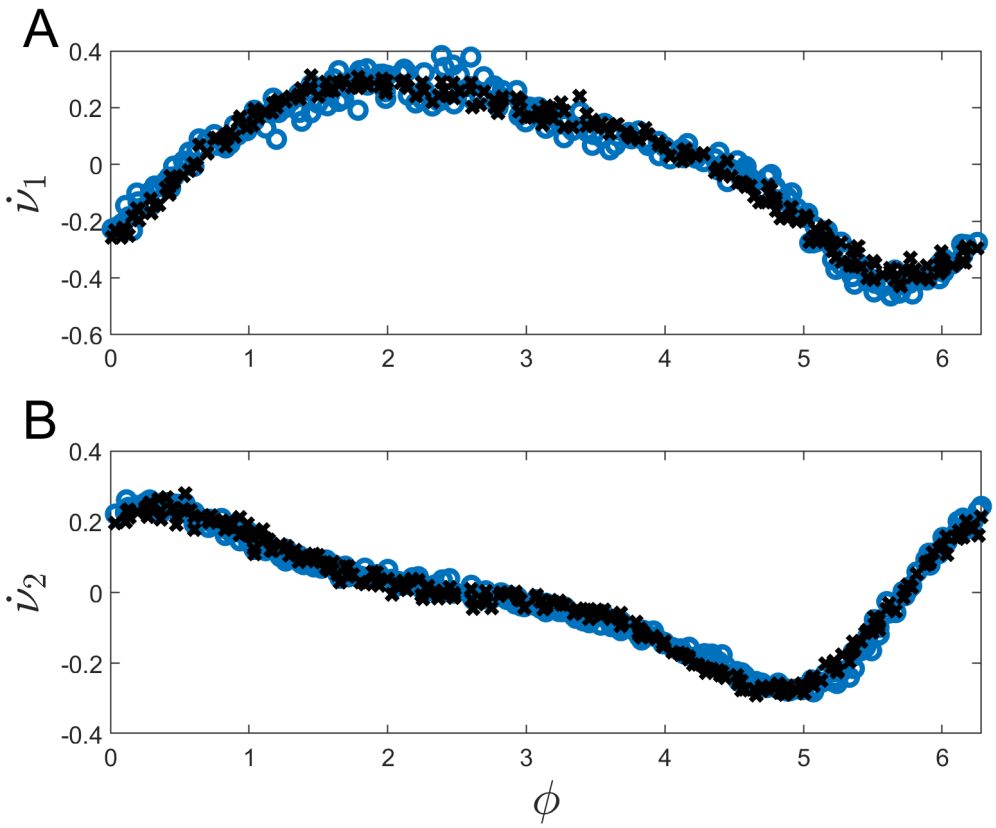

Figure 4.13: This figure validates the least-squares approximation for the amplitude dynamics derived in Section 4.3.2. It directly compares the measured data defined in Equation (4.23) with the evaluation of A_2F_2, where A_2 and F_2 are calculated following the steps in Section 4.3.2. These are plotted as a function of the phase difference ϕ calculated in Step 8 of Section 4.3.2 and found in the terms of the A_2 matrix. The measured data from Equation (4.23) is shown in blue and the data from the evaluation of A_2F_2 is shown in black. Panel A presents the results for the first subnetwork and panel B presents the results for the second subnetwork.

4.6.2 Comparisons Between Ground Truth and Inferred Model Simulations

Finally, to test the model, we simulated the reduced order model defined in Equation (4.18) using the Fourier series coefficients found using Equations (4.24) and (4.25). The phase and amplitude coordinates from this simulation are shown in Figure 4.14 for a 200 ms snapshot.

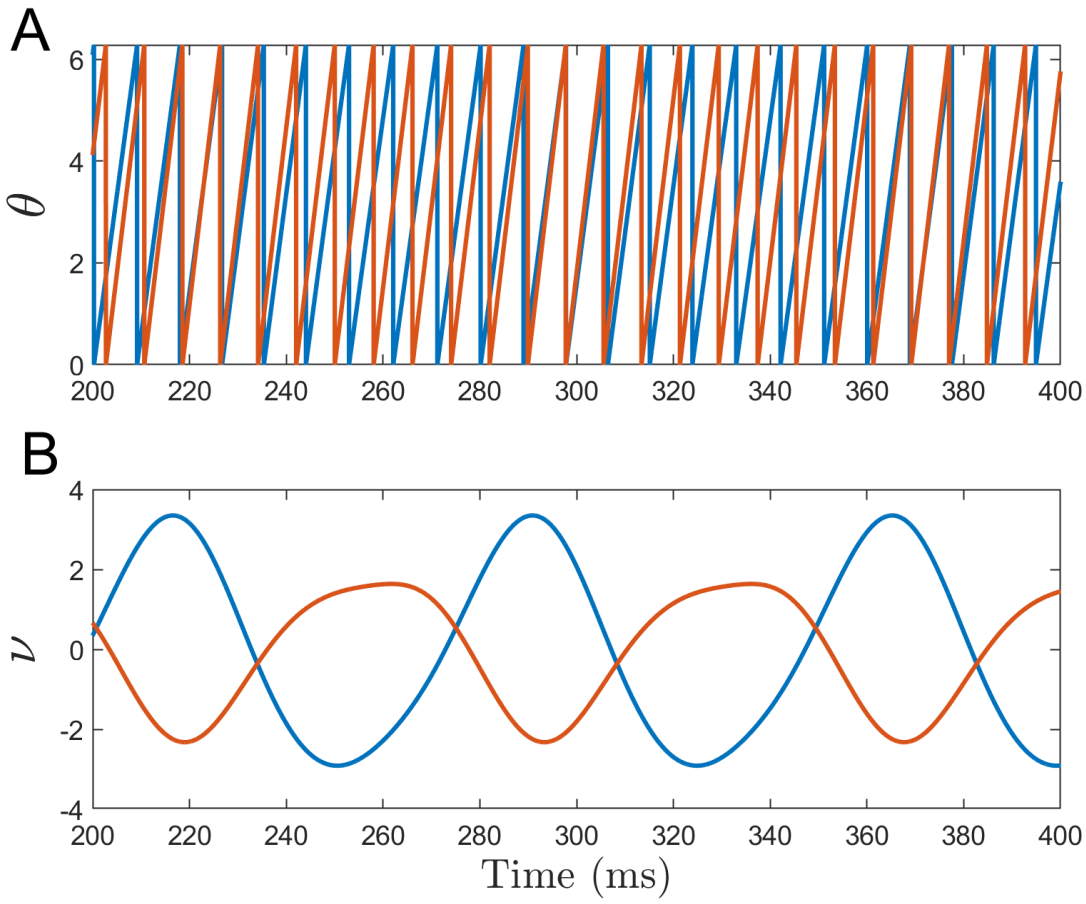

Figure 4.14: The phase and amplitude dynamics of the reduced order model. Panel A presents the phase dynamics of the first subnetwork in blue and the second subnetwork in red. Panel B presents the amplitude dynamics of the first subnetwork in blue and the second subnetwork in red.

We compare the ground truth model with the reduced order model by approximating identical initial conditions of the full order model in the phase space and evolving the reduced order model forward in time. We present a comparison of the two simulations in Figure 4.15. For this

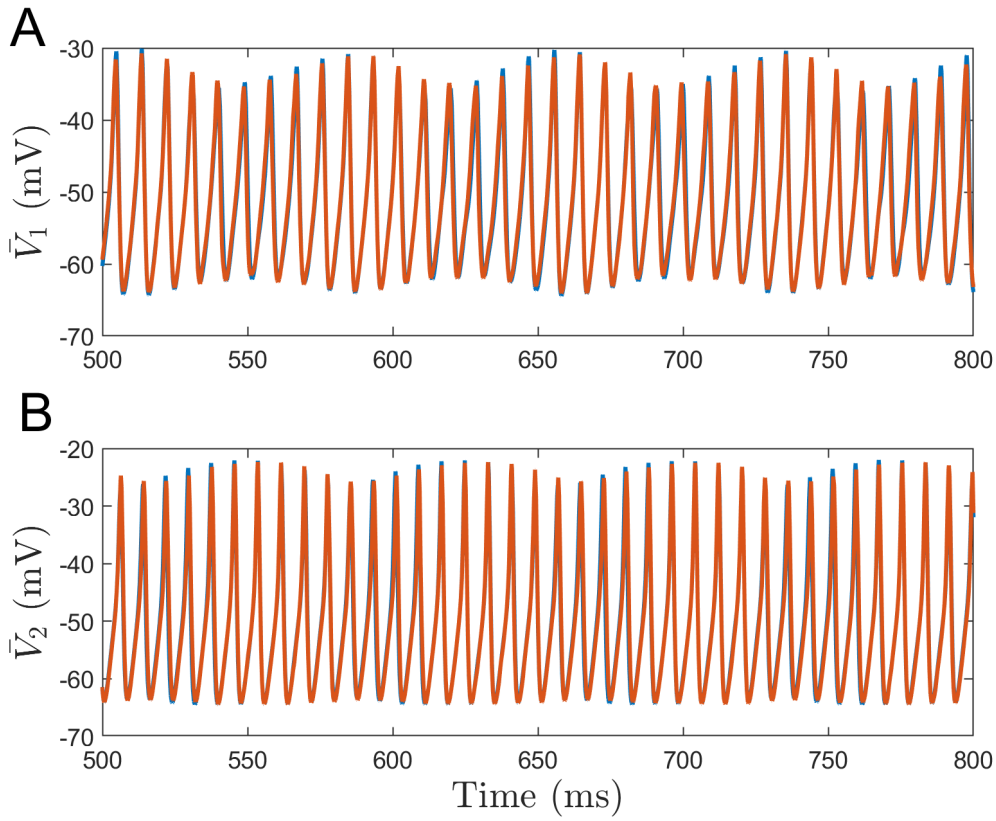

Figure 4.15: This figure compares the full order model with dynamics defined in Equations (B.1)-(B.5) in Appendix B to the comparable states inferred from the reduced order model defined in Equation (4.18). Panel A (resp., B) compares the dynamics of $\bar{V}_1$ (resp., $\bar{V}_2$) in the full and reduced order models. In both panels, the state in the full order model is plotted in blue and the comparable state derived from the reduced order model is shown in red. In each panel, the curves are again almost indistinguishable.

comparison, we have mapped the reduced order model back to its comparable state in the full order model using the relationship $x = f(\theta, \nu)$.

For additional validation of the data-driven reduced order model, we also present Figure 4.16 which plots the normalized count of voltage values for each subnetwork in both the full and reduced order models. Along with this, we also computed the variance of the full and reduced order models for each subnetwork. In the first subnetwork, the variance of $\bar{V}_1$ is 88.8 for the full order model and 88.4 for the reduced order model. In the second subnetwork, the variance is 142.6 for the full order model and 142.6 for the reduced order model. Figure 4.16 along with the variances support the visual results presented in Figure 4.15, demonstrating that the data-driven reduced order model yields a close approximation to the full order model.

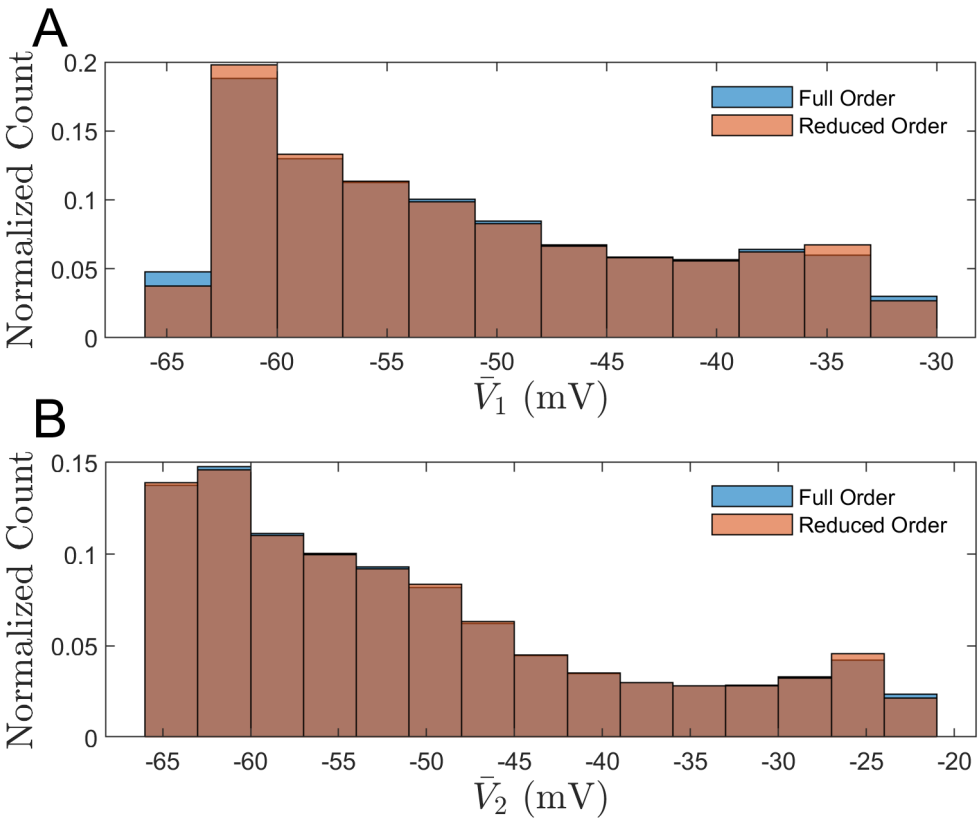

Figure 4.16: This figure presents the normalized count of $\bar{V}$ values for the full and reduced order model. Panel A presents this data for the first subnetwork. Panel B presents this data for the second subnetwork.

Finally, to clearly demonstrate the importance of coupling in the evaluation of our system's phase response curves, we present Figure 4.17. In this figure, a series of phase response curves are computed numerically using variations of the direct method. In the direct method, a series of perturbations applied to the full order model are used to find an approximate phase response curve of the form $Z(\theta)$. Each plot in Figure 4.17 is a single phase response curve obtained from a sample of 40 different perturbations. In blue, we compute phase response curves that account for coupling, while in red we do not account for coupling.

To begin the numerical computation of these PRCs, we first simulated the full order model defined in Equation (B.1) and applied a series of perturbations to all neurons in a single subnetwork (the perturbed subnetwork). Since the average voltage of the perturbed subnetwork $\bar{V}$ is known at the time of perturbation t_p, the phase θ can be inferred.

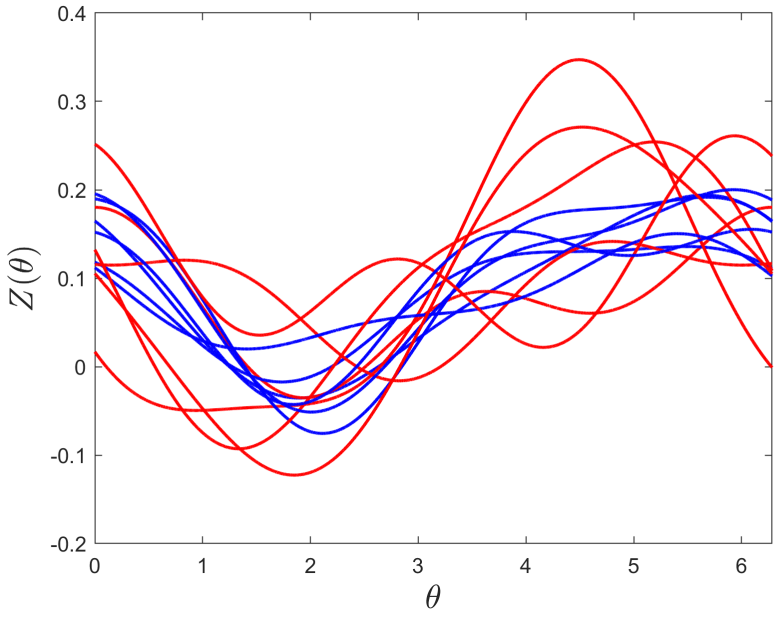

Figure 4.17: Various numerical approximations of a single subnetwork's phase response curve using the direct method. The curves in blue incorporate coupling in the computation of the numerical PRCs while the curves in red do not incorporate coupling.

To approximate $d\theta$, we find a crossing of the $\theta = 0$ isochron 2-3 cycles after the time of perturbation t_p. At this time t_m the perturbed phase $\theta_p = 0$. To determine the unperturbed phase and account for coupling, we simulate Equation (4.18) over the time span $t \in [0, (t_m - t_p)]$. The phase of the perturbed subnetwork at the end of this simulation is the unperturbed phase θ_u. To determine the unperturbed phase without coupling, simulate $\dot{\theta}_i = \omega_{0,i}$ over the time span $t \in [0, (t_m - t_p)]$. In this equation, we approximate $\omega_{0,i} = 2\pi/T_{0,i}$ and $T_{0,i} = \sum T_i$ where T_i is the time between subsequent crossings of the $\theta = 0$ isochron. The phase of the perturbed subnetwork at the end of this simulation is the unperturbed phase, θ_u. Solve $d\theta = \theta_p - \theta_u$, and then approximate $Z(\theta) = d\theta/(u\Delta t_p)$ where u is the magnitude of the perturbation and Δt_p is the time span that the perturbation is applied.

Without incorporating coupling, the red PRCs appear noisy with no discernible average curve. However, the blue plots evaluated using Equation (4.18) and incorporating coupling appear much more consistent and follow a discernible curve. Using a larger number of perturbations to compute the phase response curves would yield more accurate approximations to the actual phase response curve.

4.7 Results: A Neuronal Network of Four Subnetworks

Finally we considered a four subnetwork system of $N = 1000$ neurons with dynamics defined in Equation (B.1) and related equations in Appendix B. A complete description of the parameters of this model can be found in Section B.2 of Appendix B. We present our methodology and results in chronological order following the steps given in Section 4.3.2 below.

4.7.1 Fitting the Model to Data

We evaluated this system for 2000 ms and obtained voltage dynamics for all $N = 1000$ neural oscillators. We calculated the average voltage of the oscillators in each subnetwork $\bar{V}_m$ using Equation (4.29). The voltages for the neurons in each subnetwork are presented in Figure 4.18 for a 200 ms snapshot, with panels A-D plotting the voltages in subnetworks 1-4, respectively. The average voltage of each subnetwork as defined in Equation (4.29) is overlayed in black on the respective panels, demonstrating the existence of population-level oscillations.

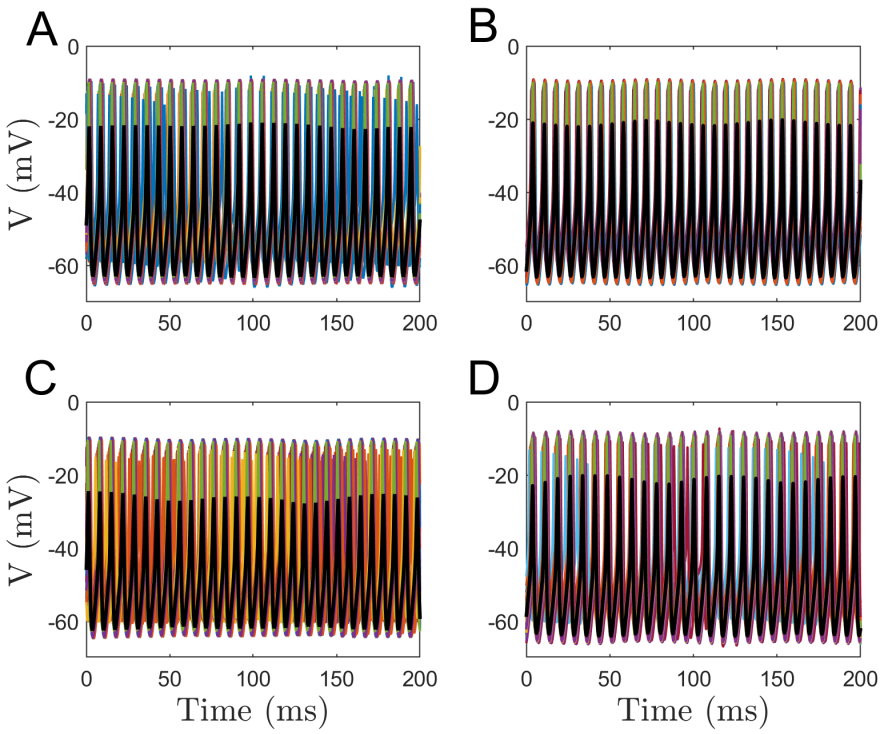

Figure 4.18: Voltage dynamics for all neurons in a four subnetwork system. Panels A-D present the voltages for subnetworks 1-4, respectively. A black trace on each panel represents the average voltage of that subnetwork, which are the observables for this system.

Our proposed strategy is implemented using the average voltage of each subnetwork as the observable. We define the $\theta = 0$ isochron to be when $\bar{V}_1 = -50.0$ mV and $\dot{\bar{V}}_1 > 0$ for the first subnetwork, $\bar{V}_2 = -50.1$ mV and $\dot{\bar{V}}_2$ for the second subnetwork, $\bar{V}_3 = -50.0$ mV and $\dot{\bar{V}}_3 > 0$ for the third subnetwork, and $\bar{V}_4 = -50.1$ and $\dot{\bar{V}}_4 > 0$ for the fourth subnetwork. These values are equivalent to the mean values of $\bar{V}$ for each subnetwork. We extracted the average voltage between subsequent crossings of the $\theta = 0$ isochron for each subnetwork. These cycles are plotted in Figure 4.19, with panels A-D showing the information for subnetworks 1-4 respectively. These cycles are plotted over time so that we can visually identify variation in the amplitude of the oscillations as well as the time between isochron crossings.

Using the data in Figure 4.19, we found discrete approximations of $\dot{\theta}$, $\dot{\nu}$, ν_i and $\phi_{i,k}$ and defined A_1, B_1, A_2, and B_2 following Steps 4-10 of Section 4.3.2. In this application, we chose the amplitude coordinate to be $\nu_q = \max(\bar{V}_q^i) - \min(\bar{V}_q^i) - \nu_{0,i}$ where $\nu_{0,i} = \frac{1}{N_{cross}-1} \sum_{q=1}^{N_{cross}-1} \big(\max(\bar{V}_q^i - \min(\bar{V}_q^i) \big)$. With the B_1 vector and A_1 matrix, we evaluated Equation (4.24) and determined the Fourier series

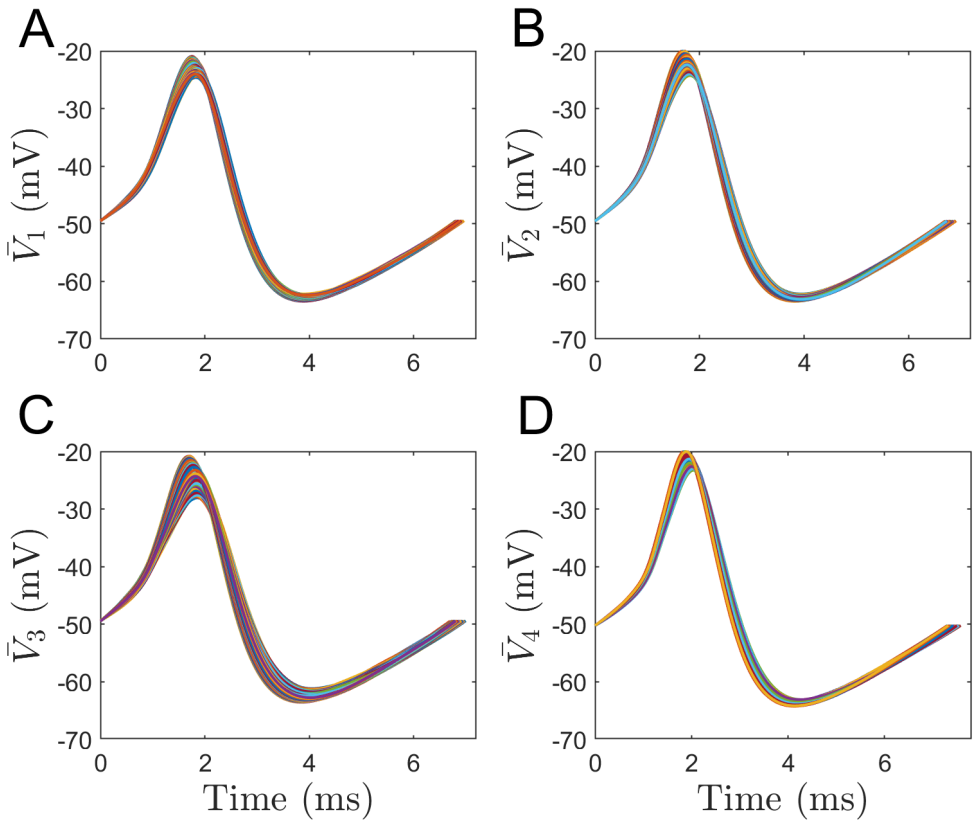

Figure 4.19: Voltage dynamics between $\theta = 0$ isochron crossings for each subnetwork. Panels A-D present the dynamics for subnetworks 1-4, respectively.

coefficients that govern the phase dynamics. With the B_2 vector and A_2 matrix, we evaluated Equation (4.25) and determined the Fourier series coefficients that govern the amplitude dynamics. The F_1 and F_2 vectors contain the Fourier series coefficients that are used in the reduced order model defined in Equation (4.18). For this example, we again used a second-order Fourier series approximation.

4.7.2 Comparisons Between Ground Truth and Inferred Model Simulations

Finally, to test our method, we simulated the reduced order model defined in Equation (4.18) with the Fourier series coefficients found using Equations (4.24) and (4.25). The phase and amplitude coordinates obtained from this simulation are shown in Figure 4.20 for a 200 ms snapshot.

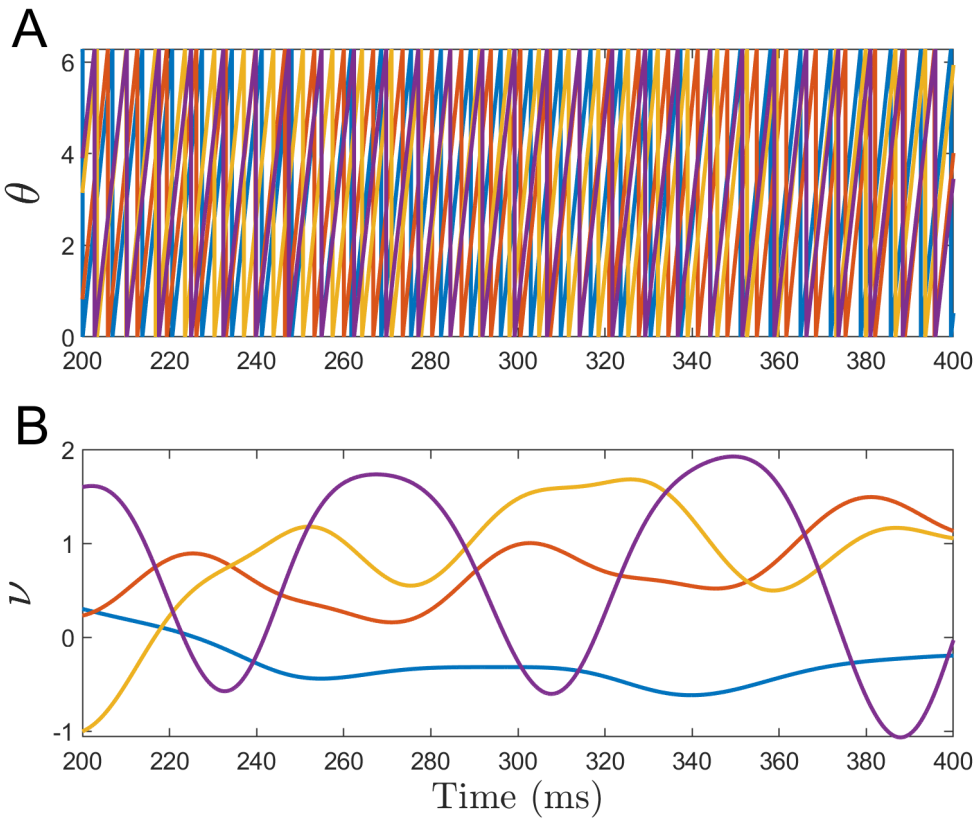

Figure 4.20: The phase and amplitude dynamics of the reduced order model. Panel A presents the phase dynamics of the four subnetworks and panel B presents the amplitude dynamics of the four subnetworks.

We compare the ground truth model with the reduced order model by again approximating identical initial conditions of the full order model in the phase space and evolving the reduced order model defined in Equation (4.18) forward in time. We present a comparison of the two simulations in Figure 4.21. For this comparison, we have mapped the reduced order model back to its comparable state in the full order model using the relationship $x = f(\theta, \nu)$.

For additional validation of the data-driven reduced order model in this application, we present Figure 4.22, which plots the normalized count of voltage values for each subnetwork in both the full and reduced order models. Along with this, we also computed the variance of the full and reduced order models for each subnetwork. For the first subnetwork, the variance is 145.6 in the full order model and 144.8 in the reduced order model. For the second subnetwork, the variance is 156.8 in

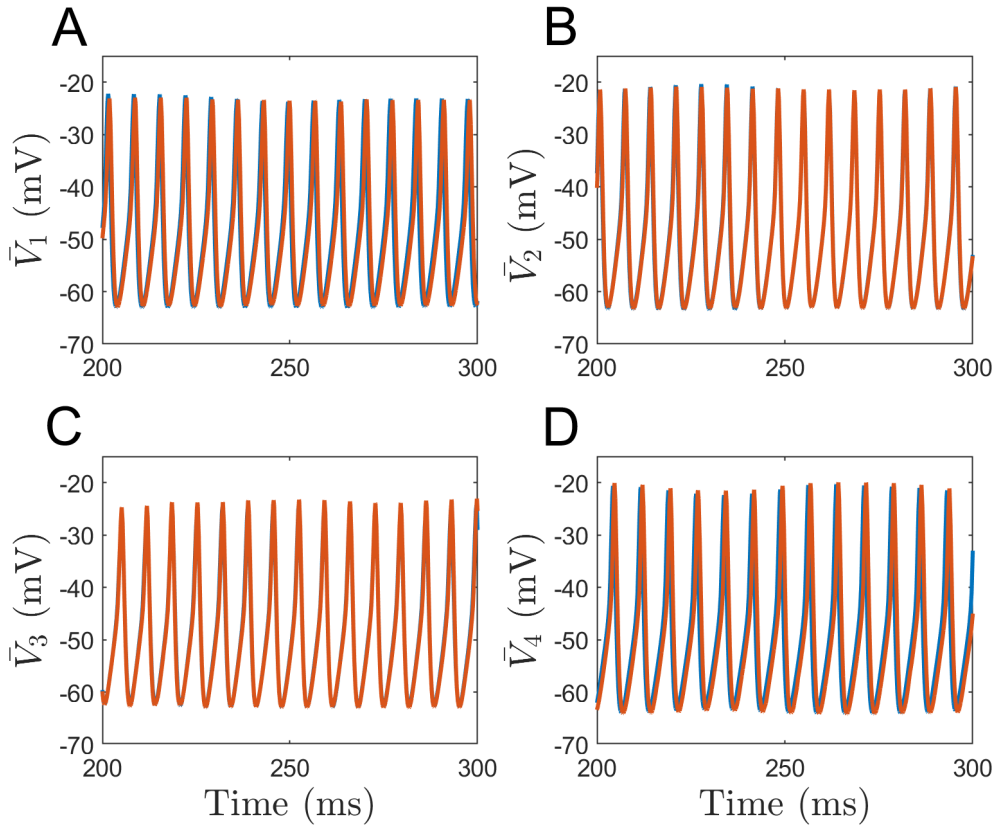

Figure 4.21: This figure compares the full order model with dynamics defined in Equations (B.1)-(B.5) in Appendix B to the comparable states inferred from the reduced order model defined in Equation (4.18). Panels A-D compare the dynamics of $\bar{V}_1 - \bar{V}_4$ in the full order model and reduced order model. In all panels, the state in the full order model is plotted in blue and the comparable state derived from the reduced order model is shown in red. The curves match closely and are nearly indistinguishable in all panels.

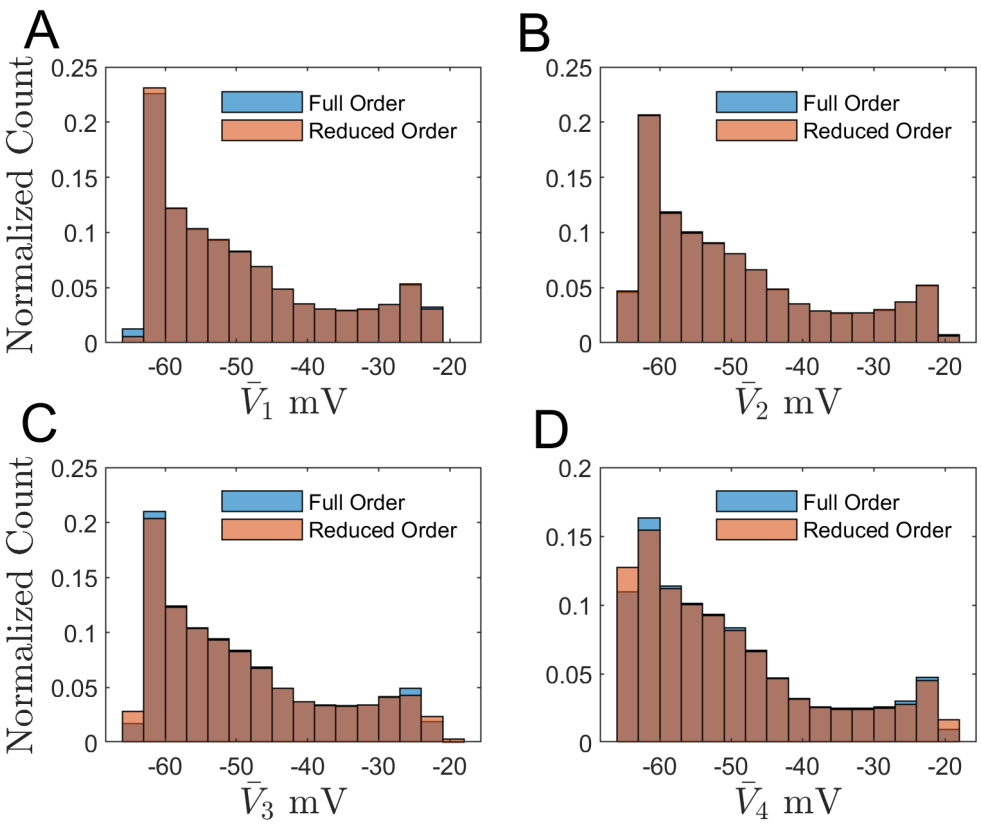

Figure 4.22: This figure presents the normalized count of $\bar{V}$ for the full and reduced order model. Panels A-D present the data for subnetworks 1-4, respectively.

the full order model and 156.4 in the reduced order model. For the third subnetwork, the variance is 139.1 in the full order model and 141.8 in the reduced order model. For the fourth subnetwork, the variance is 153.6 in the full order model and 157.9 in the reduced order model. Figure 4.22 along with the variances support the visual results presented in Figure 4.21, demonstrating again that the data-driven reduced order model yields a close approximation to the full order model.

4.8 Discussion and Conclusion

Phase-based model order reduction methods are frequently used to analyze high-dimensional, nonlinear dynamical systems that possess a stable limit cycle. Existing phase-based, data-driven model identification strategies assume the existence of a single, uncoupled limit cycle oscillator and cannot be straightforwardly implemented in applications where there are multiple coupled oscillators. In this work, we derive a data-driven phase-amplitude reduced order modeling technique

for a system of coupled limit cycle oscillators. We apply this technique in three examples: 1) a two oscillator model of the nonradial isochron clock with coupling; 2) a two subnetwork, 1000 neuron system with electrotonic and synaptic coupling; and 3) a four subnetwork, 1000 neuron system with electrotonic and synaptic coupling. Our results demonstrate that the reduced order model is a close match to the full order model for all three examples. We also demonstrate the similarity between the analytical coupling functions for our systems, and their numerical least-squares approximations.

The data-driven reduced order modeling technique implemented here incorporates the temporal dynamics intrinsic to the evaluated dynamical systems – specifically, the existence of stable, T-periodic limit cycles. Coupled limit cycle oscillators can be modeled with the modeling techniques described in this work if: 1) the underlying dynamical systems possess stable, T-periodic limit cycles; 2) the effects due to coupling, noise, and heterogeneity are relatively minimal with respect to the stable T-periodic limit cycle; and 3) measurements of the phase and amplitude coordinates can be taken over the entire range of possible phase differences.

Some of the specific limitations we encountered related to the coupling strength between limit cycle oscillators. Specifically, if the coupling strength was too strong, the oscillators possessed either strong synchronzing or antiphase tendencies. This made it impossible to derive a reduced-order model using this technique since ϕ did not generally extend over the entire range $[0, 2\pi]$ (related to point 3 in the above paragraph). Additionally, as we added more oscillators (or subnetworks), our accuracy degraded due to the high quantity of Fourier series terms that needed to be fit to the phase dynamics.

The model reduction strategies described in this paper are an adaptation of existing reduced order modeling techniques that consider a realistic scenario: a dynamical system whose structure and dynamics are mathematically unknown. In the future, we will consider extending these results by deriving the phase response curves and isostable response curves of more complicated networks of subnetworks (i.e., a 4 subnetwork system). Additionally, we will investigate the potential application of this technique to a system whose physical connections are unknown – that is, a system where we do not already know which neurons exist in the same subnetwork. We will consider extending our results to model control inputs using the reduced-order model.

Chapter 5

Conclusion and Final Remarks

In this work, we implement phase and phase-amplitude reduced order modeling techniques to analyze and control computational neural brain rhythms. The primary motivation behind this work was the desire to reflect biologically realistic neural behavior in computational settings, accounting for certain complexities often ignored in the phase-based model reduction of neural oscillators

In Chapter 2, we utilize adaptive phase-amplitude reduction to determine a control input with a slowly varying magnitude and phase offset capable of driving a pathologically synchronized population of neural oscillators towards a desynchronized state, mirroring the effect of aDBS on the pathologically synchronized neurons associated with Parkinsonian tremors. In Chapter 3, we implement phase reduction to determine the upper bound of the critical coupling strength required to retain phase cohesion in populations of excitatory neurons coupled with synaptic plasticity. In Chapter 4, we apply a direct method approach to derive a data-driven reduced order model for networks of oscillators with complex coupling structures and apply the derived algorithm to three different scenarios, focusing on its application in the analysis of population-level oscillations.

Future work will continue to explore the adaptation of phase-based reduced order modeling techniques to additional biologically realistic scenarios in computational neuroscience, with an end goal of uniting computational results with experimental data. In the near future, I hope to investigate further the possible application of the data-driven algorithm derived in Chapter 4 to real experimental data. One specific objective for my future research will include exploring methods to apply the data-driven reduced order model to networks of neuronal subnetworks where the subnetworks are not inherently known. The first step in this will be to determine properties

and methods that can be implemented to identify subnetworks of neurons and distinguish each subnetwork from the others.

The algorithms and approaches explored in Chapters 2 and 3 were published in Chaos [116] (2022) and the Journal of Mathematical Biology [117] (2024). A draft of the article containing the work presented in Chapter 4 is in preparation and will be submitted for publication shortly.

Bibliography

[1] Adamchic, I., Hauptmann, C., Barnikol, U. B., Pawelczyk, N., Popovych, O., Barnikol, T. T., Silchenko, A., Volkmann, J., Deuschl, G., Meissner, W. G., Maarouf, M., Sturm, V., Freund, H. J., and Tass, P. A. (2014). Coordinated reset neuromodulation for Parkinson's disease: proof-of-concept study. *Movement Disorders*, 29(13):1679–1684. 4

[2] Adrian, E. D. (1942). Olfactory reactions in the brain of the hedgehog. *The Journal of physiology*, 100(4):459. 84

[3] Ahmed, T., Sadovnik, A., and Wilson, D. (2023). Data-driven inference of low-order isostable-coordinate-based dynamical models using neural networks. *Nonlinear Dynamics*, 111(3):2501–2519. 68

[4] Aminzare, A., Holmes, P., and Srivastava, V. (2019). On phase reduction and time period of noisy oscillators. In *2019 IEEE 58th conference on decision and control*, pages 4717–4722. IEEE. 14

[5] Arachchige, A. S. P. M. (2023). The blue brain project: pioneering the frontier of brain simulation. *AIMS neuroscience*, 10(4):315. 1, 66

[6] Ashwin, P. and Swift, J. W. (1992). The dynamics of n weakly coupled identical oscillators. *Journal of Nonlinear Science*, 2:69–108. 49, 67

[7] Azodi-Avval, R. and Gharabaghi, A. (2015). Phase-dependent modulation as a novel approach for therapeutic brain stimulation. *Frontiers in Computational Neuroscience*, 9:26. 4, 38

[8] Benabid, A. L. (2003). Deep brain stimulation for parkinson's disease. *Current opinion in neurobiology*, 13(6):696–706. 1, 66

[9] Benabid, A. L., Chabardes, S., Mitrofanis, J., and Pollak, P. (2009). Deep brain stimulation of the subthalamic nucleus for the treatment of Parkinson's disease. *The Lancet Neurology*, 8(1):67–81. 1, 4

[10] Brown, E., Holmes, P., and Moehlis, J. (2003). Globally coupled oscillator networks. In *Perspectives and Problems in Nonlinear Science*, pages 183–215. Springer. 41

[11] Brown, E., Moehlis, J., and Holmes, P. (2004). On the phase reduction and response dynamics of neural oscillator populations. *Neural computation*, 16(4):673–715. 67, 84

[12] Brown, P. (2007). Abnormal oscillatory synchronisation in the motor system leads to impaired movement. *Current Opinion in Neurobiology*, 17(6):656–664. 1, 4, 7

[13] Brunton, S. L., Proctor, J. L., and Kutz, J. N. (2016). Discovering governing equations from data by sparse identification of nonlinear dynamical systems. *Proceedings of the national academy of sciences*, 113(15):3932–3937. 67

[14] Butson, C. R. and McIntyre, C. C. (2007). Differences among implanted pulse generator waveforms cause variations in the neural response to deep brain stimulation. *Clinical Neurophysiology*, 118(8):1889–1894. 36

[15] Cagnan, H., Pedrosa, D., Little, S., Pogosyan, A., Cheeran, B., Aziz, T., Green, A., Fitzgerald, J., Foltynie, T., Limousin, P., Zrinzo, L., Hariz, M., Friston, K. J., Denison, T., and Brown, P. (2017). Stimulating at the right time: phase-specific deep brain stimulation. *Brain*, 140(1):132–145. 2, 4, 37

[16] Castejón, O., Guillamon, A., and Huguet, G. (2013). Phase-amplitude response functions for transient-state stimuli. *The Journal of Mathematical Neuroscience*, 3:13. 10

[17] Chialvo, D. R. (2010). Emergent complex neural dynamics. *Nature Physics*, 6(10):744–750. 45

[18] Dayan, P. and Abbott, L. (2001). *Theoretical Neuroscience*. MIT Press, Cambridge. 44

[19] Duchet, B., Weerasinghe, G., Bick, C., and Bogacz, R. (2021). Optimizing deep brain stimulation based on isostable amplitude in essential tremor patient models. *Journal of Neural Engineering*, 18(4):046023. 5, 38

[20] Duchet, B., Weerasinghe, G., Cagnan, H., Brown, P., Bick, C., and Bogacz, R. (2020). Phase-dependence of response curves to deep brain stimulation and their relationship: from essential tremor patient data to a Wilson–Cowan model. *The Journal of Mathematical Neuroscience*, 10(1):1–39. 4

[21] Ermentrout, B. (1996). Type I membranes, phase resetting curves, and synchrony. *Neural Computation*, 8:979–1001. 41

[22] Ermentrout, G. B. and Terman, D. H. (2010). *Mathematical Foundations of Neuroscience*, volume 35. Springer, New York. 9, 41, 43, 48, 67

[23] Faramarzi, S. and Netoff, T. I. (2021). Closed-loop neuromodulation for clustering neuronal populations. *Journal of Neurophysiology*, 125(1):248–255. 4

[24] Gardiner, C. W. (2004). *Handbook of Stochastic Methods: for Physics, Chemistry and the Natural Sciences*. Springer, Berlin. 14

[25] Gengel, E., Teichmann, E., Rosenblum, M., and Pikovsky, A. (2020). High-order phase reduction for coupled oscillators. *Journal of Physics: Complexity*, 2(1):015005. 10

[26] Glass, L. and Mackey, M. C. (1988). *From clocks to chaos: The rhythms of life*. Princeton University Press. 67

[27] Golombek, D. A. and Rosenstein, R. E. (2010). Physiology of circadian entrainment. *Physiological Reviews*, 90(3):1063–1102. 41

[28] Gray, C. M. and Singer, W. (1989). Stimulus-specific neuronal oscillations in orientation columns of cat visual cortex. *Proceedings of the National Academy of Sciences*, 86(5):1698–1702. 84

[29] Green, J. D. and Arduini, A. A. (1954). Hippocampal electrical activity in arousal. *Journal of neurophysiology*, 17(6):533–557. 84

[30] Guckenheimer, J. (1975). Isochrons and phaseless sets. *Journal of Mathematical Biology*, 1(3):259–273. 10, 67

[31] Guckenheimer, J. and Holmes, P. (1983). *Nonlinear Oscillations, Dynamical Systems, and Bifurcations of Vector Fields*, volume 42. Springer Verlag, New York. 5, 18, 38, 71, 73

[32] Gütig, R., Aharonov, R., Rotter, S., and Sompolinsky, H. (2003). Learning input correlations through nonlinear temporally asymmetric hebbian plasticity. *Journal of Neuroscience*, 23(9):3697–3714. 65

[33] Hammond, C., Bergman, H., and Brown, P. (2007). Pathological synchronization in Parkinson's disease: networks, models and treatments. *Trends Neurosci.*, 30:357–64. 1, 4, 7

[34] Hansel, D., Mato, G., and Meunier, C. (1995). Synchrony in excitatory neural networks. *Neural Computation*, 7(2):307–337. 41

[35] Hemati, M. S., Rowley, C. W., Deem, E. A., and Cattafesta, L. N. (2017). De-biasing the dynamic mode decomposition for applied koopman spectral analysis of noisy datasets. *Theoretical and Computational Fluid Dynamics*, 31:349–368. 67

[36] Hipp, J. F. and Siegel, A. K. E. M. (2011). Oscillatory synchronization in large-scale cortical networks predicts perception. *Neuron*, 69(2):387–396. 41

[37] Ho, V. M., Lee, J., and Martin, K. C. (2011). The cell biology of synaptic plasticity. *Science (American Association for the Advancement of Science)*, 334(6056):623–628. 2, 41

[38] Holt, A. B., Kormann, E., Gulberti, A., Pötter-Nerger, M., McNamara, C. G., Cagnan, H., Baaske, M. K., Little, S., Köppen, J. A., Buhmann, C., Westphal, M., Gerloff, C., Engel, A. K., Brown, P., Hamel, W., Moll, C. K. E., and Sharott, A. (2019). Phase-dependent suppression of beta oscillations in Parkinson's disease patients. *Journal of Neuroscience*, 39(6):1119–1134. 2, 4, 37

[39] Holt, A. B., Wilson, D., Shinn, M., Moehlis, J., and Netoff, T. I. (2016). Phasic burst stimulation: a closed-loop approach to tuning deep brain stimulation parameters for parkinson's disease. *PLoS Computational Biology*, 12(7):e1005011. 4, 38, 41

[40] Hoppensteadt, F. C. and Izhikevich, E. M. (1997). *Weakly Connected Neural Networks*. Springer, New York. 41

[41] Hurtado, J. M., Gray, C. M., Tamas, L. B., and Sigvardt, K. A. (1999). Dynamics of tremor-related oscillations in the human globus pallidus: a single case study. *Proceedings of the National Academy of Sciences*, 96(4):1674–1679. 1, 66

[42] Iakymchuk, T., Rosado-Muñoz, A., Guerrero-Martínez, J. F., Bataller-Mompeán, M., and Francés-Víllora, J. V. (2015). Simplified spiking neural network architecture and STDP learning algorithm applied to image classification. *EURASIP Journal on Image and Video Processing*, 2015(1):1–11. 42

[43] Izhikevich, E. M. (2007). *Dynamical systems in neuroscience*. MIT press. 67

[44] Jasper, H. H. and Andrews, H. L. (1938). Electro-encephalography: Iii. normal differentiation of occipital and precentral regions in man. *Archives of Neurology & Psychiatry*, 39(1):96–115. 84

[45] Karbowski, J. and Ermentrout, G. B. (2002). Synchrony arising from a balanced synaptic plasticity in a network of heterogeneous neural oscillators. *Physical Review E*, 65(3):031902. 44, 50

[46] Kennedy, M. B. (2013). Synaptic signaling in learning and memory. *Cold Spring Harbor perspectives in biology*, 8(2):a016824–a016824. 2, 41

[47] Khoshkhou, M. and Montakhab, A. (2019). Spike-timing-dependent plasticity with axonal delay tunes networks of izhikevich neurons to the edge of synchronization transition with scale-free avalanches. *Frontiers in Systems Neuroscience*, 13. 2, 41, 44, 47

[48] Kopell, N. J., Gritton, H. J., Whittington, M. A., and Kramer, M. A. (2014). Beyond the connectome: the dynome. *Neuron*, 83(6):1319–1328. 1, 66

[49] Kühn, A. A., Tsui, A., Aziz, T., Ray, N., Brücke, C., Kupsch, A., Schneider, G. H., and Brown, P. (2009). Pathological synchronisation in the subthalamic nucleus of patients with Parkinson's disease relates to both bradykinesia and rigidity. *Experimental Neurology*, 215(2):380–387. 1, 4, 7

[50] Kuncel, A. M. and Grill, W. M. (2004). Selection of stimulus parameters for deep brain stimulation. *Clinical Neurophysiology*, 115(11):2431–2441. 4, 36

[51] Kuramoto, Y. (1984). *Chemical Oscillations, Waves, and Turbulence*. Springer-Verlag, Berlin. 14, 67

[52] Kutz, J. N., Brunton, S. L., Brunton, B. W., and Proctor, J. L. (2016). *Dynamic mode decomposition: data-driven modeling of complex systems*. SIAM. 67

[53] Kvalheim, M. D. and Revzen, S. (2021). Existence and uniqueness of global koopman eigenfunctions for stable fixed points and periodic orbits. *Physica D: Nonlinear Phenomena*, 425:132959. 69

[54] Lenz, F., Kwan, H., Martin, R., Tasker, R., Dostrovsky, J., and Lenz, Y. (1994). Single unit analysis of the human ventral thalamic nuclear group: tremor-related activity in functionally identified cells. *Brain*, 117(3):531–543. 1, 66

[55] Letson, B. and Rubin, J. E. (2020). LOR for analysis of periodic dynamics: A one-stop shop approach. *SIAM Journal on Applied Dynamical Systems*, 19(1):58–84. 10

[56] Levina, A., Herrmann, J. M., and Geisel, T. (2007). Dynamical synapses causing self-organized criticality in neural networks. *Nature Physics*, 3(12):857–860. 45

[57] Levy, N., Horn, D., Meilijson, I., and Ruppin, E. (2001). Distributed synchrony in a cell assembly of spiking neurons. *Neural Networks*, 14(6-7):815–824. 44

[58] Levy, R., Hutchison, W. D., Lozano, A. M., and Dostrovsky, J. O. (2000). High-frequency synchronization of neuronal activity in the subthalamic nucleus of parkinsonian patients with limb tremor. *Journal of Neuroscience*, 20(20):7766–7775. 1, 66

[59] Levy, R., Hutchison, W. D., Lozano, A. M., and Dostrovsky, J. O. (2002). Synchronized neuronal discharge in the basal ganglia of parkinsonian patients is limited to oscillatory activity. *Journal of Neuroscience*, 22(7):2855–2861. 1, 4, 7

[60] Li, M. C. H. and Cook, M. J. (2018). Deep brain stimulation for drug-resistant epilepsy. *Epilepsia*, 59(2):273–290. 1, 4

[61] Linot, A. J. and Graham, M. D. (2020). Deep learning to discover and predict dynamics on an inertial manifold. *Physical Review E*, 101(6):062209. 68

[62] Ly, C. and Ermentrout, G. B. (2009). Synchronization dynamics of two coupled neural oscillators receiving shared and unshared noisy stimuli. *Journal of Computational Neuroscience*, 26(3):425–443. 14

[63] Maistrenko, Y. L., Lysyansky, B., Hauptmann, C., Burylko, O., and Tass, P. A. (2007). Multistability in the kuramoto model with synaptic plasticity. *Physical Review E*, 75(6):066207. 44

[64] Malekmohammadi, M., Herron, J., Velisar, A., Blumenfeld, Z., Trager, M. H., Chizeck, H. J., and Brontë-Stewart, H. (2016). Kinematic adaptive deep brain stimulation for resting tremor in parkinson's disease. *Movement Dfisorders*, 31(3):426–428. 5

[65] Mangan, N. M., Askham, T., Brunton, S. L., Kutz, J. N., and Proctor, J. L. (2019). Model selection for hybrid dynamical systems via sparse regression. *Proceedings of the Royal Society A*, 475(2223):20180534. 67

[66] Manna, D. L., Vicente-Sola, A., Kirkland, P., Bihl, T. J., and Di Caterina, G. (2022). Simple and complex spiking neurons: Perspectives and analysis in a simple STDP scenario. *Neuromorphic Computing and Engineering*, 2(4):044009. 42

[67] Manos, T., Zeitler, M., and Tass, P. A. (2018). How stimulation frequency and intensity impact on the long-lasting effects of coordinated reset stimulation. *PLoS Computational Biology*, 14(5):e1006113. 4

[68] Matchen, T. D. and Moehlis, J. (2018). Phase model-based neuron stabilization into arbitrary clusters. *Journal of Computational Neuroscience*, 44(3):363–378. 4

[69] Mauroy, A., Mezić, I., and Moehlis, J. (2013). Isostables, isochrons, and Koopman spectrum for the action–angle representation of stable fixed point dynamics. *Physica D: Nonlinear Phenomena*, 261:19–30. 10, 69

[70] Mayberg, H. S., Lozano, A. M., Voon, V., McNeely, H. E., Seminowicz, D., Hamani, C., Schwalb, J. M., and Kennedy, S. H. (2005). Deep brain stimulation for treatment-resistant depression. *Neuron*, 45(5):651–660. 1, 4, 66

[71] Meidahl, A. C., Tinkhauser, G., Herz, D. M., Cagnan, H., Debarros, J., and Brown, P. (2017). Adaptive deep brain stimulation for movement disorders: the long road to clinical therapy. *Movement Disorders*, 32(6):810–819. 2, 4

[72] Merill, D., Bikson, M., and Jefferys, J. (2005). Electrical stimulation of excitable tissue: design of efficacious and safe protocols. *J. Neurosci Methods*, 141(2):171–198. 36

[73] Modolo, J., Legros, A., Thomas, A. W., and Beuter, A. (2011). Model-driven therapeutic treatment of neurological disorders: reshaping brain rhythms with neuromodulation. *Interface focus*, 1(1):61–74. 1, 66

[74] Monga, B. and Moehlis, J. (2019). Phase distribution control of a population of oscillators. *Physica D: Nonlinear Phenomena*, 398:115–129. 4

[75] Monga, B., Wilson, D., Matchen, T., and Moehlis, J. (2019). Phase reduction and phase-based optimal control for biological systems: A tutorial. *Biological Cybernetics*, 113(1):11–46. 11, 48, 49, 67, 83

[76] Nabi, A., Mirzadeh, M., Gibou, F., and Moehlis, J. (2013). Minimum energy desynchronizing control for coupled neurons. *Journal of Computational Neuroscience*, 34:259–271. 4

[77] Nakao, H. (2016). Phase reduction approach to synchronisation of nonlinear oscillators. *Contemporary Physics*, 57(2):188–214. 67

[78] Netoff, T., Schwemmer, M. A., and Lewis, T. J. (2012). Experimentally estimating phase response curves of neurons: theoretical and practical issues. *Phase Response Curves in Neuroscience: Theory, Experiment, and Analysis*, pages 95–129. 67

[79] Nowotny, T., Zhigulin, V. P., Selverston, A. I., Abarbanel, H. D. I., and Rabinovich, M. I. (2003). Enhancement of synchronization in a hybrid neural circuit by spike-timing dependent plasticity. *Journal of Neuroscience*, 23(30):9776–9785. 44

[80] O'Keefe, J. and Dostrovsky, J. (1971). The hippocampus as a spatial map: preliminary evidence from unit activity in the freely-moving rat. *Brain research*. 84

[81] Ozkan, Z. A., Bose, A., and Nadim, F. (2014). Effects of synaptic plasticity on phase and period locking in a network of two oscillatory neurons. *Journal of Mathematical Neuroscience*, 4:8. 44

[82] Panda, P., Allred, J. M., Ramanathan, S., and Roy, K. (2018). ASP: Learning to forget with adaptive synaptic plasticity in spiking neural networks. *IEEE Journal on Emerging and Selected Topics in Circuits and Systems*, 8(1):51–64. 48

[83] Pathak, J., Hunt, B., Girvan, M., Lu, Z., and Ott, E. (2018). Model-free prediction of large spatiotemporally chaotic systems from data: A reservoir computing approach. *Physical review letters*, 120(2):024102. 68

[84] Perlmutter, J. S. and Mink, J. W. (2006). Deep brain stimulation. *Annual Reviews of Neuroscience*, 29:229–257. 1, 4

[85] Pietras, B. and Daffertshofer, A. (2019). Network dynamics of coupled oscillators and phase reduction techniques. *Physics Reports*. 9, 67

[86] Pogosyan, A., Yoshida, F., Chen, C., Martinez-Torres, I., Foltynie, T., Limousin, P., Zrinzo, L., Hariz, M., and Brown, P. (2010). Parkinsonian impairment correlates with spatially extensive subthalamic oscillatory synchronization. *Neuroscience*, 171(1):245–257. 41

[87] Popovych, O., Hauptmann, C., and Tass, P. (2005). Effective desynchronization by nonlinear delayed feedback. *Physical review letters*, 94(16):164102. 5, 38

[88] Popovych, O. V., Hauptmann, C., and Tass, P. A. (2006). Control of neuronal synchrony by nonlinear delayed feedback. *Biological Cybernetics*, 95(1). 38

[89] Popovych, O. V., Lysyansky, B., Rosenblum, M., Pikovsky, A., and Tass, P. A. (2017a). Pulsatile desynchronizing delayed feedback for closed-loop deep brain stimulation. *PloS One*, 12(3):e0173363. 5, 38

[90] Popovych, O. V., Lysyansky, B., and Tass, P. A. (2017b). Closed-loop deep brain stimulation by pulsatile delayed feedback with increased gap between pulse phases. *Scientific Reports*, 7(1):1–14. 5

[91] Popovych, O. V. and Tass, P. A. (2019). Adaptive delivery of continuous and delayed feedback deep brain stimulation-a computational study. *Scientific Reports*, 9(1):1–17. 5

[92] Priori, A., Foffani, G., Rossi, L., and Marceglia, S. (2013). Adaptive deep brain stimulation (aDBS) controlled by local field potential oscillations. *Experimental Neurology*, 245:77–86. 2, 4

[93] Proctor, J. L., Brunton, S. L., and Kutz, J. N. (2016). Dynamic mode decomposition with control. *SIAM Journal on Applied Dynamical Systems*, 15(1):142–161. 67

[94] Pyragas, K., Fedaravičius, A. P., Pyragienė, T., and Tass, P. A. (2018). Optimal waveform for entrainment of a spiking neuron with minimum stimulating charge. *Physical Review E*, 98(4):042216. 41

[95] Raissi, M. (2018). Deep hidden physics models: Deep learning of nonlinear partial differential equations. *Journal of Machine Learning Research*, 19(25):1–24. 68

[96] Reis, C., Arruda, B. S., Pogosyan, A., Brown, P., and Cagnan, H. (2021). Essential tremor amplitude modulation by median nerve stimulation. *Scientific Reports*, 11(1):1–10. 38

[97] Reppert, S. M. and Weaver, D. R. (2002). Coordination of circadian timing in mammals. *Nature*, 418(6901):935. 41

[98] Rosa, M., Arlotti, M., Ardolino, G., Cogiamanian, F., Marceglia, S., Fonzo, A. D., Cortese, F., Rampini, P. M., and Priori, A. (2015). Adaptive deep brain stimulation in a freely moving Parkinsonian patient. *Movement Disorders*, 30(7):1003–1005. 2, 4, 5

[99] Rosenblum, M. and Pikovsky, A. (2004). Controlling synchronization in an ensemble of globally coupled oscillators. *Physical Review Letters*, 92(11):114102. 5, 38

[100] Rosenblum, M. and Pikovsky, A. (2019). Numerical phase reduction beyond the first order approximation. *Chaos: An Interdisciplinary Journal of Nonlinear Science*, 29(1):011105. 10

[101] Rosin, B., Slovik, M., Mitelman, R., Rivlin-Etzion, M., Haber, S. N., Israel, Z., Vaadia, E., and Bergman, H. (2011). Closed-loop deep brain stimulation is superior in ameliorating parkinsonism. *Neuron*, 72(2):370–384. 2, 4, 37

[102] Rowley, C. W., Mezić, I., Bagheri, S., Schlatter, P., and Henningson, D. S. (2009). Spectral analysis of nonlinear flows. *Journal of fluid mechanics*, 641:115–127. 67

[103] Rubin, J. and Terman, D. (2004). High frequency stimulation of the subthalamic nucleus eliminates pathological thalamic rhythmicity in a computational model. *Journal of Computational Neuroscience*, 16:211–235. 7, 46, 116, 118

[104] Salanova, V. (2018). Deep brain stimulation for epilepsy. *Epilepsy & Behavior*, 88:21–24. 1, 66

[105] Sanders, J. A., Verhulst, F., and Murdock, J. (2007). *Averaging Methods in Nonlinear Dynamical Systems*. Springer-Verlag, New York, second edition. 5, 18, 38, 56, 71, 73

[106] Schmid, P. J. (2010). Dynamic mode decomposition of numerical and experimental data. *Journal of fluid mechanics*, 656:5–28. 67

[107] Schöll, E., Hiller, G., Hövel, P., and Dahlem, M. A. (2009). Time-delayed feedback in neurosystems. *Philosophical Transactions of the Royal Society A: Mathematical, Physical and Engineering Sciences*, 367(1891):1079–1096. 38

[108] Schrock, L. E., Mink, J. W., Woods, D. W., Porta, M., Servello, D., Visser-Vandewalle, V., Silburn, P. A., Foltynie, T., Walker, H. C., Shahed-Jimenez, J., Savica, R., Klassen, B. T., Machado, A. G., Foote, K. D., Zhang, J. G., Hu, W., Ackermans, L., Temel, Y., Mari, Z., Changzi, B. K., Lozano, A., Auyeung, M., Kaido, T., Agid, Y., Welter, M. L., Khandhar, S. M., Mogilner, A. Y., Pourfar, M. H., Walter, B. L., Juncos, J. L., Gross, R. E., Kuhn, J., Leckma, J. F., Neimat, J. A., and Okun, M. S. (2015). Tourette syndrome deep brain stimulation: a review and updated recommendations. *Movement Disorders*, 30(4):448–471. 4

[109] Schwabedal, J. T. C. and Pikovsky, A. (2013). Phase description of stochastic oscillations. *Physical Review Letters*, 110(20):204102. 14

[110] Senkowski, D., Schneider, T. R., Foxe, J. J., and Engel, A. K. (2008). Crossmodal binding through neural coherence: implications for multisensory processing. *Trends in Neurosciences*, 31(8):401–409. 41

[111] Shirasaka, S., Kurebayashi, W., and Nakao, H. (2017). Phase-amplitude reduction of transient dynamics far from attractors for limit-cycling systems. *Chaos: An Interdisciplinary Journal of Nonlinear Science*, 27(2):023119. 10

[112] Smit, J. V., Janssen, M. L. F., Schulze, H., Jahanshahi, A., Overbeeke, J. J. V., Temel, Y., and Stokroos, R. J. (2015). Deep brain stimulation in tinnitus: current and future perspectives. *Brain Research*, 1608:51–65. 4

[113] Tass, P. A. (2003). A model of desynchronizing deep brain stimulation with a demand-controlled coordinated reset of neural subpopulations. *Biological Cybernetics*, 89(2):81–88. 4

[114] Thomas, P. J. and Lindner, B. (2014). Asymptotic phase for stochastic oscillators. *Physical Review Letters*, 113(25):254101. 14

[115] Timmermann, L., Gross, J., Dirks, M., Volkmann, J., Freund, H.-J., and Schnitzler, A. (2002). The cerebral oscillatory network of parkinsonian resting tremor. *Brain*, 126(1):199–212. 1, 66

[116] Toth, K. and Wilson, D. (2022). Control of coupled neural oscillations using near-periodic inputs. *Chaos: An Interdisciplinary Journal of Nonlinear Science*, 32(3). vi, 3, 41, 67, 101

[117] Toth, K. and Wilson, D. (2024). The influence of synaptic plasticity on critical coupling estimates for neural populations. *Journal of Mathematical Biology*, 88(3):39. vi, 41, 101

[118] Van Rossum, M. C. W., Shippi, M., and Barrett, A. B. (2012). Soft-bound synaptic plasticity increases storage capacity. *PLoS computational biology*, 8(12):e1002836. 43, 65

[119] Vercueil, L., Pollak, P., Fraix, V., Caputo, E., Moro, E., Benazzouz, A., Xie, J., Koudsie, A., and Benabid, A.-L. (2001). Deep brain stimulation in the treatment of severe dystonia. *Journal of neurology*, 248:695–700. 1, 66

[120] Volkmann, J., Herzog, J., Kopper, F., and Deuschl, G. (2002). Introduction to the programming of deep brain stimulators. *Movement Disorders*, 17(S3):S181–S187. 4

[121] Vreeswijk, C. V., Abbott, L. F., and Ermentrout, G. B. (1994). When inhibition not excitation synchronizes neural firing. *Journal of Computational Neuroscience*, 1(4):313–321. 41

[122] Vu, M., Singhal, B., Zeng, S., and Li, J.-S. (2024). Data-driven control of oscillator networks with population-level measurement. *Chaos: An Interdisciplinary Journal of Nonlinear Science*, 34(3). 84

[123] Wallace, E., Benayoun, M., Van Drongelen, W., and Cowan, J. D. (2011). Emergent oscillations in networks of stochastic spiking neurons. *Plos one*, 6(5):e14804. 84

[124] Wang, J., Nebeck, S., Muralidharan, A., Johnson, M. D., Vitek, J. L., and Baker, K. B. (2016). Coordinated reset deep brain stimulation of subthalamic nucleus produces long-lasting, dose-dependent motor improvements in the 1-methyl-4-phenyl-1, 2, 3, 6-tetrahydropyridine non-human primate model of parkinsonism. *Brain Stimulation*, 9(4):609–617. 4

[125] Wang, Z., Xiao, D., Fang, F., Govindan, R., Pain, C. C., and Guo, Y. (2018). Model identification of reduced order fluid dynamics systems using deep learning. *International Journal for Numerical Methods in Fluids*, 86(4):255–268. 68

[126] Wedgwood, K. C. A., Lin, K. K., Thul, R., and Coombes, S. (2013). Phase-amplitude descriptions of neural oscillator models. *The Journal of Mathematical Neuroscience*, 3(1):2. 10

[127] Weerasinghe, G., Duchet, B., Bick, C., and Bogacz, R. (2021). Optimal closed-loop deep brain stimulation using multiple independently controlled contacts. *PLoS Computational Biology*, 17(8):e1009281. 5, 38

[128] Weerasinghe, G., Duchet, B., Cagnan, H., Brown, P., Bick, C., and Bogacz, R. (2019). Predicting the effects of deep brain stimulation using a reduced coupled oscillator model. *PLoS computational biology*, 15(8):e1006575. 5, 38

[129] Whittington, M. A., Traub, R. D., and Adams, N. E. (2018). A future for neuronal oscillation research. *Brain and Neuroscience Advances*, 2:2398212818794827. 84

[130] Whittington, M. A., Traub, R. D., and Jefferys, J. G. (1995). Synchronized oscillations in interneuron networks driven by metabotropic glutamate receptor activation. *Nature*, 373(6515):612–615. 84

[131] Wichmann, T., DeLong, M. R., Guridi, J., and Obeso, J. A. (2011). Milestones in research on the pathophysiology of parkinson's disease. *Movement Disorders*, 26(6):1032–1041. 41

[132] Wilson, C., Beverlin II, B., and Netoff, T. (2011). Chaotic desynchronization as the therapeutic mechanism of deep brain stimulation. *Frontiers in Systems Neuroscience*, 5:Art. No. 50. 4

[133] Wilson, D. (2020a). A data-driven phase and isostable reduced modeling framework for oscillatory dynamical systems. *Chaos: An Interdisciplinary Journal of Nonlinear Science*, 30(1). 68

[134] Wilson, D. (2020b). Optimal open-loop desynchronization of neural oscillator populations. *Journal of Mathematical Biology*, 81(1):25–64. 41, 67

[135] Wilson, D. (2020c). Phase-amplitude reduction far beyond the weakly perturbed paradigm. *Physical Review E*, 101(2):022220. 10

[136] Wilson, D. (2021a). Degenerate isostable reduction for fixed-point and limit-cycle attractors with defective linearizations. *Physical Review E*, 103(2):022211. 11

[137] Wilson, D. (2021b). Optimal control of oscillation timing and entrainment using large magnitude inputs: An adaptive phase-amplitude-coordinate-based approach. *SIAM Journal on Applied Dynamical Systems*, 20(4):1814–1843. 5, 11, 38

[138] Wilson, D. (2022). An adaptive phase-amplitude reduction framework without $\mathcal{O}(\epsilon)$ constraints on inputs. *SIAM Journal on Applied Dynamical Systems*, 21(1):204–230. 5, 11, 12, 13, 38

[139] Wilson, D. (2023). A direct method approach for data-driven inference of high accuracy adaptive phase-isostable reduced order models. *Physica D: Nonlinear Phenomena*, 446:133675. 68

[140] Wilson, D. and Ermentrout, B. (2018). Greater accuracy and broadened applicability of phase reduction using isostable coordinates. *Journal of Mathematical Biology*, 76(1-2):37–66. 10

[141] Wilson, D. and Ermentrout, B. (2019). Augmented phase reduction of (not so) weakly perturbed coupled oscillators. *SIAM Review*, 61(2):277–315. 11

[142] Wilson, D., Faramarzi, S., Moehlis, J., Tinsley, M. R., and Showalter, K. (2018). Synchronization of heterogenous oscillator populations in response to weak and strong coupling. *Chaos: An Interdisciplinary Journal of Nonlinear Science*, 28(123114). 45, 58, 60, 64

[143] Wilson, D. and Moehlis, J. (2014). Optimal chaotic desynchronization for neural populations. *SIAM Journal on Applied Dynamical Systems*, 13(1):276–305. 4

[144] Wilson, D. and Moehlis, J. (2015). Clustered desynchronization from high-frequency deep brain stimulation. *PLoS Computational Biology*, 11(12):e1004673. 4

[145] Wilson, D. and Moehlis, J. (2016). Isostable reduction of periodic orbits. *Physical Review E*, 94(5):052213. 10, 11, 67, 69

[146] Wilson, D. and Moehlis, J. (2022). Recent advances in the analysis and control of large populations of neural oscillators. *Annual Reviews in Control*, 54:327–351. 49

[147] Winfree, A. (2001). *The Geometry of Biological Time*. Springer Verlag, New York, second edition. 9, 10, 67, 78

[148] Winfree, A. T. (1974). Patterns of phase compromise in biological cycles. *Journal of Mathematical Biology*, 1(1):73–93. 67

[149] Woolrich, M. W. and Stephan, K. E. (2013). Biophysical network models and the human connectome. *Neuroimage*, 80:330–338. 66

Appendices

A The General Thalamic Neural Model

In order to model the ionic currents I_{ion} for the population of neurons described by Equation (2.1), a three-dimensional model that replicates the behavior of tonically firing thalamic neurons from [103] is used. The model equations in the absence of coupling, noise, and external stimulus are:

$$\begin{aligned} C\dot{V} &= -I_{\text{ion}}(V,h,r), \\ \dot{h} &= \frac{h_\infty - h}{\tau_h}, \\ \dot{r} &= \frac{r_\infty - r}{\tau_r}, \end{aligned} \tag{A.1}$$

where $I_{\text{ion}}(V,r,h)$ is comprised of five ionic currents

$$I_{\text{ion}} = I_L(V) + I_{Na}(V,h) + I_K(V,h) + I_T(V,r) - I_b, \tag{A.2}$$

each given by

$$\begin{aligned} I_L(V) &= g_L(V - E_L), \\ I_{Na}(V,h) &= g_{Na}({m_\infty}^3)h(V - E_{Na}), \\ I_K(V,h) &= g_K((0.75(1-h))^4)(V - E_K), \\ I_T(V,r) &= g_T(p_\infty^2)r(V - E_T), \\ I_b &= 5\mu\text{A/cm}^2. \end{aligned} \tag{A.3}$$

Auxiliary functions are given below:

$$
\begin{aligned}
h_\infty &= 1/(1+\exp((V+41)/4)),\\
r_\infty &= 1/(1+\exp((V+84)/4)),\\
\alpha_h &= 0.128\exp(-(V+46)/18),\\
\beta_h &= 4/(1+\exp(-(V+23)/5)),\\
\tau_h &= 1/(\alpha_h+\beta_h),\\
\tau_r &= (28+\exp(-(V+25)/10.5)),\\
m_\infty &= 1/(1+\exp(-(V+37)/7)),\\
p_\infty &= 1/(1+\exp(-(V+60)/6.2)).
\end{aligned}
\tag{A.4}
$$

Additional constants are $C = 1\ \mu\text{F/cm}^2, g_L = 0.05\ \text{mS/cm}^2, E_L = -70\ \text{mV}, g_{Na} = 3\ \text{mS/cm}^2, E_{Na} = 50\ \text{mV}, g_K = 5\ \text{mS/cm}^2, E_K = -90\ \text{mV}, g_T = 5\ \text{mS/cm}^2, E_T = 0\ \text{mV}$. With these specific parameters, the neuron settles to a tonically firing limit cycle in steady state with a period of 8.40 ms.

B The Thalamic Neural Model for a Neuronal Network of Subnetworks

A single conductance-based thalamic neuron in the network model considered in Sections 4.6 and 4.7 has dynamics from [103].

$$\begin{aligned}
\frac{\dot{V_i}}{C} &= I_{b_i} - I_L(V_i) - I_{Na}(V_i, h_i) - I_K(V_i, h_i) - I_T(V_i, r_i) + I_{c_i} + \sqrt{2D}\eta_i(t) \\
\dot{h_i} &= (h_\infty - h_i)/\tau_h, \\
\dot{r_i} &= (r_\infty - r_i)/\tau_r, \\
i &= 1, ..., N,
\end{aligned} \tag{B.1}$$

where $C = 1\ \mu\text{F/cm}^2$ is the constant membrane capacitance; $N = 1000$ is the total number of neurons in the network of subnetworks; I_{b_i} is an external baseline stimulus; I_{c_i} is the current due to coupling; I_L, I_{Na}, I_K, and I_T are the leak, sodium, potassium, and low-threshold calcium ionic currents; $\eta_i(t)$ is a zero-mean white noise process with intensity D; and h_i and r_i are gating variables. The equations defining the ionic currents are defined below:

$$\begin{aligned}
I_L(V_i) &= g_L(V_i - E_L), \\
I_{Na}(V_i, h_i) &= g_{Na}(m_\infty^3)h_i(V_i - E_{Na}), \\
I_K(V_i, h_i) &= g_K(0.75(1 - h_i)^4)(V_i - E_K), \\
I_T(V_i, r_i) &= g_T(p_\infty^2)r_i(V_i - E_T).
\end{aligned} \tag{B.2}$$

In Equation (B.2), $g_L = 0.05\ \text{mS/cm}^2$, $E_L = -70\ \text{mV}$, $g_{Na} = 3\ \text{mS/cm}^2$, $E_{Na} = 50\ \text{mV}$, $g_K = 5\ \text{mS/cm}^2$, $E_K = -90\ \text{mV}$, $g_T = 5\ \text{mS/cm}^2$, and $E_T = 0\ \text{mV}$. Additional auxiliary variables are

$$
\begin{aligned}
h_\infty &= 1/(1+\exp((V+41)/4)), \\
r_\infty &= 1/(1+\exp((V+84)/4)), \\
\alpha_h &= 0.128\exp(-(V+46)/18), \\
\beta_h &= 4/(1+\exp(-(V+23)/5)), \\
\tau_h &= 1/(\alpha_h+\beta_h), \\
\tau_r &= 28+\exp(-(V+25)/10.5), \\
m_\infty &= 1/(1+\exp(-(V+37)/7)), \\
p_\infty &= 1/(1+\exp(-(V+60)/6.2)).
\end{aligned}
\tag{B.3}
$$

The coupling structure between neurons is complex. Neuron i is coupled with electrotonic coupling to all neurons within the same subnetwork as neuron i and with synaptic coupling to all other neurons not in the same subnetwork as neuron i. The current due to coupling I_{c_i} is

$$
I_{c_i} = \frac{1}{N-1}\Bigg[\underbrace{\sum_{j\neq i} K_{j\to i}(V_j - V_i)}_{\text{Electrotonic Current, Same Subnetwork}} - \underbrace{\sum_{j\neq i} g_{j\to i} s_j \big(V_i - E_{syn}(j,i)\big)}_{\text{Synaptic Current, Other Subnetworks}} \Bigg], \tag{B.4}
$$

where $g_{j\to i}$ is the synaptic coupling strength between neurons i and j, $K_{j\to i}$ is the electrotonic coupling strength between neurons i and j, $E_{syn}(j,i)$ (in mV) is the synaptic reversal potential between neurons i and j, and s_j is the synaptic variable with associated temporal dynamics

$$
\dot{s}_i = \frac{c_1(1-s_i)}{1+\exp(-(V_i - V_T)/\sigma_T)} - c_2 s_i. \tag{B.5}
$$

The synaptic variable has parameters $c_1 = 3$ (unitless), $c_2 = 1$ (unitless),$V_T = -20$ mV, and $\sigma_T = 0.8$ mV. The synaptic coupling strength $g_{j\to i}$, the synaptic reversal potential $E_{syn}(j,i)$, and the electrotonic coupling strength $K_{j\to i}$ are dependent on the subnetworks containing neurons i and j. For specific details regarding the parameters used in Sections 4.6 and 4.7 of this work, see the subsections below.

B.1 Parameters for the Neuronal Network of Two Subnetworks

For the two subnetwork system in Section 4.6, $N = 1000$ neurons with 500 neurons in each subnetwork. Both subnetworks are heterogeneous, with baseline stimuli $I_{b_i} \in [4.5, 4.7]$ μA/cm^2 for the first subnetwork and $I_{b_i} \in [5.5, 5.7]$ μA/cm^2 for the second subnetwork, both drawn from a uniform distribution. The noise intensity is $D = 0.0015$. The synaptic reversal potential between the subnetworks is $E_{syn} = -100$ mV.

The synaptic coupling strength between any two neurons, i and j will depend on the subnetworks containing the neurons i and j. Specifically, if $1 \leq i \leq 500$ and $500 < j \leq 1000$ or if $1 \leq j \leq 500$ and $500 < i \leq 1000$, then $g_{j\to i} = g_{i\to j} = 0.0501$. However, if $1 \leq i \leq 500$ and $1 \leq j \leq 500$ or $500 < i \leq 1000$ and $500 < j \leq 1000$, then $g_{j\to i} = g_{i\to j} = 0$.

The electrotonic coupling strength between any two neurons i and j is the same for all neurons within that subnetwork. Specifically, if $1 \leq i \leq 500$ and $1 \leq j \leq 500$, then $K_{j\to i} = K_{i\to j} = 0.1501$. If $500 < i \leq 1000$ and $500 < j \leq 1000$, then $K_{j\to i} = K_{i\to j} = 0.1782$. However, if $1 \leq i \leq 500$ and $500 < j \leq 1000$ or if $1 \leq j \leq 500$ and $500 < i \leq 1000$, then $K_{j\to i}$ does not exist.

B.2 Parameters for the Neuronal Network of Four Subnetworks

For the four subnetwork system in Section 4.7, N=1000 neurons with 250 neurons in each subnetwork. The subnetworks are heterogeneous, with baseline stimuli $I_{b_i} \in [4.0, 4.8]$ μA/cm^2 for the first subnetwork, $I_{b_i} \in [4.8, 5.6]$ μA/cm^2 for the second subnetwork, $I_{b_i} \in [5.6, 6.4]$ μA/cm^2 for the third subnetwork, and $I_{b_i} \in [6.4, 7.2]$ μA/cm^2 for the fourth subnetwork, each drawn from a uniform distribution. Here, the noise intensity is taken to be $D = 0.0016$. The synaptic reversal potential between the neurons i and j is $E_{syn}(i, j) = E_{syn}(j, i)$ and can be found by referencing Table 1. Note that neurons in the same subnetwork are not synaptically coupled.

Table 1: Table of synaptic reversal potentials between the four 250 neuron subnetworks analyzed in Section 4.7. $E_{syn}(j, i) = 0$ mV yields an excitatory connection and $E_{syn}(j, i) = -100$ mV yields an inhibitory connection.

	$1 \leq i \leq 250$	$250 < i \leq 500$	$500 < i \leq 750$	$750 < i \leq 1000$
$1 \leq j \leq 250$	–	-100	0	-100
$250 < j \leq 500$	-100	–	0	0
$500 < j \leq 750$	0	0	–	-100
$750 < j \leq 1000$	-100	0	-100	–

The synaptic coupling strength between any two neurons i and j again depends on the specific subnetworks containing neurons i and j. Note again that there is no synaptic coupling strength between neurons within the same subnetwork since these neurons are coupled electrotonically. Table 2 lists the synaptic coupling strength between neurons in the four subnetworks represented in Section 4.7.

The electrotonic coupling strength between any two neurons i and j only exists if i and j reside within the same subnetwork, and is identical for all neurons in that subnetwork. Table 3 lists the electrotonic coupling strengths for the four subnetwork system in Section 4.7.

Table 2: Table of synaptic coupling strengths between the four 250 neuron subnetworks analyzed in Section 4.7.

	$1 \leq i \leq 250$	$250 < i \leq 500$	$500 < i \leq 750$	$750 < i \leq 1000$
$1 \leq j \leq 250$	0	0.0101	0.0495	0.0235
$250 < j \leq 500$	0.0101	0	0.0667	0.0509
$500 < j \leq 750$	0.0495	0.0667	0	0.0436
$750 < j \leq 1000$	0.0235	0.0509	0.0436	0

Table 3: Table of electrotonic coupling strengths $K_{j\to i}$ between any two neurons i and j for the four 250 neuron subnetworks analyzed in Section 4.7.

	$1 \leq i \leq 250$	$250 < i \leq 500$	$500 < i \leq 750$	$750 < i \leq 1000$
$1 \leq j \leq 250$	0.1500	0	0	0
$250 < j \leq 500$	0	0.1669	0	0
$500 < j \leq 750$	0	0	0.1558	0
$750 < j \leq 1000$	0	0	0	0.1743

Vita

Kaitlyn Toth grew up in Silver Spring, MD where she was a successful competitive swimmer and a student with a proclivity for science and math. After graduating from high school, Kaitlyn received an appointment to the United States Coast Guard Academy in New London, CT. Kaitlyn received her B.S. in electrical engineering from the United States Coast Guard Academy in 2017. After serving on active duty in the U.S. Coast Guard for 2.5 years, Kaitlyn was medically retired and relocated to Knoxville, TN. Upon retiring from the U.S.Coast Guard, Kaitlyn began the pursuit of her Ph.D. in electrical engineering at the University of Tennessee, Knoxville under the guidance of Dr. Dan Wilson.